# MODELING, DESIGN, FABRICATION AND DEMONSTRATION OF MULTILAYERED FERROMAGNETIC-POLYMER DIELECTRIC COMPOSITES FOR ULTRA-THIN HIGH-DENSITY POWER-INDUCTORS

A Dissertation
Presented to
The Academic Faculty

by

Dibyajat Mishra

In Partial Fulfillment
of the Requirements for the Degree
Doctor of Philosophy in the
School of Materials Science and Engineering

Georgia Institute of Technology
December, 2015

# MODELING, DESIGN, FABRICATION AND DEMONSTRATION OF MULTILAYERED FERROMAGNETIC-POLYMER DIELECTRIC COMPOSITES FOR ULTRA-THIN HIGH-DENSITY POWER-INDUCTORS

Approved by:


Dr. Rao Tummala, Advisor
School of Materials Science and Engineering
*Georgia Institute of Technology*

Dr. Hamid Garmestani
School of Materials Science and Engineering
*Georgia Institute of Technology*

Dr. Rosario Gerhradt
School of Materials Science and Engineering
*Georgia Institute of Technology*

Dr. Erik Shipton
GTRI
*Georgia Institute of Technology*

Dr. P. Markondeya Raj
School of Electrical and Computer Engineering
*Georgia Institute of Technology*



Date Approved: 8/6/2015

[Dedicated to my parents and sister]

# ACKNOWLEDGEMENTS

I would like to thank and express my sincere gratitude to my advisor Prof. Rao Tummala for giving me the opportunity to work on a leading edge project at the Georgia Tech 3D systems packaging research center. He has been a constant source of inspiration. His vision and advice has greatly helped in shaping my thesis. I am extremely grateful for having been mentored and advised by Prof. Tummala.

I would also like to thank my mentor Dr. Raj for his invaluable support and mentorship over the years. His technical depth has helped guide me every step of the way. I have learnt much more than I could have ever hoped for. Next, I would like to thank my committee members: Prof. Rosario Gerhardt, Prof. Hamid Garmestani , and Dr. Erik Shipton for being part of my PhD committee and for all the valuable suggestions and feedback.

I have had the privilege to work with a very knowledgeable and enthusiastic team at the Georgia Tech PRC and I would like to thank Dr. Venky Sundaram, Dr. Himani Sharma, Dr. Fuhan Liu, Dr. Vanessa Smet, Mr. Sung Jin Kim, and Mr. Nitesh Kumbhat for all of their invaluable support over the course of my stay at Georgia Tech. Next I would like to thank the PRC staff: Karen May, Patricia Allen, Brian McGalde, Chris White, and Jason Bishop for all their support over my stay at the GT PRC. I would also like to extend a special thanks to all the visiting engineers: Yoichiro Sato (AGC), Yuya Suzuki (Zeon Chemicals), Toshitake Seki (NGK-NTK), Makoto Kobayashi (Namics Corporation), Yutaka Takagi (NGK-NTK), and Ryuta Furuya (Ushio).

My stay in Atlanta would not have been the same but for the support of great friends: Drishti, Pratik, Aditi, Nabankur, Dhruv, Srikrishna, Vijay, Bruce, Saumya, Brett, Xian,

Sadia, Gokul, Timothy, Kaya, , Zihan, Chinmay, Chandra, William, Tapo, Qiao, Hao, Gary, Yushu, Koushik, Jialing, Min Suk, Bhupendra, Ninad, Tengsun, Partha, and Tailong. Lastly I would like to thank my parents who have made me what I am today. I am extremely grateful for all their love and support.

# TABLE OF CONTENTS

# LIST OF TABLES

# LIST OF FIGURES

Page

# SUMMARY

The evolution of multifunctional smart and wearable electronic systems is primarily enabled by the integration of multiple functions such as RF, analog, digital, MEMS, sensors in the same system. Integration of these heterogeneous technologies with variety of active devices requires multiple power modules to convert the battery voltage to the device voltage and current requirements. Energy storage components such as inductors are the largest components in these power modules, directly impacting both system performance and miniaturization.

Power-handling and efficiency of inductors is limited by the magnetic materials used as inductor cores. Existing materials do not achieve high Ms and μ with low loss at the desired frequency of operation (1-10 MHz) for enabling high inductance density and power handling with high efficiency. This thesis presents material modeling, design, fabrication, characterization and integration of a new class of multilayered ferromagnetic-polymer composite structures as magnetic cores for high-density power inductor applications. The multilayered composite structures comprise of stacked high-permeability, high-Ms, low-coercivity magnetic layers with ultrathin polymer adhesives. The adhesive acts as an insulating layer to reduce eddy current losses while also enabling high permeabilities and power-handling at operating frequencies of above 1 MHz.

Fundamental material models were developed using electromagnetic (EM) simulation techniques to design the composite micro-structures to achieve permeability of above 500 in the frequency range of 1-10 MHz. Various magnetic materials (NiFe, NiFeMo, CoZrO) were studied and the effects of their resistivities and thicknesses on the frequency-dependent permeability were analyzed through modeling. A new manufacturable adhesive-coating and layering process was developed to demonstrate

fabrication of the multilayered composite structures based on the design inputs from modeling. The fabricated composite structures showed an $M_s$ of 0.62T, coercivity of 4.4 Oe and $\mu$~500 at 10 MHz.

Toroid-based multilayered composite inductors were designed to achieve high-inductance densities and power handling in the MHz frequency regime (1-10 MHz). The multilayered composite structures were subtractively patterned on silicon substrates to form toroid structures. The patterned toroids were integrated with copper windings to demonstrate fabrication of ultra-thin inductors on silicon. These ultra-thin inductors (thickness < 100 microns) are shown to be capable of achieving high inductance densities of upto 2000 nH/mm$^2$ and power handling of 1A/mm$^2$ for 100 $\mu$m component thickness.

In summary, using material modeling, design, fabrication and characterization, and their integration onto silicon substrates as high-density inductors, novel ferromagnetic-polymer composite structures were demonstrated with high inductance densities and with improved power handling in the 1-10 MHz frequency regime.

# CHAPTER 1

# INTRODUCTION

## 1.1 Strategic need

The emerging need for smart and wearable electronic systems are driving new electronics technology paradigms in miniaturization, functionality and cost. Such systems are expected to provide computing, wireless communications, wireless healthcare, security, banking, entertainment, navigation, and a variety of other functions in ultra-small thickness. This requires integration of multiple technologies such as digital, RF, analog, optical, MEMS and sensors devices into ultra-small packages and systems. Increasing functionality of such systems has imposed a high demand on power storage and power conversion circuitry, while reducing system real estate. The operating voltages and power levels for devices in these systems are becoming increasingly varied with increased diversity of devices to serve these heterogeneous functions[1, 2]. To accommodate these varied power levels, power convertors are incorporated into various parts of these systems to step-up or step-down battery voltages and currents. Hence, multiple power converters, to power different functional blocks of the system, each requiring several passive components, are used to create stable power-supplies. This places significant challenges in ultra-miniaturized and ultra-efficient power management technologies[3, 4].

A typical power convertor consists of an active network of switches and diodes integrated into a power management IC (PMIC) that works in conjunction with passive components, such as capacitors and inductors, to perform the voltage conversion. Figure 1.1 shows the schematic of a point-of-load (POL), dc-dc, switched mode power supply (SMPS) used in mobile phones today, consisting of active silicon devices (controller,

MOSFETS, and drivers) and several passive components (*R*, *L*, *C*) to complete the voltage regulation[5]. Most state-of-art power management modules consist of a PMIC

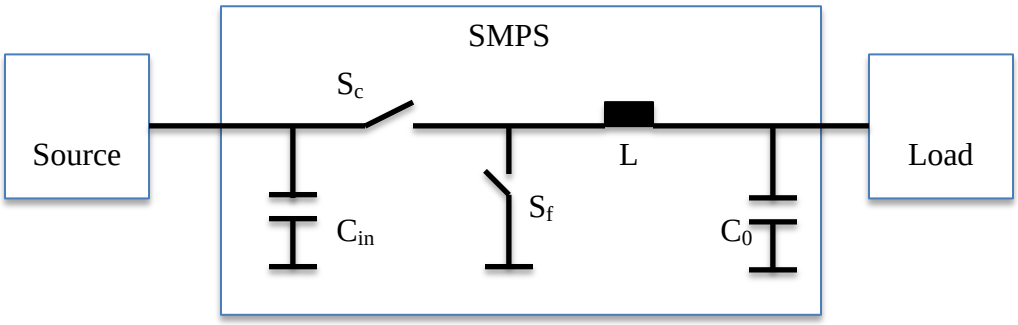


Figure 1.1 Schematic of a typical point-of-load converter

and application processor assembled on a board with multiple discrete passive components[6]. Figure 1.2 shows leading smartphones such as from Apple with PMIC and passives mounted side-by-side on the board to create a discrete power converter solution. This increases the system size and limits its performance because of the large parasitics from the long interconnect length. This approach also consumes real estate on the board. This challenge is partially addressed by power semiconductor companies with embedding of active components. The key barrier for miniaturization and performance enhancement in power modules is the integration of passive components. Current passive components are available as discrete devices that are individually packaged and surface-mounted on the package or board. Integration of passive components as thinfilms in the power modules, while simultaneously meeting the performance goals such as efficiency, current-handling and voltage ripple tolerances is the key to achieve system overall system miniaturization and system performance. Inductors are typically the largest components in a power supply module[7].

This thesis focuses on innovative magnetic materials and their integration as miniaturized thinfilm inductors while simultaneously improving the power-handling and efficiency.

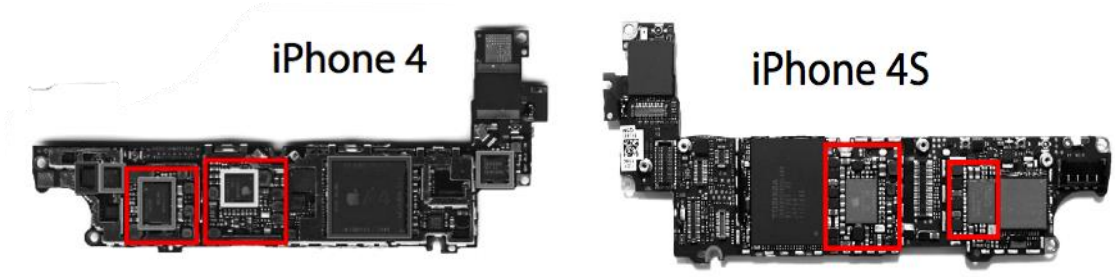


Figure 1.2 Apple's iPhone 4 and 4s with 2D mounted PMIC and passive components[6].

## 1.2 Evolution of Integrated Power Converter Modules

Power convertors are mostly manufactured as discrete modules with individually packaged components that are mounted on the board. However, there is an increasing trend to integrate or co-package multiple components for increased performance and system miniaturization. This section briefly describes these advances and then introduces the 3D power module vision of GT-PRC.

**Discrete power modules:** Figure 1.3 shows a conventional discrete power module introduced by Texas Instruments (TI) with a set of (>10) standard discrete components mounted side by side on an FR4 substrate. Typically, the largest component in the converter is the inductor. As mentioned earlier, such a large discrete components occupy a large area in a system and its performance is limited due to interconnection parasitics.

Figure 1.3 Discrete DC-DC converter module (Courtesy: TI)[7]

Increase in switching frequencies reduces the passive component need, which plays a key role in the integration and miniaturization of power converter modules. For a typical POL buck converter, the required inductances and capacitances are inversely proportional to the operating frequency. The required inductance and capacitance are also affected by the load current specifications. The plot in Figure 1.4 shows a good illustration of how the required inductance and capacitance values change with frequency and load current. Thus, it can be seen that increasing the switching frequencies into the MHz region offers the potential for the reduction of passive component values to the point where their size becomes compatible with power IC dimensions.

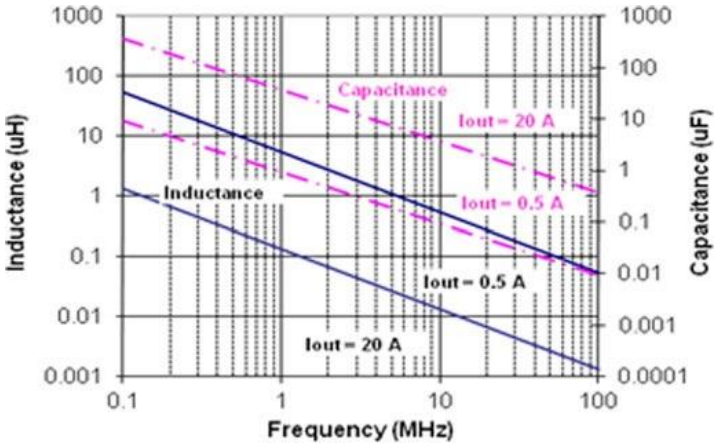


Figure 1.4 Impact of switching frequency on inductance and capacitance values[7]

**Power supply in package***:* Increasingly, many power semiconductor companies, including Enpirion, Fuji, Micrel, National Semiconductor, and TI, have reported products using integrated packages, either with one or more passives integrated into the same package as the PMIC, in either a planar or stacked form. Enpirion and Micrel have assembled, or co-packaged the output inductor in a plastic-encapsulated package on the same lead frame as the adjacent PMIC. Both Fuji and National Semiconductor have reported the use of customized ceramic ferrite inductors, which act as chip-scale substrates on which the PMIC is mounted. This dramatically reduces the dc–dc converter footprint while using a customized version of conventional magnetic component technology. Most current products on the market co-package either proprietary inductors or discrete ferrite inductors with the PMIC to produce a partially integrated solution, as shown in Figure 1.5.

More recently, TI [8] has gone a step further with its chip-scale package (MicroSiP) , with commercial ceramic passives, inductors and capacitors, assembled on a chip-scale PCB with embedded PMICs. It uses a thin Si-die embedded in an organic core with power components mounted on the top. Figure 1.6 shows the schematic of such a MicroSiP package made by TI.

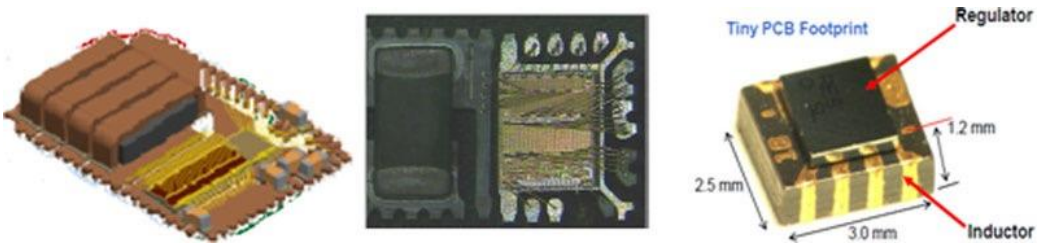


Figure 1.5 Commercial products with power supply in package. (Courtesy of Enpirion, Micrel and TI)[7].

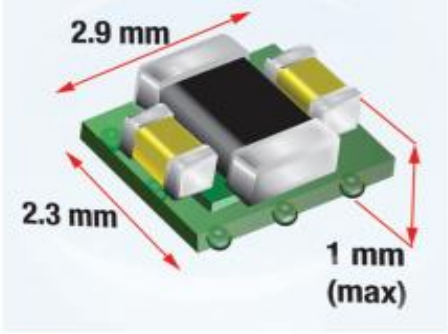


Figure 1.6 TI's MicroSIP module with embedded die and power components[8]

In spite of these recent advances in power modules, fundamental limitations in miniaturization and performance remain because of limited component integration and the side-by-side assembly in 2D packages. A complete integration of passive and active components (3D IPAC) to form complete functional modules in ultra-thin 3D packages is envisioned by GT-PRC, as the next era in power modules . Figure 1.7 shows the Georgia Tech PRC vision for such a miniaturized power converter module (5X thinner than prior art) using new generation of ultra-thin inductor and capacitor components that are only ~50 micron thickness, integrated double-side as thinfilms. The active components can also be surface-assembled on either side. Such an approach can lead to 10X increase in power densities without degrading the efficiency from interconnection parasitics. Hence, advanced thinfilm component technologies with the best properties, and their integration into ultra-thin substrates is seen as the next wave in power modules to meet the emerging needs in performance, size and cost.

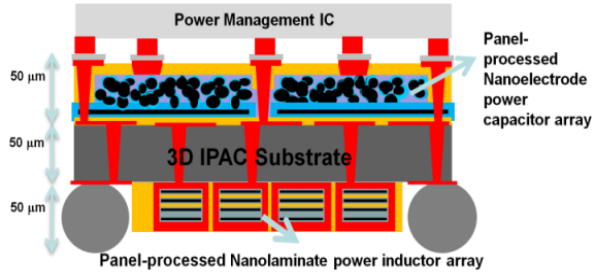


Figure 1.7 Miniaturized power converter module using new generation of passive components

**Inductors as a key bottleneck in miniaturization of power modules**: Most power conversion circuits require passive magnetic components such as inductors or transformers as energy storage devices. With miniaturization and improvements in active device performance, the development of power electronics systems has progressed to a state where the active devices' impact on the system's size and cost has been taken over by the passive components. Magnetic components are the largest and bulkiest components in power conversion systems, taking up significant circuit surface area and thus hindering their miniaturization. Miniaturization of power magnetic components has been widely researched to replace conventional inductors and transformers in power conversion systems. Standard integrated circuit (IC) processes are not intended to produce high-performance magnetics. Therefore, power converters typically use external magnetic components, even when other components are integrated.

## 1.3 Current approaches to inductor technologies

This section describes the common inductor designs and the different types of inductors used in dc-dc power converter modules.

Inductor design: An inductor consists of copper winding around a magnetic core or vice versa. The magnetic core has to form a closed magnetic loop to prevent flux leakage. The key electrical parameters that determine an inductor's performance are its inductance per unit area (inductance density), current-handling, equivalent series resistance, and *Q*-factor. The key inductor design parameters are selection of the inductor type, number of windings or winding pitch, and wire cross-section. These parameters, along with the materials properties of the core and winding, determine the performance of power inductors.

Depending on the arrangement of conductors with respect to the magnetic core, the construction of microinductors can be categorized into two different approaches. The first approach is to enclose the planar coils with a magnetic material. In the second approach, the conductor is wrapped around a planar magnetic core using multilayer metal windings. The main structures using the first approach are spiral inductors, potcore inductors (racetrack) and strip-line inductors. Typical examples of structures using the second approach are solenoid and toroid inductors. Figure 1.8 shows the schematic of racetrack inductors representing the first approach and toroid inductors showing the second design.

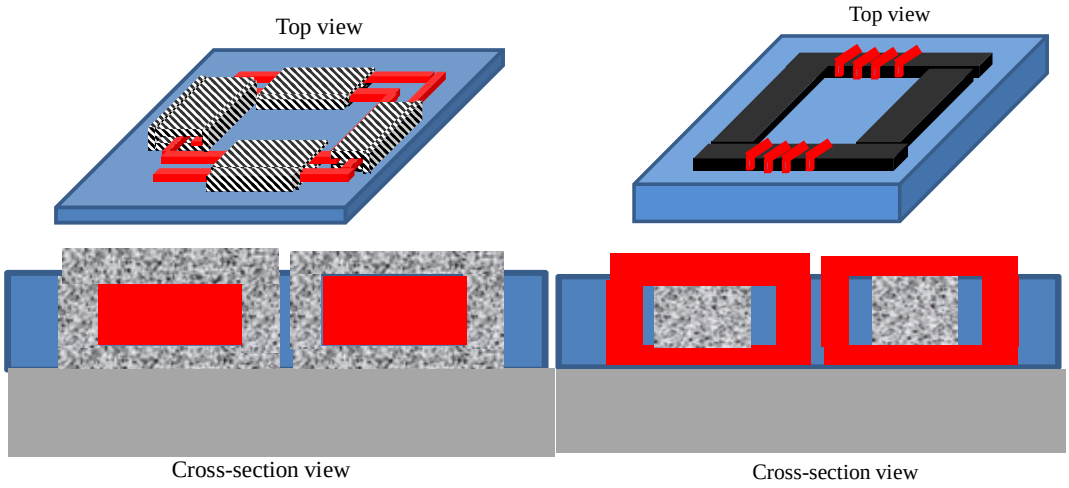


Figure 1.8 Schematics of inductor designs: (a) Racetrack inductor; (b) Toroid inductor

Types of inductors used in power modules: Power convertors are predominantly used as discrete ferrite-based inductors, discrete air-core inductors, or integrated thinfilm inductors with either nonmagnetic or magnetic cores. Surface-mount ferrite inductors are the workhorse of the power convertor industry. However, they are facing fundamental limitations because of their low frequency-stability and energy densities. They are also manufactured as thick components at temperatures exceeding 1200 C, which further limits their integration in emerging ultra-thin packages. Planar power inductors with fine-pitch spirals or coils that achieve the required inductance densities with the desired Q in a single layer at low cost, are therefore ideal. Such inductors, operating at a frequency of above 50 MHz, are generally based on nonmagnetic cores, either as discrete or integrated components. However, handling high power with high efficiency becomes difficult using this approach. Thinfilm magnetic-core inductors have advantages in inductance density and efficiency at frequencies below 10 MHz. However, they face challenges associated with processing and also suffer from degradation in quality factors at frequencies above 10 MHz.

## 1.4 Magnetic core materials for integrated thinfilm inductors

This section discusses the most commonly- used magnetic materials and their deposition techniques to form microinductors. The deposition techniques are categorized as screen-printing, sputtering, and electrodeposition, each of which has its own advantages and disadvantages.

Screen-printing of ferrite-polymer composites: In the 100 kHz to 1 MHz region, ferrites are the most popular magnetic materials for power applications. NiZn and MnZn ferrites

are the most common examples because of their low coercivity and high permeability. Ferrites require high-temperature processing and are therefore not substrate-compatible for direct integration. They are, therefore, screen printed as ferrite particle-polymer composites [9]. This technique presents a good compromise between the deposition of high-permeability magnetic material with high resistivity (i.e., >1 Ω·m) and the simplicity of processing due to polymer. As such, it has been widely explored in realizing microfabricated inductors[10, 11]. While screen-printing offers a comparatively simple process for deposition of low-loss cores, the inductance densities are lower with this approach because of the lower composite permeabilities.

Sputter-deposition of nanogranular materials: This technique has the advantage of depositing a wide range of magnetic materials, including alloys and oxides with resistivities in the range 100–1000 μΩ·cm, which greatly assist in limiting eddy current losses. Sputtering has been used for developing granular nanocrystalline films as core materials for microinductors. Such nanogranular magnetic materials include CoZrNb[12] FeCoBC [13], FeHfO and CoFeHfO [14, 15], FeZrO [15], $Fe_{59}$-$Co_{20}$-$B_{14}$-$N_7$[16], and Fe-B-N[17]. Sputtering has also been widely employed for depositing magnetic alloys with high resistivity, including CoHfTaPd thin film [18, 19], and multilayer CoZrTa/SiO2 [89]. The sputtered magnetic alloys have advantages of high saturation flux density and permeability, and their deposition is compatible with low-temperature CMOS wafers. The technique is ideal for depositing thin films upto a thickness of 5 microns. However, for thicker films, sputtering becomes a slow and expensive process.

Electroplating metal alloys: Electroplating magnetic films is another promising option to achieve the desired thick core layers for microinductors. The process is relatively inexpensive and is compatible with standard packaging fabrication,. The most commonly -electrodeposited magnetic material is permalloy (typically, 81% Fe and 19% Ni). The

combination of relatively high permeability, low hysteresis losses, and near zero magnetostriction (i.e., stresses in the devices will not impact the magnetic performance) has driven its use in microscale sensors, actuators, and power converters. Perhaps, the most significant reason for its common use is its wide adoption in magnetic recording heads. Electrodeposition has also been reported for the deposition of magnetic materials such as supermalloy (NiFeMo) [20], $Ni_{45}Fe_{55}$ [21] and Orthonol ($Ni_{50}Fe_{50}$) [22]. Additionally, electroplating techniques for multilayered thinfilm cores have also been investigated[23]. There are other interesting electroplated materials that include electrodeposited nanocyrstalline alloy, $Co_{65}$-$Ni_{12}$-$Fe_{23}$ [24], and electroplated CoFeP amorphous alloy [25], both showing relatively high saturation flux density (>1.8 T). In spite of their advantages, electroplated magnetic materials are metallic in nature, with high electrical conductivity, and, therefore, suffer from low Q-factors and poor frequency stability from eddy current losses.

A new class of magnetic cores with high permeability and high resistivity that can also be deposited using scalable and low-cost processes is thus required to address the limitations of current magnetic cores.

## 1.5 Objectives

The objectives of this research are to model, design, demonstrate and validate a new class of multilayered ferromagnetic-polymer composite structures as magnetic cores for power inductors**.** These inductor devices are aimed at achieving unparalleled combination of inductance density and power handling capability in the desired frequency regime of operation. The specific objectives of the proposed research compared to prior art and the challenges are shown in Table 1.1.

Table 1.1 Specific objectives of the proposed research

| Parameter | Prior Art | Objectives | Challenges |
|---|---|---|---|
| **1.Inductance density ($nH/mm^2$)** | 1000 | >2000 | High permeability (μ) with low loss at the desired frequency of operation(1-10 MHz) in ultra-thin form factor (50-100 microns) |
| **2.Power Handling ($A/mm^2$)** | 0.25 | 1 | High saturation magnetization ($M_s$) magnetic core in ultra-thin form factor (50-100 microns) for power handling |
| **3.Ultra-thin inductor** | 500 mms | 100 mms | Integration of high performance magnetic materials limited by geometry and processing requirements |

## 1.6 Fundamental Challenges in integration of magnetic materials with inductors

**Inductance density requirement**: Magnetic inductors for power applications with standard planar toroid and solenoid designs are modeled using analytical equations. The classical model predicts that the inductance of the solenoid inductor is enhanced by the relative permeability ($\mu_r$) of the magnetic core material [26].

$$L_{solenoid} = \frac{t_m w_m N^2 \mu_r \mu_0}{l_m} \qquad (1.1)$$

where N is the number of coil turns, and $w_m$, $t_m$ and $l_m$ are the width, thickness, and the length of the magnetic core, respectively. If a high-permeability material is incorporated into an inductor without producing extra losses, a substantially higher inductance can be obtained without increasing the number of windings or the size of the device, thus enhancing inductance density and also improving its efficiency.

**Power handling requirement**: The maximum power handling capacity of an inductor is the energy stored in one switching time period, which is given by

$$P_{max} = \frac{V_{core} f_{sw} Ms^2}{2\mu} \qquad (1.2)$$

where $V_{core}$ is the volume of the core, $M_s$ is the saturation flux density and $f_{sw}$ is the switching frequency. Thus, having a magnetic core with high saturation flux density greatly enhances the power handling capacity. For smaller real estate consumption, the thickness of the core also influences the energy storage capacity of the device. Apart from increasing the power handling capacity, the inductor size requirements can also be reduced by orders of magnitude by increasing the switching frequency.

High $\mu$ and high $M_s$ magnetic cores with enhanced thicknesses (50-100 microns) incur increased power losses. This has been an engineering barrier that needs to be overcome to achieve high inductance density and power handling. The dominating loss mechanism in metal composites in the target frequency regime (1-10 MHz) arises from eddy currents. Eddy currents are circulating currents induced in the core by the alternating magnetizing field. The induced eddy currents produce a magnetic field counteracting the magnetizing field, reduce the net magnetic flux in the core at higher frequencies, and shield it from the inner portion of the core cross-section. This phenomenon is called the magnetic skin effect. The decay of magnetic flux from the surface to the inner portion is exponential in nature. The core depth at which the flux decays to 1/e of the surface value is the skin depth, given by

$$\delta = \sqrt{\frac{\rho}{\pi f \mu}} \qquad (1.3)$$

where $\delta$ is the skin depth, $\rho$ is the resistivity and f is the frequency. Equation (3) indicates that the skin depth decreases with increase in conductivity, frequency and permeability. Increasing the thickness of a metal layer to above the skin depth leads to significant eddy current losses. Figure 1.9 shows a schematic depicting the effect of eddy current losses on the frequency-dependent permeability. This figure clearly shows the roll-off of permeability with frequency due to eddy current losses. Therefore, high-resistivity magnetic materials and ultrathin magnetic layers are needed to suppress eddy current losses and achieve high quality factors.

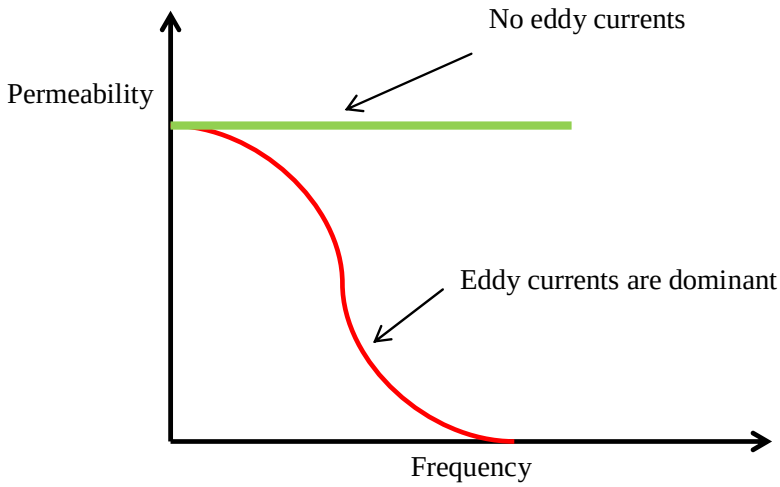


Figure 1.9 Effect of eddy currents on frequency-dependent permeability.

**Magnetic Material Limitations:** Power inductors have, to date, been limited to ferrites which have reached fundamental material and process limitations and hence their volumetric efficiency limitations. Ferrite cores have relatively high resistivity and hence low eddy current losses but suffer from low $M_s$ (0.1 to 0.3T), limiting their use in high-power applications [27]. Metal alloys such as nickel-iron and cobalt-iron have a much higher saturation flux density (0.8 to 2.4 T) compared to ferrite cores, making them ideal candidates for high power density devices. However, metal alloys suffer from high eddy current losses due to their low resistivity [26]. Metal composites can address these challenges, but only to a limited extent because of the suppressed permeability in metal particles compared to bulk metal. Amorphous and nanocrystalline magnetic composite cores suffer from high losses and low permeability at high frequencies due to the particle demagnetization. Sputtered nanogranular thin films permeabilities of above 200, saturation magnetization of above 2 T, and resistivity higher than 100μΩ-cm have been reported [12-17]. However, inadequate thickness of sputtered thin-film magnetic cores makes them unsuitable for high power applications. Thus, there is a lack of high μ, high Ms, low loss materials scalable to thickness of 50-100 microns to miniaturize power inductors at desired frequency of operation (1-10MHz).

## 1.7 Proposed Unique Approach: Multilayered ferromagnetic-polymer dielectric composites

To overcome the limitations of current approaches discussed above, a set of unique magnetic structures and processes are proposed to fabricate ultra-high density power inductors. The proposed structure consists of multiple layers of stacked ferromagnetic films, separated by ultra-thin insulating polymer dielectric layers, to act as the core of the inductor. Figure 1.10 shows the schematic of such a composite structure.

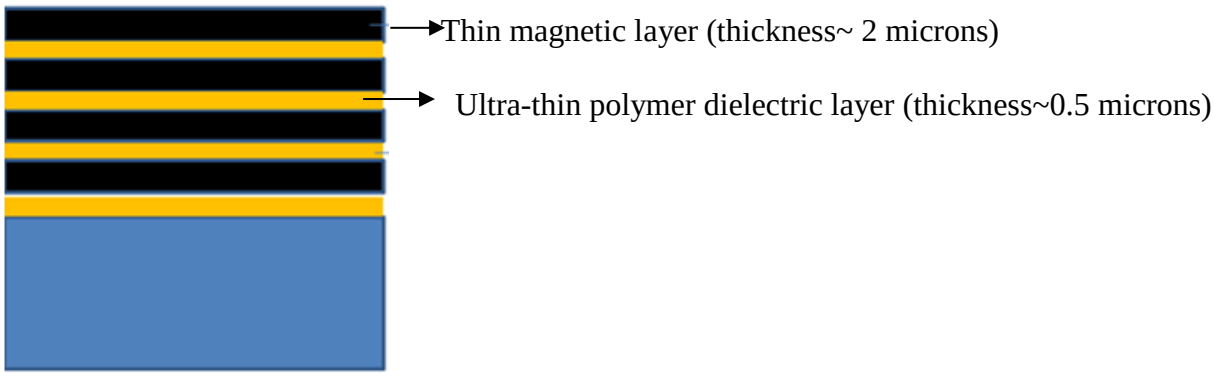


Figure 1.10 Schematic cross-section of multilayered ferromagnetic-polymer dielectric composite

The ferromagnetic layers are proposed to be made of high-permeability, high-$M_s$ and low-coercivity magnetic materials. The thickness ($t_c$) of each magnetic layer is designed such that it is thinner than the skin depth in the desired frequency regime, computed using Equation 1.3. This reduces the eddy current loss and enhances the frequency stability of permeability. Different magnetic materials are chosen to study the effects of their resistivity and thickness on the frequency of operation.

The polymer-dielectric layers acts as both an insulating layer as well as an adhesive layer to stack the magnetic layers. The thickness of the polymer layers affects the $M_s$ and permeability of the composite structure. The effective $M_s$ of the structure can be computed as:

$$Ms_{eff} = qMs_i \qquad (1.4)$$

where $Ms_{eff}$ is the saturation magnetization of the effective composite, q is the volume fraction of ferromagnetic layers and $Ms_i$ is the saturation magnetization of individual magnetic layers. Thus, it can be seen that higher effective composite $M_s$ can be achieved with thinner polymer layers. Yet, the ultra-thin polymer adhesive layers should still have sufficient adhesion strength to bond the magnetic layers strongly.

The proposed research addresses the fundamental challenge of eddy current losses at high frequencies by modeling the composite structure so as to achieve high μ and high $M_s$ for power supply inductors. Figure 1.11 compares the performance of current magnetic inductors with that of the proposed approach.

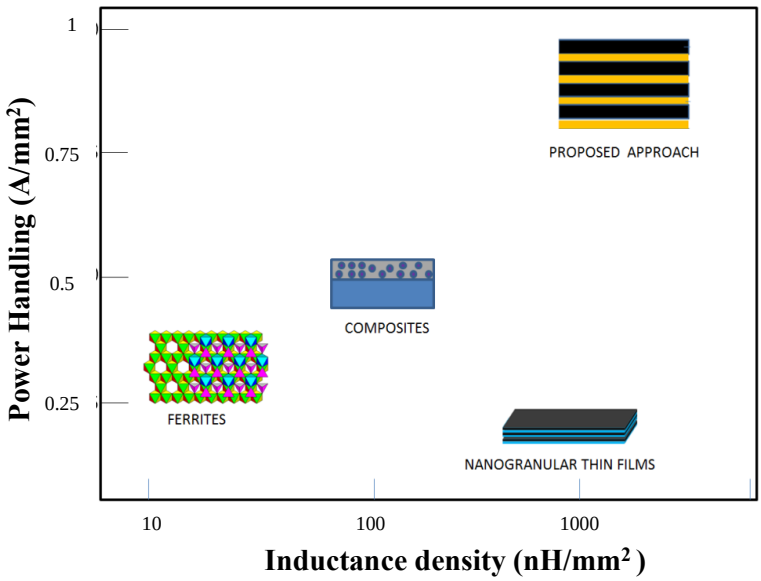


Figure 1.11 Current magnetic core approaches vs proposed approach for Power Handling.

Figure 1.12 shows a schematic of the integrated inductor structure with the proposed composite structures. The multilayer composite is patterned and integrated with coils wound around it to fabricate planar, integrated, high-density inductor structures.

The proposed novel magnetic composite structures, thus, enable high inductance and power densities to decrease the total volume of magnetic components for miniaturized

integrated power-supply modules with higher power handling, low profile of devices and easy fabrication.

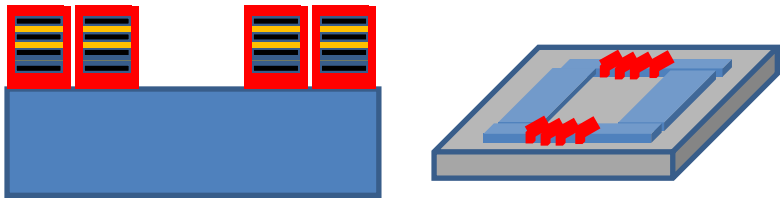

Figure 1.12 Integrated inductor structure using multilayered composite core

## 1.8 Research Challenges

Three major challenges are foreseen in achieving the objectives with the proposed approach.

**1.High-μ and low-loss composite structures:** The multilayered composite structure has to be modeled and designed such that it can obtain high μ, low loss and high $M_s$ at frequencies of 1-10 MHz. Existing material models do not accurately predict the frequency-dependent permeability and losses of multilayered composite structures.

**2.High Ms multilayered composite structure:** The multilayered composite structure has to be fabricated with ultra-thin polymer interlayers to achieve high μ, high $M_s$ at 1-10 MHz. The composite structure should have adequate thickness for power-handling. This requires bonding the magnetic layers using ultra-thin insulating polymer layers, with adequate adhesion strength to the magnetic layers so that there is no delamination during further processing and inductor usage.

**3.Demonstration of ultra-thin inductors:** Substrate-compatible, thin-film inductor fabrication is another challenge. Micro-patterning the multilayered composite structures to form copper windings around them requires innovative processing. Formation of coils around the patterned composite structures to fabricate planar, integrated inductors also needs to be addressed.

## 1.9 Research Tasks to Address Challenges

**Task 1: Material modeling and design for high-μ and low-loss composite structures:**

- Model high-frequency magnetic properties of composite structures through simulations and analytical models
- Design composite structures capable to achieve the target properties based on the models.

**Task 2: Material synthesis and characterization of high Ms multilayered composite structures**

- Fabricate multilayered composite structures with ultrathin polymer dielectrics that act as adhesive layers.
- Characterize multilayered composite structure to extract $M_s$ and frequency-dependent permeability, thus validating the models from Task 1.

**Task 3: Design, fabrication and demonstration of ultra-thin inductors :**

- Design inductors using the proposed multilayered composite core structure to achieve high inductance density.
- Pattern multilayered composite structure and form coils around them to fabricate planar, integrated inductors.

## 1.9 Dissertation outline

The outline of the dissertation is listed below and is based on the strategy described in the previous section. Chapter 2 presents the literature review. This chapter first presents the basic fundamentals of power inductors. Material modeling and loss mechanisms of magnetic composites are described next. Fundamental structure and properties of various magnetic materials used as inductor cores and their challenges are described in detail.

Chapter 3 presents the modeling and design of multilayered composite structures. Electromagnetic (EM) based modeling techniques are used to extract the effective frequency-dependent permeability of the composite structure. The effect of various parameters on the frequency dependent permeability is also studied. Based on the modeling results, the multilayered composite structure is designed to achieve the target properties.

Chapter 4 presents the fabrication and characterization of the multilayered composite structure. The complete process details and structural characterization of the multilayered composite structure are described in this chapter. DC and high frequency magnetic characterization of the composite structure are also shown.

Chapter 5 describes the inductor design, fabrication and characterization on the multilayered composite structure. The first part of the chapter presents the design and fabrication of Si-integrated toroid inductors with the multilayered composite structure. The process of micro-patterning the composite structure and forming coils around them to demonstrate ultra-thin inductors is described in detail. The electrical characterization of the fabricated inductors is shown next.

Chapter 6 concludes the work presented in this dissertation and summarizes the key findings and contributions. It also provides the scope and suggestions for future work.

# CHAPTER 2

# LITERATURE REVIEW

This chapter begins with a review of inductor applications in power converter modules and their key performance metrics, and translates them into inductor design and its material properties. The fundamentals that govern these magnetic properties are briefly discussed to put the prior art literature in perspective. Recent major innovations in magnetic materials to achieve inductor integration with enhanced performance are then reviewed. These materials are classified as ferrites, microcomposites and nanomagnetic materials. Fundamental structure and properties of these materials and recent advances to overcome the limitations of traditional materials are described in detail. The last part of the chapter describes various fabrication methods to form integrated inductors using such advanced magnetic core materials.

## 2.1 Role of inductors in power converter modules

Portable electronic applications typically use three kinds of DC-DC power converters: switch-mode power converters (SMP), linear converters and switched capacitor converters. Among these categories, SMP converters are widely used for high-power applications because their high -efficiency increases the battery life. Such converters consist of a switch, often a metal oxide semiconductor field effect transistor (MOSFET), a diode, input and output capacitors, and an output inductor. The schematic circuit for SMP converters is shown in Figure 2.1. During its operation, the switch is closed for a certain amount of time depending on the input voltage and the desired output voltage. When the switch turns off, this energy is released into the load.

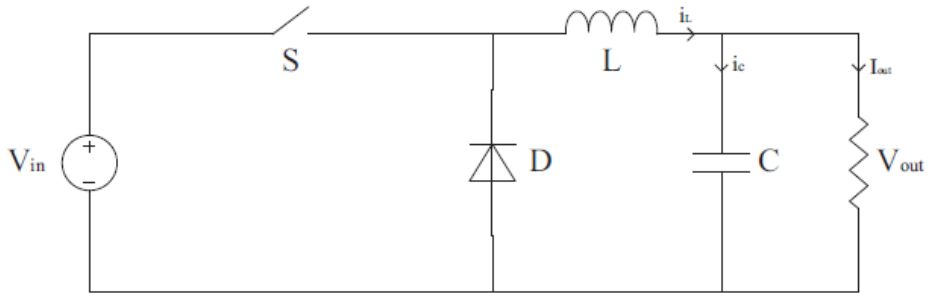


Figure 0.1 Schematic circuit of a switch-mode power converter.

Switching regulators use inductors as energy storage devices. When the semiconductor switch is "on", the current in the inductor ramps up and energy is stored in the form of magnetic field, which, in turn, resists changes in the current passing through it. The amount of energy stored in the inductor is given by [26]:

$$E = \frac{1}{2}Li^2 \quad (2.1)$$

where L is the inductance in Henrys and I is the peak value of inductor current. The current change during a switching cycle is known as the ripple current, and is defined by the equation.

$$V_1 = L.\frac{di}{dt} \quad (2.2)$$

where $V_1$ is the voltage across the inductor, di is the ripple current and dt is the duration for which the voltage is applied. The ripple current depends on the inductance. Therefore, having a high inductance is important in order to obtain acceptable current ripple. The inductor size requirements reduce with higher switching frequencies.

Inductors are designed with metal coils, which generate magnetic field when current is flowing through them. The magnetic flux is further enhanced when a magnetic material, increasing the inductance and energy storage density, surrounds the coil. Two types of topologies are most commonly used to enhance the inductance: 1.)Spirals with magnetic medium wrapped around the coils, also referred to as race-track or potcor inductors, and

2.)Magnetic loop with copper winding wrapped around them, also referred to as toroid inductors. The key topologies are illustrated in Figure 1.8 of Chapter 1.

The key parameters for enhancing inductance density are the permeability of the magnetic core and number of turns. The operation frequency of the power switch determines the losses in the inductor, which, in turn, is determined by the frequency stability of the magnetic materials. These magnetic materials also need to be integrated with inductor topologies without increasing the processing cost.

The maximum energy stored in an inductor in a SMP is an important parameter that determines it's power-handling. The magnetic energy stored in an inductor can be expressed as:

$$W = \frac{1}{2}\int B.Hdv = \frac{1}{2}\int \frac{B^2}{\mu} \quad (2.3)$$

where $B$ is the magnetic flux density, $H$ is the magnetic field intensity and μ is the permeability of the core. The core material is assumed to be linear and homogenous. The maximum energy stored in the inductor for a uniformly distributed magnetic field in the core is given by:

$$W_{max} = \frac{V_{core}(Bs)^2}{2\mu} \quad (2.4)$$

where $V_{core}$ is the volume of the core, μ is the permeability, $B_s$ is the saturation flux density. The maximum power handling capacity is the energy stored over one switching time period, calculated by multiplying the operating frequency of the converter to the magnetic energy stored

$$P_{max} = \frac{V_{core} f_{sw}(Bs)^2}{2\mu} \quad (2.5)$$

where f is the switching frequency of the converter. The power handling is determined by the saturation magnetization ($M_s$) as seen from Equation 2.5.

## 2.2 Fundamentals of magnetic properties

Relative permeability ($\mu$) and saturation magnetization ($M_s$) are the most important properties of magnetic materials for designing power inductors. Permeability is a measure of the degree of magnetization in a material in response to an applied magnetic field. Saturation magnetization is the maximum magnetic flux density in a material under an applied magnetic field. In general, permeability is not constant as it can vary with the material structure, the frequency of the applied field, temperature, and other parameters. Magnetic materials at high frequencies are subject to various kinds of losses, which lead to degradation in permeability. However, $M_s$ is a constant intrinsic property which primarily depends on the composition of the magnetic materials.

Ferromagnetic materials such as Fe, Co, Ni and their alloys have high $\mu$ and Ms. However, due to their metallic nature, they are very lossy at high frequencies. Therefore metal-insulator composites are used for high-frequency applications although the effective permeability of the composites are much lower than that of the metal fillers. Analytical models based on effective medium theory (EMT) or Bruggeman's model are used to estimate the permeability of particulate magnetic composites as a function of metal filler permeability and volume fraction [28].

The EMT equation is represented as:

$$c_a \frac{\mu_a - \mu_{eff}}{\mu_a + 2\mu_{eff}} + c_b \frac{\mu_b - \mu_{eff}}{\mu_b + 2\mu_{eff}} = 0 \qquad (2.6)$$

where $\mu_a$ and $\mu_b$ refer to the permeabilities of the filler and matrix, $c_a$ and $c_b$ refer to the volume fraction of the filler and matrix, and $\mu_{eff}$ is the effective nanocomposite permeability. However, existing analytical models cannot accurately capture the size, morphology, composite structure and frequency effects. Therefore, electromagnetic simulations are developed to further improve the accuracy. For example, in a recent

study, the effective permeability of a multilayered magnetic substrate was estimated using S-parameters obtained from HFSS based electromagnetic simulations [29].

### 2.2.1 Magnetic Losses and Frequency-Dependence of Permeability

The major loss mechanisms that govern the high-frequency permeability of magnetic materials are hysteresis, domain wall resonance, eddy current damping and Landau-Lifshitz (LL) phenomenological damping leading to ferromagnetic resonance (FMR). For thicker conducting magnetic films, eddy current effects dominate at frequencies lower than those at which L-L damping effects are observed. The eddy current effect depends on the skin depth, as computed in Equation 1.3 (Chapter 1). Equation 1.3 indicates that the skin depth decreases with increase in conductivity, frequency and intrinsic permeability. Increasing the thickness of a metal layer to above the skin depth leads to significant eddy current losses. The effective permeability due to eddy current screening for an infinitely wide film can be obtained using Maxwell's equations as [30]:

$$\mu = \mu_i \frac{2\delta}{(i+j)d} tanh \frac{(1+j)d}{2\delta} \qquad (2.7)$$

where $\mu_i$ is the intrinsic relative permeability, d is the film thickness and $\delta$ is the skin depth. Using high-resistivity magnetic materials or making the magnetic film thickness less than the skin depth at the desired frequencies can counteract eddy current losses.

The eddy current losses in particulate metal-composites, expressed as $\mu''$, are a strong function of particle size, particle conductivity and the frequency. They are represented as [31-33]:

$$\frac{\mu''}{\mu'} = \frac{2\pi\mu_o\mu_r D^2 f}{3\Omega} \qquad (2.8)$$

$\Omega$ is the particle resistivity, D is the particle size, $\mu_r$ is the relative permeability, and f is the frequency. A linear change in $\mu'/(\mu'')$ with frequency is, therefore, an indication of

eddy current losses. They are directly proportional to the particle size and are, therefore, higher for microscale particles [34] compared to nanoparticles. The frequency ($F_{EC}$) above which the eddy current losses dominate is estimated using the equation:

$$\frac{4\rho}{\pi\mu_o(1+\chi)D^2} \qquad (2.9)$$

where ρ is the resistivity and ***X*** is the magnetic susceptibility [34].

The losses from domain wall resonance become prominent when multidomains are present within the particles, and are usually dominant at 1-250 MHz frequencies for microsized ferrites and metallic nanoparticles [35, 36]. A simplified equation used for estimating the domain wall resonance is given by [37]:

$$\frac{\omega_{DW}}{\gamma} = M_s\sqrt{\frac{4\pi\delta}{D_d}} \qquad (2.10)$$

where $\delta_{DW}$ is the domain wall resonance frequency, $M_s$ is the saturation magnetization where δ is the domain wall thickness, γ is the gyromagnetic ratio and $D_d$ is the domain spacing or domain size. The domain wall thickness is dependent on the exchange constant (A) and the magnetic anisotropy energy (K). The domain size varies with the particle dimensions. Finer particles show domain wall resonance at higher frequencies. In case of larger microscale particles, domain wall resonances leads to magnetic losses at lower frequencies, while these losses are absent in single-domain finer nanoparticles.

### 2.2.2 Frequency stability from FMR

The electron magnetic moment in a ferromagnet precesses about the direction of the magnetic field, and energy is absorbed strongly from the RF transverse field when the RF frequency is equal to the precession frequency [38]. A transmitted field shows a dip at the ferromagnetic resonance frequency due to the coupling of the microwave energy to the

magnetic spin system. The transverse magnetic susceptibilities are very large because of the high magnetization in ferromagnetic moments. For an anisotropic material, this resonance frequency is given by:

$$\frac{\omega_{FMR}}{\gamma} = \sqrt{(4\pi M_s + H_k)H_k} \quad (2.11)$$

where $H_k$ is the anisotropy field, $M_s$ is the saturation magnetization and $\gamma$ is the gyromagnetic ratio (2.31 x $10^8$ m/kAs).

The tradeoff between high permeability and operation at high frequencies is described by Snoek's limit [39].

$$(\mu_r - 1)F_{res} = (\frac{\gamma}{3\pi}4\pi M_s) \quad (2.12)$$

For soft magnetic thin films with uniform uniaxial in-plane anisotropies, a modified law, known as Acher's limit, is applicable:

$$(\mu_r - 1)F_{res}^2 = (\frac{\gamma}{2\pi}4\pi M_s)^2 \quad (2.13)$$

Where $F_{res}$ is the FMR frequency and $\boldsymbol{\gamma}$ is the gyromagnetic factor. Thus, a high saturation magnetization ($4\pi M_s$) enables high permeability at elevated frequencies of operation.

## 2.3 High-permeability magnetic materials for inductor cores

Inductors used in portable power management applications require soft magnetic materials with low coercivity, high permeability, high $M_s$ and large ferromagnetic resonance frequencies. Due to their high permeability, ferromagnetic materials such as crystalline metal alloys, amorphous metal alloys and ferrites are commonly used as core materials. The core material should be chosen such that it provides high resistivity to reduce eddy current loss at high frequency, low hysteresis loss for high efficiency, fairly simple fabrication process and capability of integrated fabrication with ICs or packages. This section briefly reviews the status and progress in state-of-the art materials and

technologies used as inductor cores. Figure 2.2 shows the classification of inductor core magnetic materials described in this section.

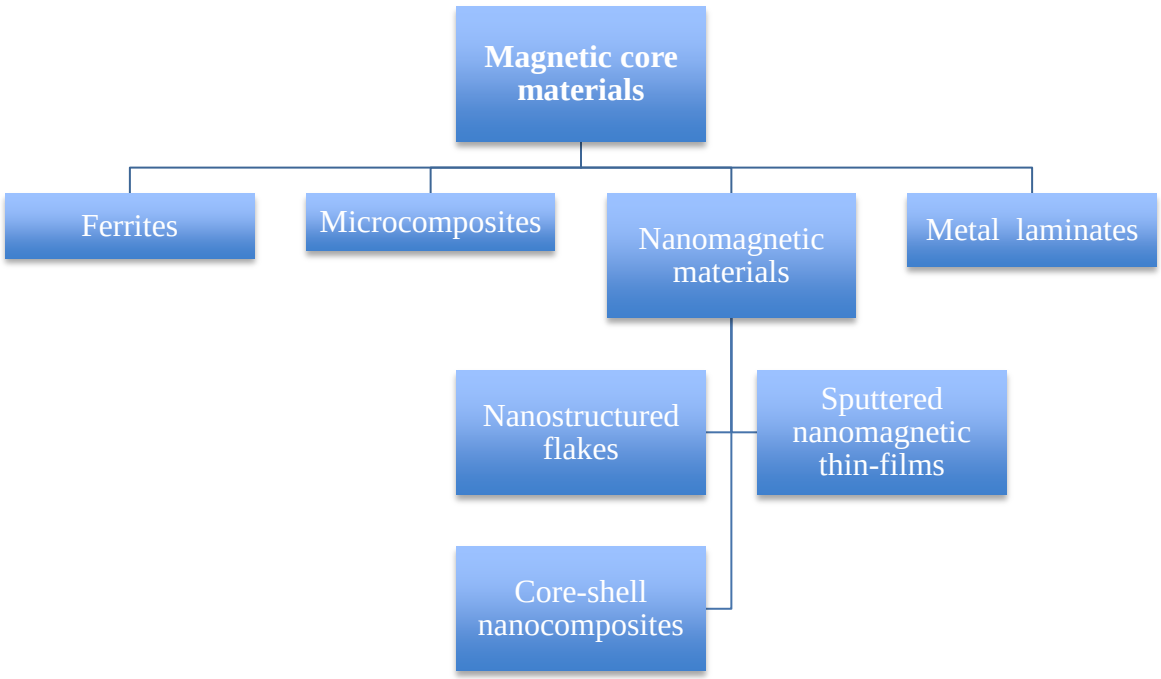


Figure 0.2 Classification of magnetic materials used in inductor cores.

### 2.3.1 Ferrites

For high-frequency applications, the conductivity of metals limits their use and so magnetic insulators such as soft ferrites are widely used. Ferrites are ceramic magnetic solids, commercially utilized as magnetic cores since 1945. They are ferrimagnetic but on the bulk scale behave in much the same way as ferromagnets. Ferrites are complex magnetic oxides that contain the ferric oxide ($Fe_2O_3$) as their basic magnetic component. Soft ferrites have a cubic crystal structure with the general chemical formula $MO.Fe_2O_3$ where M is a divalent transition metal such as Mg, Mn, Zn, Ni etc [40]. The crystallography of ferrites fall into three types: (I) the cubic ferrites of spinel type, (II) the cubic ferrites of the garnet type and (III) the hexagonal ferrites. Spinel ferrites (e.g., $NiFe_2O_4$, Mn-Zn and Ni-Zn-ferrites) [41] are extensively used in power converters because of their lower losses than metal cores, resulting in high Q factors at moderate

frequencies of 100 kHz to 1 MHz. Figure 2.3 shows a schematic of the spinel unit cell showing the arrangement of atoms.

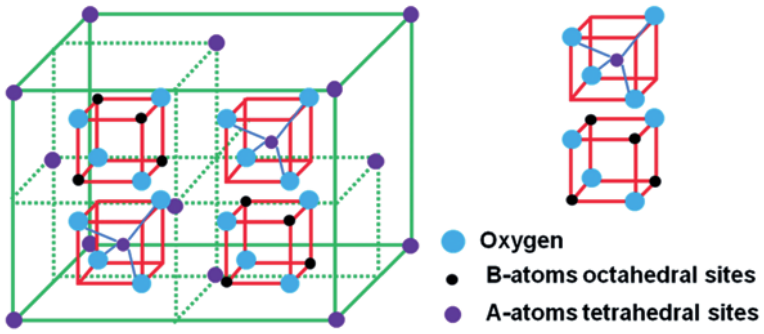


Figure 0.3 The unit cell structure of spinel ferrite [42].

As can be seen from the figure, in a spinel ferrite, the metal ions are either A-type, located on the tetrahedral sites, or B-type arranged in octahedral sites and are separated by oxygen ions. As a result of this, ions in the tetrahedral sites are oriented antiparallel in spins compared to those in the octahedral sites. In majority of ferrites, the number and type of ions at both the sites are different and this causes a net resultant magnetization because all the spins are not completely cancelled. Due to the partial cancellation of spin moments, ferrites have a much lower saturation magnetization compared to metallic iron[40]. However, ferrites still possess sufficient saturation magnetization to make them useful in a wide range of applications.

All the commercial ferrites are mixed ferrites (solid solutions of one ferrite in another). Their Curie points range from $300^{o}$ to $600^{o}$C, and $M_s$ from 100 to 500 emu/$cm^3$. All of them have <111> easy directions of magnetization, low crystal anisotropy, and low to moderate magnetostriction [43]. The outstanding fact about ferrites is that they combine extremely high electrical resistivity with reasonable good magnetic properties. Therefore,

they can operate with virtually no eddy current losses at high frequencies, where metal cores would be useless. This fact accounts for virtually all the applications of soft ferrites.

Two broad classes of soft ferrites are commercially produced[27]:

1.Mn-Zn ferrites: These have initial permeabilities of the order of 1000 to 2000, coercivities of less than 1 Oe, and are effective without serious losses upto a frequency of 1MHz. Their resistivity is about 20-100 ohm-cm. These resistivities are too low to minimize the eddy current losses at higher frequencies.

2.Ni-Zn ferrites: These are designed for high-frequency operation of upto 10 MHz. Initial permeabilities are 10-1000, and coercivities are several oersteds. The Ni-Zn ferrites have very high resistivity, about $10^5$ ohm-cm, resulting in low eddy current losses even at high frequencies.

Both of these main classes of materials contain zinc ferrite. Zinc ferrite, $ZnFe_2O_4$, is a normal spinel, and as such, the unit cell has no net magnetic moment. Manganese ferrite is an inverse spinel and consequently, the two magnetic sublattices are antiferromagnetically aligned. When the nonmagnetic zinc ion is substituted into the manganese ferrite lattice, it has a stronger preference for the tetrahedral site than does the ferric ion and thus reduces the amount of $Fe^{3+}$ on the tetrahedral site. Because of the antiferromagnetic coupling, the net result is an increase in magnetic moment on the octahedral lattice and an increase in saturation magnetization of Mn-Zn ferrites. The increase in $M_s$ of Ni-Zn ferrites also occurs by a similar phenomenon [44].

The magnetic properties of ferrites are determined by the chemical composition, porosity and grain size [45]. Of these, grain size is the most important parameter that affects the magnetic properties of ferrites. Coarse-grained ferrites have a high permeability. The grain boundaries represent obstacles to domain movement, thus decreasing the

permeability. The grain boundaries in power ferrites should exhibit a high resistivity in order to decrease power losses [46]. Figure 2.4 shows the variation of permeability of Mn-Zn ferrites with grain size, indicating that the permeability increases with grain size as mentioned earlier.

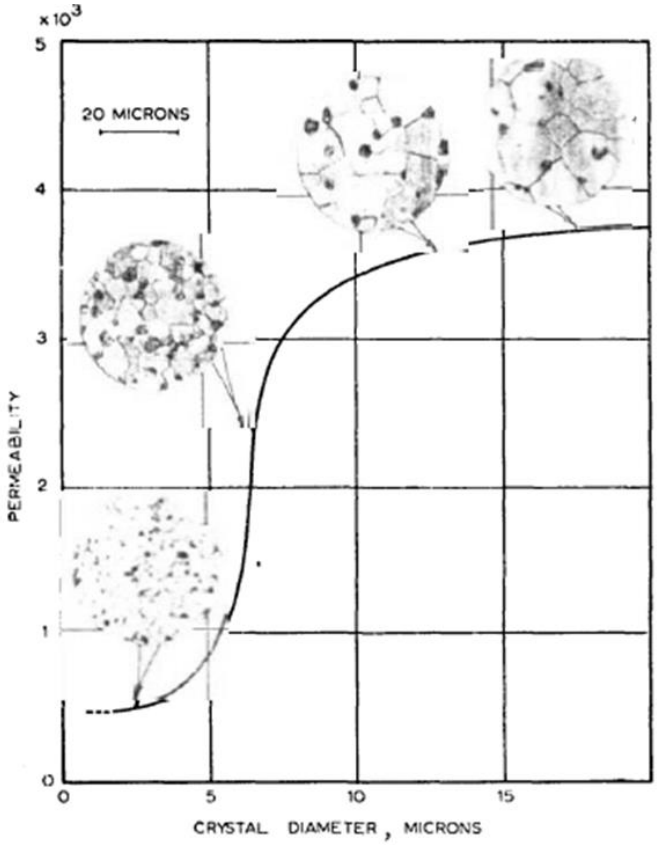


Figure 0.4 Variation of permeability with grain diameter in ferrites [46].

To improve the electrical and magnetic properties of Mn–Zn ferrites, doping of small amount of cationic substitutes is widely used. The grain growth, and thus the permeability of ferrites, is enhanced when the dopant concentration in the grains is above the solid solubility limit [44]. By either segregation to, precipitating on, or melting at grain boundaries, the dopants can affect the grain-boundary energy and therefore the driving force for grain growth[47].

Low-melting point insulating phases also increases the electrical resistivity of the material. As a consequence, this reduces the ohmic currents developed through the body of the material during operation under alternating currents and reduces the total power losses [48]. Practically, the most successful have been additions of Ti4+, Sn4+, Hf2+ , Zr4+ , Ni2+ , Cu2+ . Borated and alkali fluorides also have cations that promote sintering by forming a liquid phase at the grain boundaries and also increase the resistivity [47].

The permeability of ferrites does not change with frequency upto a critical frequency but decays rapidly beyond this critical frequency due to the onset of ferrimagnetic resonance as shown in Figure 2.5. According to Snoek's law [39], for a particular $M_s$, the larger the static value of $\mu_r$, the lower is the frequency at which this decrease occurs .

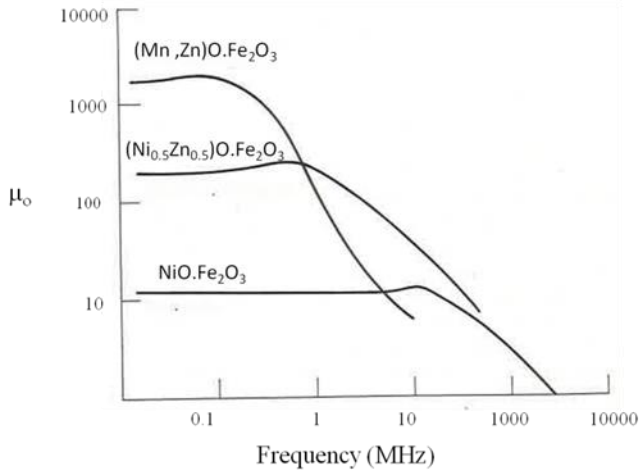


Figure 0.5 Variation of permeability with frequency in ferrites[42].

For emerging high-frequency consumer applications, ferrites suffer from several major disadvantages, including: 1) low saturation magnetization, $4\pi M_s < 3000G$ limiting the power density of the converters. This fundamentally limits the ability of ferrites to achieve a combination of high permeability and low magnetic losses at the frequency of interest. 2) low Curie temperature, (for Mn-Zn-ferrites, $T_c < 300\ ^oC$; for Ni-Zn-ferrite, $T_c < 400\ ^oC$), thus the current densities and operating temperatures have to be restricted to

control the inductor losses and stability; and 3) poor frequency response of magnetic properties due to their strong relaxation behavior. These limitations lead to millimeter size components and make ferrites unsuitable for emerging applications. In addition, traditional high-frequency magnetic materials such as ferrites also suffer from high process temperatures, thus making them incompatible with substrate integration. Currently, due to the lack of new innovations in magnetic materials, Ni-Zn-ferrites are widely used for discrete inductors in spite of their inferior properties.

### 2.3.2 Microcomposites

Metal-polymer composites have high resistivity resulting in lower eddy current losses while also retaining high permeability and saturation magnetization. In addition, microcomposites are more attractive for power-inductor cores because of their easier processing as toroids using powder compaction techniques. These composites constitute of metallic magnetic particles that are coated (or separated) by an insulating phase. Such magnetic powders in polymer paste form are commercially available from various vendors [27]. Microcomposite powder materials consist of different chemical elements in order to obtain the required resistivity and permeability of the inductor core. Metal composites also have a smoother reduction of permeability with frequency but it starts much earlier compared to ferrites. The permeability of the core depends on the size of the powder particles, with smaller particles giving lower permeabilities. Examples of these include iron and permalloy powders, which show permeabilities of 10-100 in the low MHz frequency range. However, the magnetic properties of these degrade even under mild magnetization force (e.g. 10% drop in permeability for 10 Oe) indicating lower power-handling capability. Further, these microscale composites show higher eddy current and domain wall losses.

Iron Powder Cores: Iron powder used in magnetic cores consists of pure iron, Fe, and is built up of small particles, which are isolated from each other. Iron powder saturates between 1-1.5 T and usually has a relative permeability ranging from 10-90. Iron powder compacts suffer from one major drawback. The binders used for isolating the grain particles, typically epoxy, are organic-based, and thereby are susceptible to instabilities during thermal aging . This increases the material's sensitivity for high temperatures, usually above 125◦C, and will cause the material to change its magnetic properties[43].

MPP ( Molypermalloy Powder) Cores: Molypermalloy powder, MPP, was introduced in 1940 and because of its high flux density, the core is very stable with DC current. MPP also has the lowest losses of all the powder materials when a higher saturation magnetization level is needed without increasing the losses. MPP cores consist of a mix of 2% molybdenum, 17% iron and 81% nickel and the relative permeability ranges from 14-550. The frequency spectrum varies from 200 KHz – 1MHz[26].

High flux Cores: High flux cores consists of 50% iron and 50% nickel powder and are used when very high saturation, 1.5 T, is needed . The losses are higher compared to MPP but much lower than the iron powder. High flux cores are the best powder cores in retaining high permeability when the DC-bias is increased. Because of the permeability of the material, high flux cores are smaller than the standard iron powder cores, which make it more suitable in applications where space is an issue. High flux cores have relative permeabilities between 14-160μ and a frequency stability up to 200 kHz [40].

Sendust Cores: Sendust cores, also called as Kool Mu cores, invented in Japan in 1936, consists of 85% iron, 9% silicon and 6% aluminum . They saturate at around 1T and they fit between iron powder and "High flux" cores when it comes to both losses and cost. The available relative permeabilities for Sendust cores are between 26-125μ. Sendust is

cheaper than both MPP and High flux because there is no nickel in the alloy, which makes the production process easier. The frequency range of operation is between 500 kHz - 1 MHz [42].

### 2.3.3 Nanomagnetic materials

Nanoscale magnetic materials are emerging to enhance the volumetric density and overcome the frequency-limitations with microscale materials. Reducing the structural correlation length of solids (e.g. crystalline or device sizes) on a nanoscale often brings about dramatic changes in their physical properties which are usually unpredictable from the classical point of view. Magnetic softening in ferromagnetic nanostructures is one of the examples of such size effects. These nanoengineered materials include nanostructured flakes, sputtered nanomagnetic thin-films and core-shell nanocomposite magnetic materials.

Nanostructured flakes: The first nanostructured magnetic materials were nanocrystalline alloys invented by Yoshizawa et al. from Hitachi Metals Laboratory [49] called Finemet with a nominal composition $Fe_{73.5}Si_xB_{22.5-x}Nb_3Cu_1$ (with usually $x$ = 13.5 or 16.5 at%). It consists of Fe-Si BCC crystallites, with 10-14 nm average diameter, embedded in the residual amorphous matrix. Other commonly available commercial nanocrystalline alloys are Nanoperm ($Fe_{84}Nb_{3.5}Zr_{3.5}B_8Cu_1$) and Hitperm ($(FeCo)_{88}Zr_7B_4Cu_1$). These nanocrystalline materials show excellent performance in the lower frequency ranges (100-500 KHz), making them ideal for transformers and common mode inductor chokes for inverter drives.

Most of the nanocrystalline alloys are prepared by rapid solidification followed by partial devitrification of an amorphous solid solution. The nanocrystallization process is

based on the overlapping action of nucleating (especially Cu) and grain-growth inhibiting element (Nb, with larger atomic diameter than iron)[34]. Figure 2.6 shows TEM micrographs highlighting the nanocrystalline structure of annealed Finemet alloy.

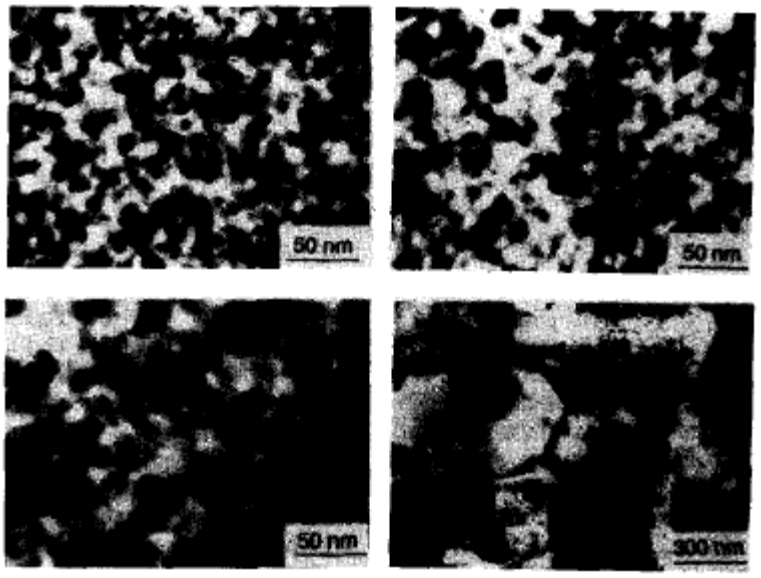


Figure 0.6 TEM micrographs of annealed Finemet nanocrystalline alloy[34]

The soft magnetic properties of nanocrystalline alloys has been explained with the phenomenon of magnetic exchange coupling by Herzer's model [50]. Herzer analyzed the scaling behavior of the magnetocrystalline anisotropy energy density of nanocrystalline materials based on a theoretical approach called random anisotropy model (RAM),which was originally proposed by Alben et al.[51] in 1978 for amorphous systems. Herzer's random anisotropy model explained experiments well and has become a guiding principle in development of soft magnetic nanostructured materials.

Herzer model: The most appreciable difference between classical and nanostructured ferromagnetic system lies in the effect of the grain size on the effective anisotropy relevant to the magnetization process. The magnetic properties of an assembly of small grains strongly depend on the counterplay of local magnetic anisotropy energy and

ferromagnetic exchange energy. For large grains, the magnetization can follow the easy magnetization directions in the single grain. Domains can also be formed within the grains. The magnetization process, thus, is determined by the magneto-crystalline anisotropy $K_1$ of the crystallites. For very small grains, however, ferromagnetic exchange interaction forces the magnetic moments to align parallel, thus, impeding the magnetization to follow the easy magnetization directions of each individual grain. As a consequence, the effective anisotropy for the magnetic behavior is an average over several grains and, thus, reduced in magnitude. According to the Herzer statement, when particle size (D) along with the distance (S) between particles is smaller than the exchange length ($L_{ex}$), exchange coupling takes place, which forces the magnetizations of particles to be aligned parallel, therefore, leading to a cancellation of the magnetic anisotropy of individual particles. The exchange coupling interaction, which leads to magnetic ordering within a grain, extends out to the neighboring environments within a characteristic distance, $l_{ex}$ which is ~20-30 nm for Fe or Co [52, 53]. The exchange interaction in nanocomposites also leads to the cancellation of magnetic anisotropy of individual particles and the demagnetizing effect, leading to higher permeability and lower coercivity. As a result, the average anisotropy $\langle K \rangle$ of the film, and hence the coercivity Hc, reduce considerably.

The critical scale, called the exchange length, below which this averaging mechanism takes place is given by

$$L_{ex} = \sqrt{\left(\frac{A}{K}\right)} \qquad (2.14)$$

where $L_{ex}$ is the exchange length, A and $K_1$ are the exchange constant and magnetocrystalline anisotropy constant, respectively. Due to exchange coupling, the effective anisotropy constant $K_{eff}$ due to averaging can be expressed as

$$K_{eff} = \frac{K_1}{\sqrt{N}} \qquad (2.15)$$

where N is the number of exchange coupled grains within the volume of $L_{ex}^3$ with grain size D, estimated as:

$$N = \left(\frac{L_{ex}}{D}\right)^3 \qquad (2.16)$$

The magnetic properties such as coercivity ($H_c$) and permeability ($\mu$) are a function of the magnetocrystalline anisotropy constant of the material. Coercivity ($H_c$) varies linearly with the magnetocrystalline anisotropy constant (K). Permeability ($\mu$) is inversely proportional to K. From these equations it can be seen that a large N will result in $K_{eff}$ <<K and hence effectively decreases $H_c$ and increases the magnetic permeability. Thus, the excellent soft magnetic properties of nanocrystalline magnetic materials is explained with the phenomenon of exchange coupling.

Stable permeability in a large frequency range can be accomplished in Finemet based nanocrystalline alloys by transverse induced anisotropy in ribbons. Owing to the brittleness of nanostructured Finemet alloys, powders down to 20 microns can easily be produced by grinding the ribbon samples into flakes without changing the nanostructure. The flake-shaped particles are molded in resin [54, 55] or solder glass [56] under pressure with eventual field-orientation of the flakes. The magnetic properties are related to the gap distribution and can be controlled by both the flake size and the compacting pressure with very good reproducibility. The largest permeability (6000) is obtained after hot-pressing of large flakes (1mm) with 5% solder glass, but this results in a low cut-off frequency (10 kHz) due to eddy current losses of the large particles. In contrast, the smallest permeability (ranging from 7 to10) is obtained after cold pressing of 20 micron flakes with 50% resin, and have the highest cut-off frequency (100 MHz) due to higher eddy current losses. Figure 2.7 shows the frequency-dependent permeability of Finemet

powder cores and stress-annealed ribbons and their variation with particle sizes. The frequency limit of permeability is not only due to eddy currents related to skin depth but also due to domain wall resonance and ferromagnetic resonance (FMR).

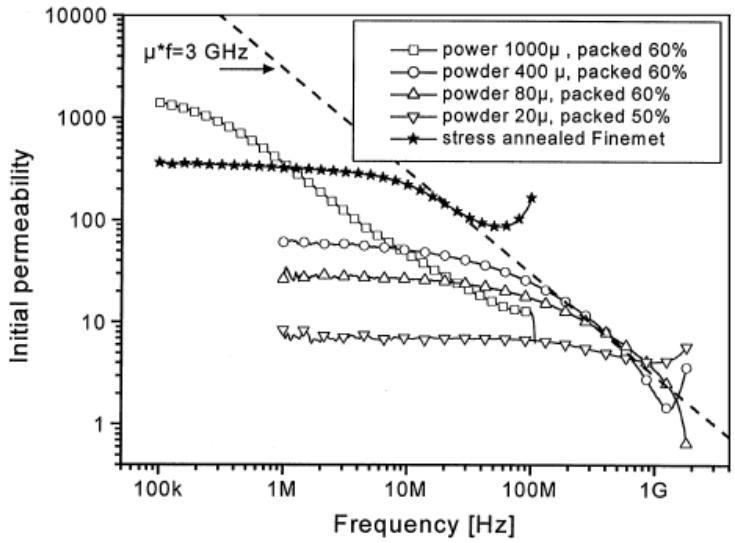


Figure 0.7 Frequency dependent permeability of Finemet powder composite cores for different particles sizes [34].

Certain brittle and metastable intermetallic compounds can be prepared by planar flow casting and then grinding the ribbon into powder, preserving its nanostructure obtained from rapid quenching. For example, silicon-rich iron ribbons can be crushed into micro-sized particles with nanocrystalline structure. Special interest is devoted to $Fe_2Si$, which exhibits a high resistivity of 220 mΩcm, due to its highly-disordered B2 metastable nanostructure (grain size~50 nm). The magnetic polarization is relatively low, 0.6 T, but sufficient in high-frequency applications. An appreciable permeability of 250 is maintained up to 10MHz [34].

**Sputtered nanomagnetic thin-films**: There is a wide interest in nanomagnetic thin-films developed by sputtering techniques in microinductor applications. Transition metal-metalloid alloy amorphous thin-films such as CoZrTa [12], CoZrNb [13,14], CoFeSiB [],

FeBN [15], CoHfTaPd [16,17] produced by sputtering are used in microinductor applications because they have soft magnetic properties, high permeability and high saturation magnetization. However, their resistivity is not too high (~100 μΩ· cm) to completely mitigate eddy current losses for thicker films (>5ums) at higher frequencies (>100 MHz). Figure 2.8 shows the permeability spectra over a range of frequencies for CoZrTa films of varying thickness.

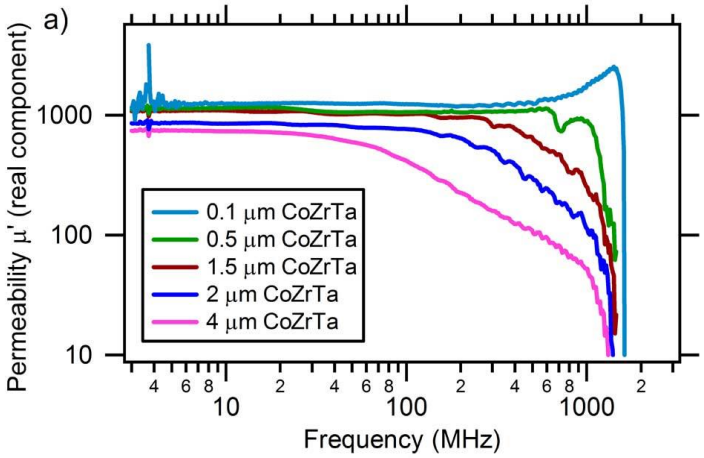


Figure 0.8 Permeability spectra of CoZrTa for varying film thicknesses[57]

Recently, a new type of sputtered nanogranular films consisting of ferromagnetic metallic nanoparticles distributed uniformly in an insulator matrix, have attracted much attention because of their excellent soft magnetic properties operating in the high-frequency range (up to GHz). The nanogranular materials consist of randomly-deposited nanograins of magnetic metals or alloys in a ceramic matrix commonly prepared by sputtering transition elements or alloys in the presence of gases such as $O_2$ and $N_2$. Figure 2.9 shows the TEM image of such a sputtered thin-film consisting of NiFe nanoparticles in an $SiO_2$ matrix. These films take the advantages of high permeability μ of magnetic metals and the high resistivity of insulators, making high μ and high ρ (~1000 μΩ-cm) possible in the same materials. The critical factor leading to good soft magnetic properties in these materials is the exchange coupling between magnetic nanoparticles, which can be

explained by extending the Herzer model to such materials. As the particle size is reduced down to the nanoscale, the particle size and exchange length converge, allowing for single domain states to stabilize. The magnetism and hence the magnetic properties of nanoparticles are predominantly dictated by the intrinsic properties of a material such as the anisotropy and saturation magnetization. The transition from multi-domain to single domain becomes very apparent when one considers the coercivity as a function of particle sizes as shown in Figure 2.10 [18]. As can be seen, the critical size of particles for single domain formation corresponds to a peak in coercivity below which there is a drastic coercivity reduction. Brown [19] has calculated the critical radius ($R_{c1}$) of the single domain according to the micromagnetics principle:

$$R_{c1} = \frac{3.6055}{M_s}\left(\frac{K}{\mu_0}\right) \qquad (2.17)$$

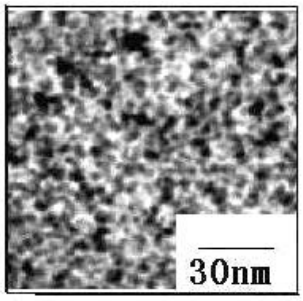


Figure 0.9 TEM image of NiFe (metallic) nanoparticles in $SiO_2$ (insulator) matrix[58].

where $M_s$, K and $\mu_0$ are saturated magnetization, magnetocrystalline anisotropy and vacuum permeability, respectively. As is well known, an assembly of single-domain ferromagnetic particles without interaction among particles usually possesses high $H_c$ and low permeability, due to the large magnetoanisotropy and demagnetization effect of individual particles.

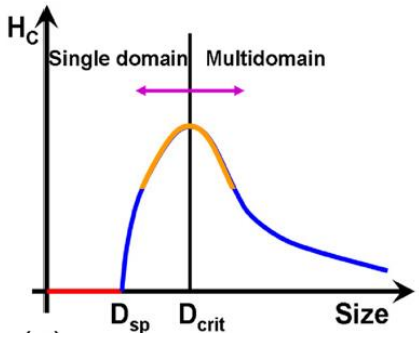


Figure 0.10 Variation of coercivity with particle size [20].

For nano-composites with single-domain particles, however, $H_c$ is very small. According to the Herzer model [21], described earlier in this section, when particle size (D) along with the distance (S) between particles is smaller than the exchange length ($L_{ex}$), exchange coupling takes place, which forces the magnetizations of particles to be aligned parallel, therefore, leading to a cancellation of the magnetic anisotropy of individual particles. As a result, the average anisotropy ⟨K⟩ of the film and hence the coercivity Hc reduces considerably. The condition to realize exchange coupling is $(D+S)<L_{ex}$.

Nano Fe-M-O and Co-M-O (M = Hf, Zr, Si, Al or rare-earth metal element) thin films have been successfully demonstrated via co-sputtering in a reactive gas mixture. These films have structure composed of (<10nm) magnetic nanoparticles surrounded by an amorphous insulator. It has been found that μ' for Fe- and Co-based nanocomposites thin films can be as large as 500 and with essentially flat frequency response up to 1 GHz [59, 60].

Dramatically different magnetic and electrical properties of these nanogranular thin-films can be obtained by changing the gas flow ratio during sputtering. For example, Figure 2.11 shows the dependence of saturation magnetization and electrical resistivity of CoFeHfO films on the gas flow ratio. When the gas flow ratio increases above 12%, a significant change in the properties is measured. At a gas flow ratio close to 15.4%, the

saturation magnetization attains a maximum value, and the coercivity of the film decreases and reaches its minimum of 0.3 Oe. Simultaneously, the resistivity of the film increases to 1700 μΩ.cm, more than a tenfold increase over the metallic Co–Fe–Hf film (approximately 100 μΩ.cm).

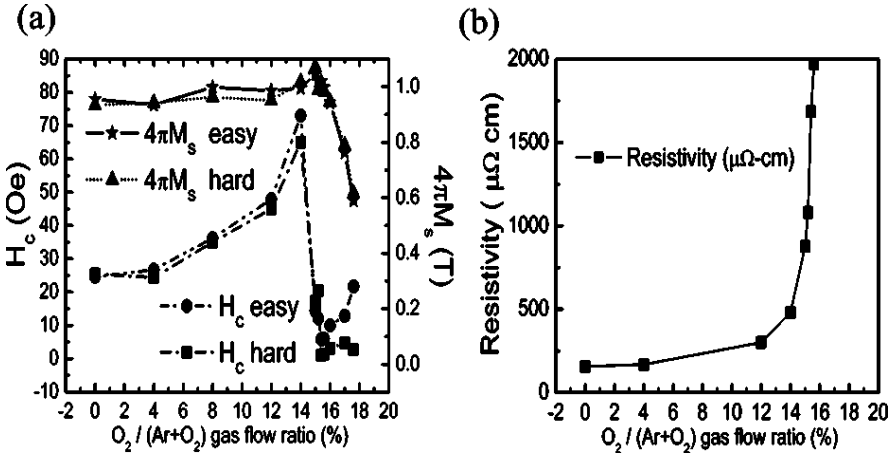


Figure 0.11 Dependence of magnetic and electrical properties of CoFeHfO films on gas ratio[61] .

The origin of such a significant change in these properties is studied by understanding the overall structural evolution using XRD. Films with varying flow ratio were grown and the structural evolution was compared as shown in Figure 2.12. At low gas-flow ratios, there is a broad peak corresponding to amorphous CoFeHfO. When the $O_2/(Ar+O_2)$ gas flow ratio increases, Hf atoms gradually dissolve out of the metallic Co–Fe–Hf material to form $HfO_2$ due to the strong affinity of Hf to $O_2$. This is evident by the formation of the $HfO_2$ peak in the XRD spectrum seen at the 12% gas flow ratio. This is also consistent with a continuous decrease in the lattice spacing of CoFe grains, because Hf atoms with a larger atomic size separate out of CoFe lattices. At a 15.4% $O_2$ there is a good phase separation between $HfO_2$ and CoFe, resulting in a stable CoFe (110) peak position and a minimum coercivity of Co–Fe–Hf–O film. Additional increase in the oxygen content (16%) causes oxidation of CoFe grains denoted by reduced diffraction intensity and degradation of magnetic properties.

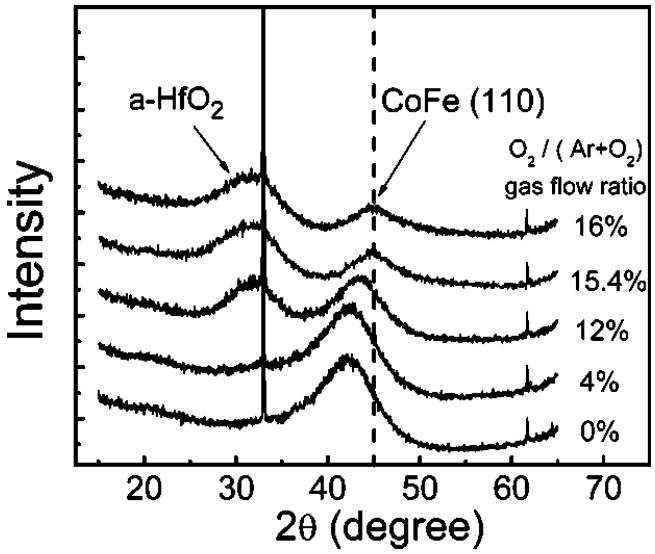

Figure 0.12 XRD spectra of CoFeHfO films with varying gas flow ratio [61].

**Core shell nanocomposites**: Nanoparticle composites in polymer matrices are also synthesized via chemical synthesis routes to improve frequency stability and reduce losses compared to their microstructured counterparts [53, 62-67]. The core-shell nanocomposite materials are chemically synthesized by coating nanosized magnetic particles with insulating spherical shells of $SiO_2$ or $Al_2O_3$. The techniques successfully applied for the preparation of the above mentioned granular and core-shell nanocomposites are: reduction of metal oxides, hydrothermal precipitation, sol–gel processing of Fe–$SiO_2$ [68], Ni–$SiO_2$ [69] , Fe–$Al_2O_3$ [70] , ball-milling of FeCo–$SiO_2$ [71], Fe–$SiO_2$ wet-chemistry method [72, 73]. Co-$SiO_2$ or Ni-$SiO_2$ nanocomposite samples, for example, are reported to have a permeability of 15 and a flat-frequency response up to 1 GHz. Permeability of 30 was also reported from Permalloy ($Ni_{47}Fe_{53}$) encapsulated with Ni–Zn ferrite. These systems showed magnetic relaxation at 1 GHz [37] which is 10X higher than traditional metal composites or ferrites. However, the permeability and frequency-stability of chemically synthesized metal nanoparticle-insulator nanocomposites are much inferior to those of the sputtered films and do not meet the property requirements for power inductor applications.

### 2.3.4 Metal laminates

Most magnetic materials deposited by sputtering and electroplating, have low resistivity. Thus the eddy current losses dominate at high frequencies. It is well known that the eddy current loss can be suppressed when the thickness of the magnetic layer is smaller than the skin depth. Therefore, in order to reduce the core loss at high frequency, while maintaining sufficient core thickness, multilayered cores are used. In bulk magnetic devices, low loss lamination cores are typically achieved by stacking alternating layers of a core material and an insulating material.

To overcome the limitations with metal-based thick films, magnetic cores made of sequentially deposited, alternate layers of metal-polymer or metal-oxide structures have been designed to achieve higher permeability than microcomposites, while simultaneously achieving higher power-handling capabilities. Highly-laminated, low-profile magnetic cores with micron-scale laminations and high power handling (~1W) have been demonstrated using high-permeability metallic alloys [20]. Various processes such as mechanical laminations made by hot pressing or horizontal laminations using electroplating{Park, 1999 #11} and sequential sputtering [10,11] have been demonstrated. Example of a laminated magnetic core formed by electroplating is shown in Figure 2.13. The electroplated laminate process involves core fabrication by sequential electroplating, followed by etching of sacrificial layers to achieve micron-level laminations that cannot be attained using mechanical laminations. This process does not require the expensive vacuum steps involved in horizontal sputtering . The laminations are very thin and the core has very low eddy current loss as the electrical resistance of each lamination is very high compared to the bulk core. However, fabrication of integrated inductors with such laminated cores is very complex.

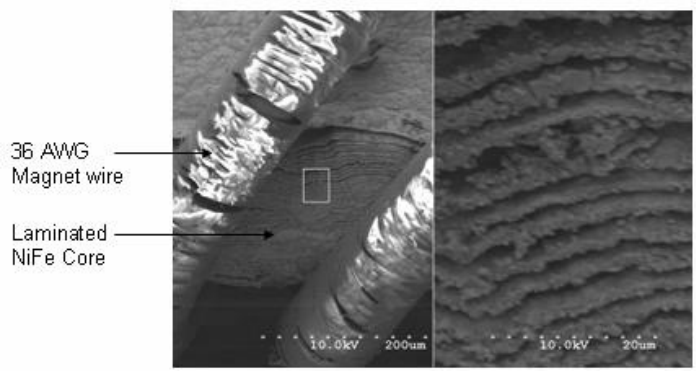


Figure 0.13 Laminated core formed by electroplating and sacrificial etching{Park, 1999 #11}.

Sputtered nanolaminated magnetic cores, formed by sequential alternate sputtering of magnetic and insulating layers, have high permeability at large frequencies and thus can be used to achieve high inductance density. High-resistivity magnetic alloy materials such as CoZrTa [14], CoZrNb [15, 23], CoFeSiB [16] are sputtered as the magnetic layers owing to their higher resistivity compared to NiFe. However, their resistivity is still quite small (~100 μΩ· cm) to mitigate eddy current losses completely. The eddy current losses will degrade the high-frequency performance of the magnetic inductors using these alloy materials as the magnetic core. These losses can be reduced by depositing insulating layers of AlN or $SiO_2$ between the two magnetic layers, thus forming multilayered films such as CoZrNb/AlN [24] and CoFeSiB/SiO2 [25]. However, the multilayered structures involve complex processes that may make fabrication difficult.

## 2.4 Integrated Power Inductors in DC-DC converters

Several approaches are pursued to miniaturize and integrate power inductors in packages, boards or on silicon. These approaches are based on the type of magnetic films used to enhance the flux density or power density. This section categorizes these approaches into two classes: spiral inductors and toroidal inductors. Spiral inductors enclose planar (spiral) coils with a magnetic material. In the toroidal approach, the conductor is wrapped around a planar magnetic core using metal windings. Figure 2.14 shows the schematic designs of spiral and toroid inductors.

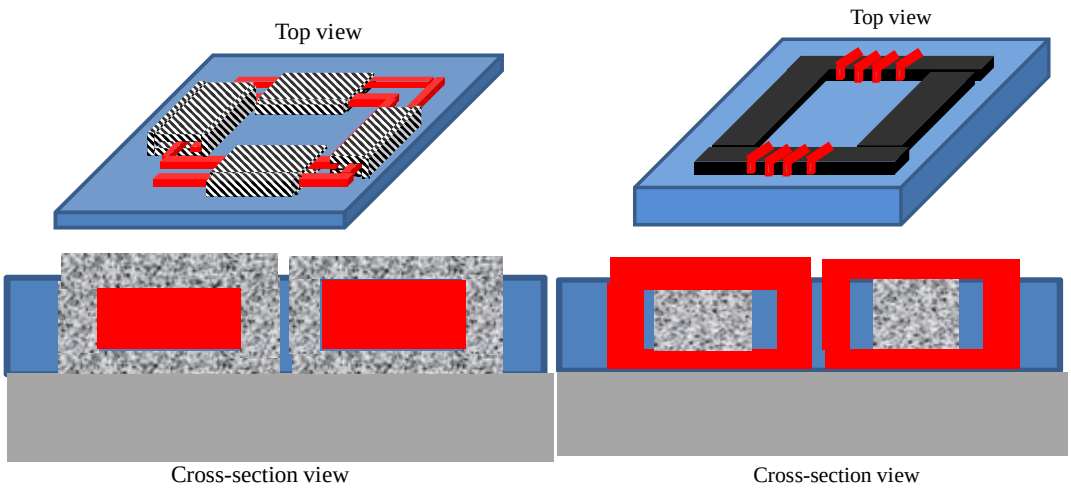


Figure 0.14 Schematics of inductor designs: (a) Racetrack inductor; (b) Toroid inductor

The most common spiral inductors utilize: a.) magnetic cores, b.)nonmagnetic substrates, or c.)sputtered magnetic films, d.) nonmagnetic cores (referred to as polymer or air core). The toroidal inductors utilize cores of a.)polymer, b.)electroplated metal, c.)electroplated metal laminate, or d.)printed inductor cores. This section reviews these different types of integrated inductors. Figure 2.15 shows the classification of these approaches.

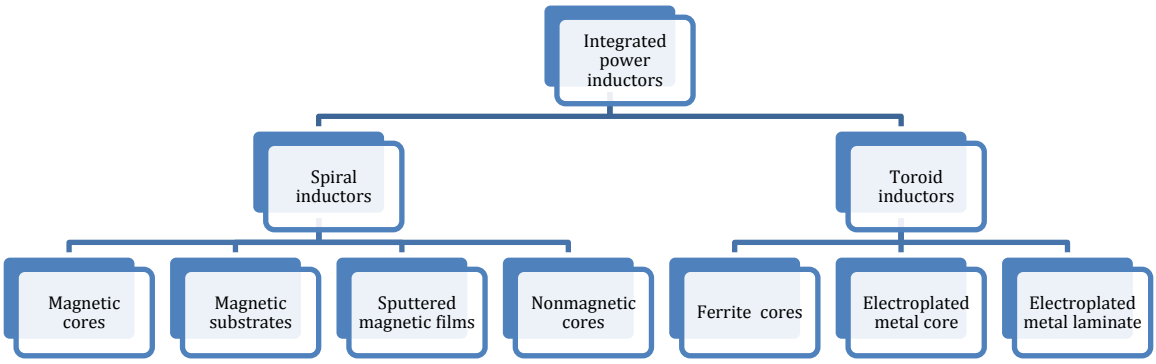


Figure 0.15 Classification of integrated power inductors

### 2.4.1 Spiral inductors

**Spiral Inductors with Magnetic cores:**

Spiral inductors with laminated ferrite cores: In such integrated inductors, the spiral coils are fabricated by microfabrication technologies, while the magnetic cores are fabricated separately. They are assembled to form hybrid inductors. Figure 2.16 shows a laminated hybrid inductor, in which the coils were fabricated on a polyimide film.

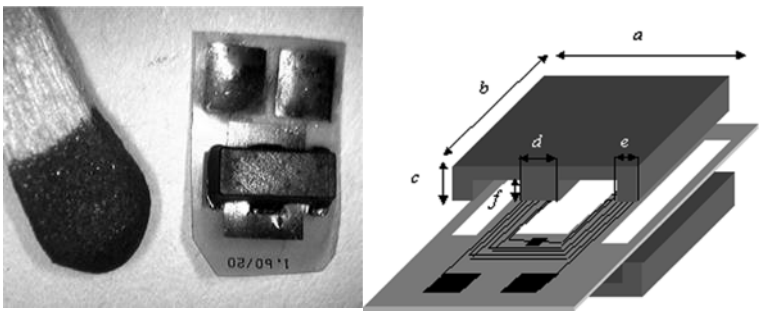


Figure 0.16 Hybrid inductors with planar coils assembled with two ferrite laminate cores [74].

Spiral Inductors on Printed Circuit Board (PCB) with metallic magnetic cores: In this approach, both coils and magnetic cores are fabricated in PCB, as shown in Figure 2.17. The coils are fabricated by patterning the copper layers on the PCB. Magnetic materials are added to boost the inductance. These can be ferrite polymer compounds (FPC) [75,

76], or electroplated CoNiFe [77], NiFe [78]. The PCB is used as a packaged substrate for other components. This approach takes full advantage of the PCB for inductor fabrication. However, they do not meet the size and performance targets for many applications [79].

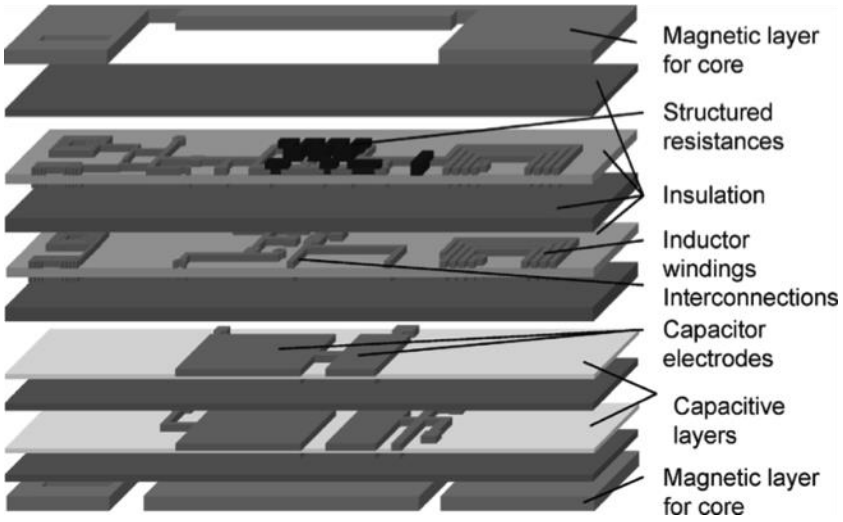


Figure 0.17 Perspective review of PCB with integrated inductors and capacitors [76]

Spiral Inductors with Low Temperature Co-fired Ceramic (LTCC) ferrite cores: Low temperature co-fired ceramic (LTCC) is a well-established multi-layer technology, which has been in use for many years in the microelectronics packaging industry for multichip modules, RF components or modules. The fabrication process of LTCC inductors is quite similar to the PCB approach described earlier except that it starts with LTCC tapes and is sintered at 700~900℃ after being stacked. Each of the LTCC layers is processed in parallel as particulate tapes and brought together in an accurately aligned stack prior to firing. For inductors made from LTCC process, the standard glass-ceramic dielectrics are replaced with magnetic materials such as NiCuZn [80, 81] or NiZn ferrites[82]. Although the permeability of ferrite powder composites increases after firing, the achievable thickness of LTCC ferrite inductors is smaller than that of PCB inductors. Figure 2.18 shows a fully integrated DC-DC converter with an LTCC inductor.

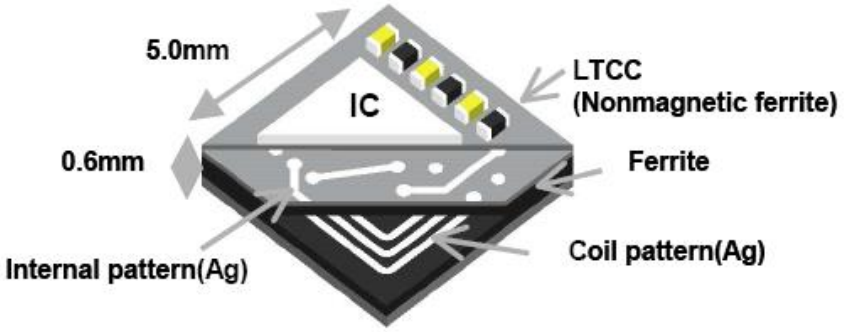


Figure 0.18 Demonstration of fully integrated DC-DC converter with LTCC inductor [80]

Spiral inductors with printed metal-polymer composites: In order to combine the favorable properties of magnetic materials with simple processing sequences, small particles of magnetic materials are suspended in a nonmagnetic matrix or binder [83, 84]to synthesize a paste. The paste is then screen-printed to form the inductor core. For example, 1.2 μm NiZn ferrite particles and 0.8 μm MnZn ferrite particles are mixed with polymers such as polyimide to form the paste. The mixtures were coated and patterned by screen printing and were cured at 160-300°C. The resistivities of the fabricated magnetic components were 0.01MΩ·cm for NiZn-based composite and 1MΩ·cm for MnZn-based composite. The saturation flux densities are 0.43 T and 0.28 T respectively. However, without high-temperature sintering, the permeabilities are relatively low, ~ 25 for NiZn based composites and 32 for MnZn based composites respectively. Thus, the resistivity of the fabricated micro magnetic core is increased dramatically at the expense of relatively low saturation flux density and low permeability. Figure 2.19 shows an integrated inductor with the composite of ferrite powder and polymer bonder.

Compared to electroplating and sputtering, the fabrication process is much simpler and offers flexibility in selecting the magnetic material. First, the composite is screen printed on the substrate. Photoresist molds are then created, followed by electroplating copper windings. Next, the molds and seed layers are removed and the composite is screen

printed on the top again to finish the fabrication. The reported inductance densities were 300~500 nH/mm$^2$ and remained constant up to 10 MHz.

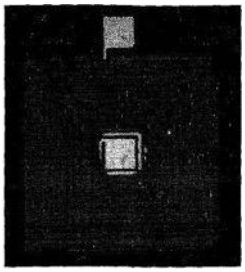

Figure 0.19 Integrated inductors based on ferrite-polymer composites [82]

**Spiral Inductors on Magnetic substrates:**

Spiral Inductors on Ferrite Substrates: Instead of adding magnetic materials onto the substrate, magnetic substrates have been directly used for inductor integration [85]. Similar to the PCB and LTCC approaches, this approach also takes the full advantage of the space available on the packaging substrate. Furthermore, it removes the space of additional magnetic material. Spiral coils are deposited on a Ni-Zn ferrite substrate, and then are covered by a composite composed of Mn-Zn powders and a polymer binder as shown in Figure 2.20.

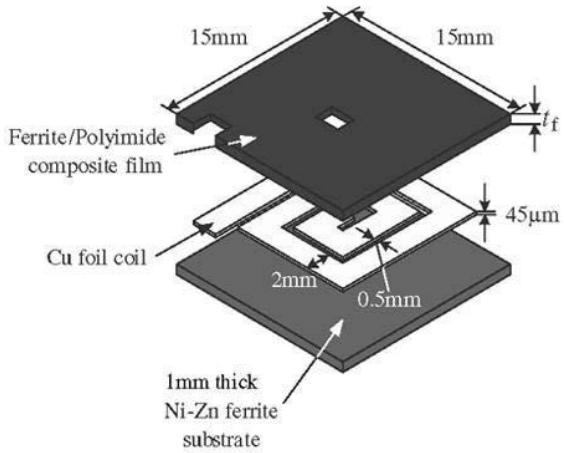


Figure 0.20 Spiral inductors on magnetic substrates [83].

Spiral Inductors with Sputtered Magnetic Films: Sputtered CoHfTaPd films were used as

the magnetic cores for inductors on the top of power MOSFETs. Monolithic DC-DC converters were thus demonstrated by Fuji Electronics [19]. The inductor consists of two 9 μm sputtered magnetic plates with a 35 μm thick spiral copper winding sandwiched in the between as shown in Figure 2.21.

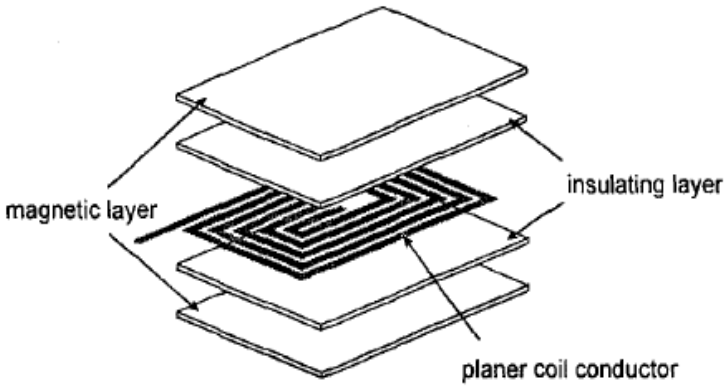


Figure 0.21 Schematic of a thin film inductor that was monolithically integrated on a power IC [84].

In the pioneering work on on-chip power inductors by Intel Corp., Co-Zr-Ta nanolaminates with spiral coils showed 10X higher inductance densities than the state-of-the-art. Their work demonstrated that nanolaminates can increase the roll-off frequency from 300-800 MHz. These inductors take advantage of the uniaxial magnetic anisotropy for higher frequency stability and current-handling[86]. Figure 2.22 shows integrated inductor on 130 nm CMOS Si. The magnetic plates are 2 μm thick CoZrTa, deposited by sputtering. Inductor wires were prepared by electroplating 5 microns of copper on top of a 0.5 um-thick $SiO_2$, isolating the copper from the first CoZrTa level. Polyimide was then deposited over the copper to planarize the surface before the deposition of a second level of CoZrTa. Magnetic vias were formed to connect the top and bottom magnetic material. The inductances were boosted 9 times compared to the corresponding air core inductors and upto tens of nH inductance can be achieved. These inductors are intended for

applications with switching frequencies of above 100 MHz.

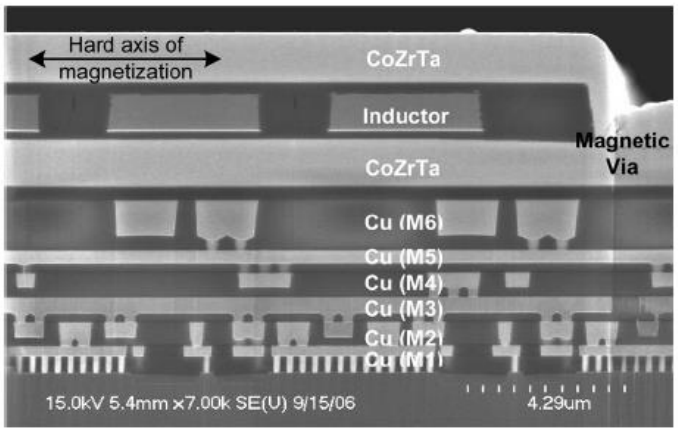


Figure 0.22 Cross-section view of inductor integrated on 130nm CMOS [57]

Spiral v-groove inductors with sputtered magnetic films: Figure 2.23 shows the cross-section of a V-groove inductor, which is a straight-line copper wrapped by a sputtered magnetic material. This inductor has very small DC resistance due to its large cross-section area, but it took a 11 mm length to obtain 8 nH[87].

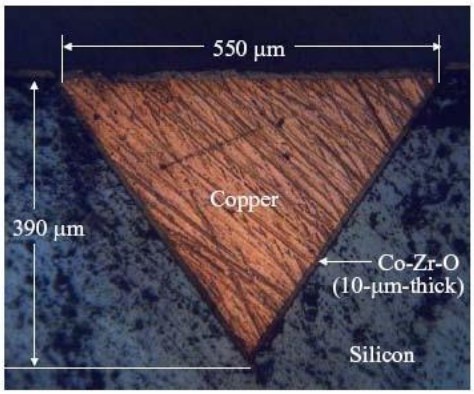


Figure 0.23 Cross-section of a V-groove inductor with sputtered magnetic core [87]

Power inductors with sputtered magnetic materials have several limitations in spite of their superior properties. First, in order to control the film stress, they cannot be made thicker than 10μm. Second, the sputtering deposition rate is very low, generally ~0.1nm

per second, which results in long deposition times. Third, the resistivities of most sputtered alloys are low. Therefore, isolation with insulating oxides is required to suppress the eddy current loss. For example, 7 layers of 1.8 μm CoZrTa are isolated with 0.2 silicon oxide isolation to form a 14-μm thick magnetic core. This introduces fabrication complexities and suppresses the sputtering throughput.

**Spiral Inductors with Nonmagnetic Cores:**

Nonmagnetic inductors are popular for realizing integrated inductors due to their relatively simple structure and easier integration. They are widely used in RF circuits. They have limited applicability in power converters due to their lower inductance.

Advanced IC technologies allow power MOSFETs to switch at extremely high frequency (over 100MHz) with acceptable switching loss[88]. At such high frequencies, small inductances in nH scale can meet the requirements of DC-DC converters in portable electronics. Thus, for such high frequencies (>100 MHz), nonmagnetic spiral inductors can easily be realized on power-IC chips, with acceptable inductance values and Q-factors. The most common example of this is the integrated spiral inductors in Intel's Haswell processors .

Nonmagnetic core inductors on chip are generally spiral inductors with metal layers. Spiral inductors by CMOS technology suffer from high resistance due to the thickness limitation of the interconnection metal layers. It is well-known that in-plane spiral inductors generate losses on silicon substrate. To address this limitation, out-of plane spiral inductors were realized as shown in Figure 2.24, by post-CMOS technologies to reduce the substrate loss. The inductor was fabricated in-plane first and then was pulled out-of-plane by external magnetic force. Because of the plastic deformation, the inductor stayed out-of-plane after the release of the external magnetic force [56].

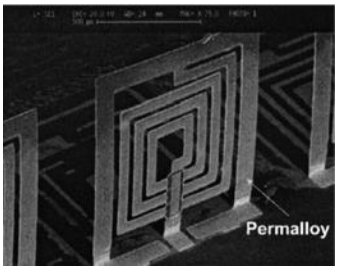

Figure 0.24 Out-of-plane air-core inductor by plastic deformation and magnetic assembly [56].

### 2.4.2 Toroid Inductors

Another important direction in fully-integrated DC-DC converters is to integrate toroidal inductors by microfabrication technologies. Unlike spiral inductors with a typical single-layer metal pattern, toroidal inductors require two metal layers with vias, which increases the fabrication steps. The following sections review toroid inductors in different categories based on the magnetic materials used for inductor cores.

Toroidal inductors with ferrite substrate cores: In this approach, through-substrate holes are punched on a magnetic ferrite substrate and then copper is electroplated through the holes. After the inductor is fabricated on the substrate, the inductor is stacked with a power IC chip and packaged[57]. An example of toroidal inductors with ferrite core is shown in Figure 2.25.

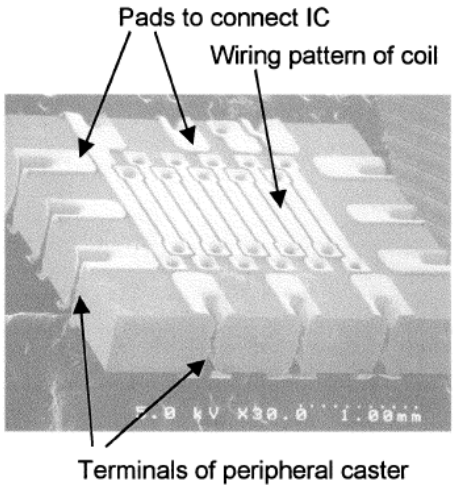


Figure 0.25 Toroidal inductor on ferrite substrate[57].

Toroidal Inductors with Electroplated Metal Cores: Although both spiral and toroidal inductors are used with electroplated magnetic materials, toroidal cores are preferred because of their higher power densities. The fabrication process starts with electroplating of the bottom metal. The isolation layer is then coated, followed by electroplating the magnetic core layer, and electroplating of vias. The final step involves formation of the top metal layer[22]. Figure 2.26 shows a microfabricated toroidal inductor.

Most inductors with electroplated magnetics use NiFe alloys as the magnetic core. However, they show high loss and low permeability at high frequencies. An improved material, CoNiFe, has been reported to have better saturation flux density and higher resistivity [89], and it has been used for integrated high-frequency inductors [77].

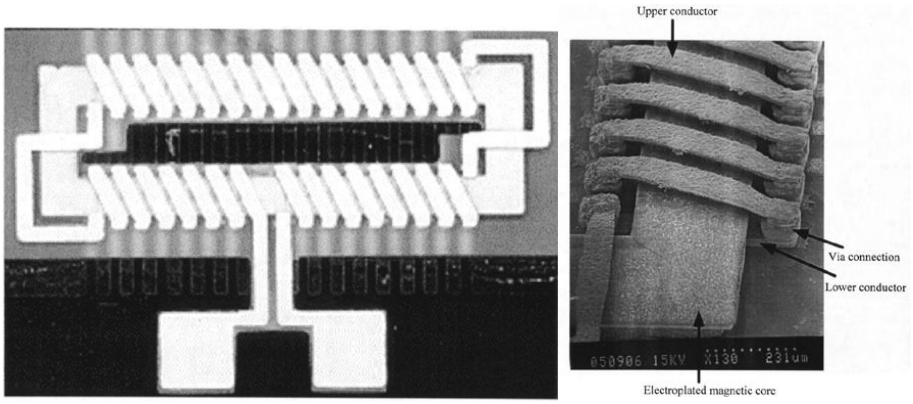


Figure 0.26 A micro fabricated toroidal inductor with electroplated NiFe [22]

Toroidal Inductors with Electroplated Metal Laminate Cores: Laminated multilayered magnetic cores reduce the eddy current losses at high frequencies, while maintaining sufficient core thickness for power handling. Several approaches have been proposed and demonstrated for different type of laminated cores. One such example involves laminated cores by repetitively depositing polymer insulator, seed layer, and electroplating magnetic metal layers[20]. This approach is a cumbersome process, which needs many transfers between an electroplating bath and a deposition chamber. Further, it needs many photolithography steps and each seed layer must be removed after the corresponding electroplating. An all-aqueous-based electro-chemical process was reported for laminating magnetic cores using an electrodepositable, dielectric photoresist, as shown in Figure 2.27. The seed layers were deposited by electroless plating after photoresist surface activation. In this process, only one mask is needed for the first layer. The following layers were selectively deposited. No seed layer removal was required. However, the seed-layer electroless plating needed additional surface treatment, making this a cumbersome process [81].

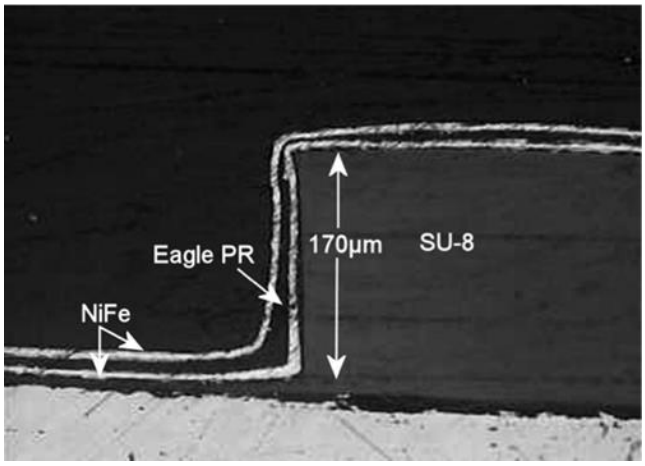

Figure 0.27 Laminated NiFe core by all aqueous-based electro-chemical process [81].

By alternately depositing NiFe and Cu layers, followed by Cu removal, Park et al. fabricated another class of laminated cores [90], as shown in Figure 2.28. In this process, only one mask was used, and no surface treatment was required. However, sacrificial Cu layers must be removed to obtain multilayered structures. Based on the same idea, Leith et al. fabricated laminated cores by alternatively electroplating nickel-rich and iron-rich NiFe alloy layers and then removing the iron-rich layers by potential-enhanced acid etching [91]. Therefore, all the electroplating processes of the core were carried out in the same bath. The sacrificial layers were electroplated by varying the electroplating conditions.

In addition to lateral or horizontal laminations mentioned above, vertical laminated cores were also demonstrated in two ways: partially filled trenches and fully-filled trenches[92]. Through-wafer silicon trenches were created by DRIE and used as an electroplating mold. In partially-filled trenches, magnetic core layers were electroplated on the sidewall of the silicon trenches, and the core layers are separated by silicon and oxide gap. In the fully-filled trench method shown in Figure 2.29, the wafer with through-wafer trenches was attached to another wafer with a metal seed layer. The vertical core layers were filled into the vertical through-wafer silicon trenches.

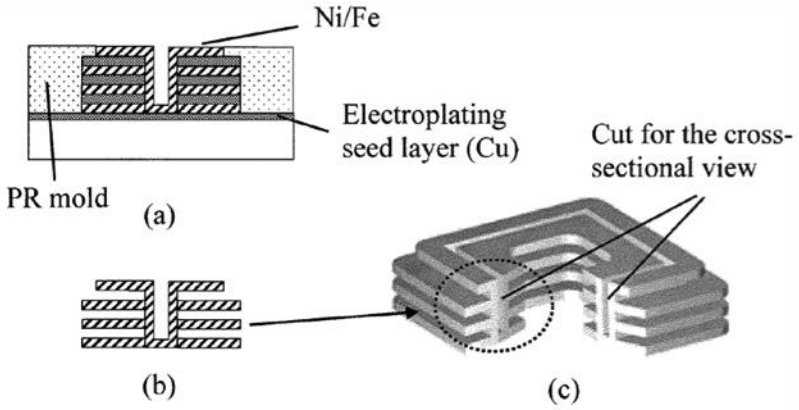

Figure 0.28 Schematic of laminated NiFe core by using copper as sacrificial layer[20].

The primary advantage of this approach is that all the laminated vertical core layers were fabricated in one electroplating step at the same time and no sacrificial layer removal is needed. However, in this case of vertically-laminated structures, the required aspect ratio of the laminations is high, making fabrication difficult.

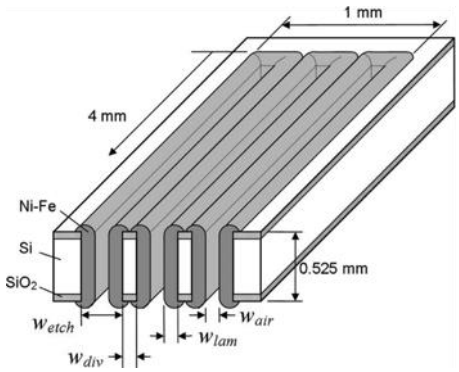

Figure 0.29 Schematic of laminated NiFe core by electroplating through vertical Si trenches[92] .

## 2.5 Summary

Inductors are typically the largest components in a power converter. They also play a key role in determining the efficiency of the converter. Traditional inductor technologies are limited to discrete ferrite inductors in spite of their low volumetric density. Ferrites have low Ms limiting their power density and poor frequency response of magnetic properties. Advanced magnetic materials such as metal composites have emerged to enhance volumetric density, albeit their much higher losses. Nanomagnetic materials are being explored to achieve both high power density and high Q. However, the process complexity, geometry constraints and cost are still slowing their widespread use. Achieving high $\mu$, high Ms, and low loss at high frequencies (1-10 MHz) in ultra-thin form factor (50-100 microns) for next generation inductor technologies is still a challenge for today's magnetic materials. The novel multilayered composite approach is proposed in this thesis to achieve a high $\mu$, high Ms, and low loss magnetic structure, thus overcoming the challenge. Chapter 2 and 3 describe the modeling, design, fabrication and characterization of such multilayered composite structures.

Next generation power inductors need to replace today's bulky discretes and be integrated with the active components in a miniaturized and ultra-thin form factor. Planar inductors are integrated with two key topologies: spiral and toroidal inductors. Spiral inductors are more widely used because of their ease of fabrication while toroidal inductors offer higher power densities. However, integration of high performance magnetic materials to form ultra-thin inductors is still limited by geometry and processing requirements. To overcome this challenge, Chapter 5 describes the design and fabrication of ultra-thin Si-integrated multilayered composite inductors by patterning the multilayered composite structure and forming coils around it.

# CHAPTER 3

# MODELING AND DESIGN OF MULTILAYERED MAGNETIC COMPOSITE STRUCTURES

Multilayered metal-polymer composite structures are explored as innovative magnetic cores for high-density power inductors, as outlined in Chapter 1. The structure is recaptured in Figure 3.1. The primary focus of this chapter is to: 1) Model the impact of material and geometry parameters on the frequency-dependence of permeability, and 2) Arrive at design guidelines for the geometry of the multilayered composite structures. Three candidates with high satuation magnetization (Ms) and low coercivity are selected for the metallic magnetic layers. Analytical equations and 3D electromagnetic (EM) simulations are used to model and design the multilayered metal-polymer composite structures for high μ in the desired frequency range (1-10 MHz).

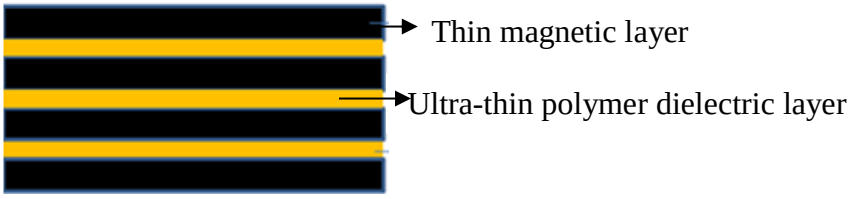


Figure 0.1 Schematic cross-section of multilayered composite structure

## 3.1 Analytical modeling

To achieve high μ with low losses, in the desired frequency range (1-10 MHz), the thickness of each magnetic metal layer has to be maintained such that it is thinner than the skin depth, computed using Equation (1) [28]:

$$\delta = \sqrt{\frac{\rho}{\pi f \mu}} \qquad (3.1)$$

where δ is the skin depth, f is the frequency, ρ is the resistivity and μ is the intrinsic permeability of the magnetic material. Thinner magnetic layers reduce the eddy current loss and enable frequency-stability of permeability. The first step in material modeling is to compute the skin depth of the ferromagnetic layer in the composite structure for the frequency range of interest. This determines the thickness of the magnetic layer in the multilayered structure for a stable permeability at high frequencies. Three magnetic materials, NiFe, NiFeMo and CoZrO are chosen as candidate materials for the ferromagnetic layer, because of their high Ms (0.8-1 Tesla) and low coercivity (< 1 Oe). Table 3.1 shows the computed skin depth of the magnetic materials at 10 MHz.

Table 0.1 Computed skin-depth of magnetic materials

| **Material** | **Permeability** | **Resistivity (micro-ohm-cms)** | **Skin depth (microns) @10 MHz** |
|---|---|---|---|
| NiFe | 1000 | 14 | 2.25 |
| NiFeMo | 800 | 59 | 4.83 |
| CoZrO | 200 | 300 | 27.57 |

### 3.1.1 Effect of magnetic layer thickness

The effective permeability due to eddy current screening for an infinitely wide magnetic film can be obtained using Maxwell's equations as [93]

$$\mu = \mu_i \frac{2\delta}{(1+j)d} tanh \frac{(1+j)d}{2\delta} \qquad (3.2)$$

where $\mu_i$ is the intrinsic relative permeability, d is the film thickness and δ is the skin depth. Figure 3.2 plots the variation of permeability with frequency for different thicknesses of NiFeMo films, using Equations 3.1 and 3.2. Similar plots are shown for NiFe and CoZrO films in Figure 3.3 and Figure 3.4 respectively. The frequency roll-off of permeability is assumed to be only due to eddy current losses in the desired frequency range. The plots indicate that all the materials have stable high permeability upto 10 MHz for magnetic layer thickness below 2 μm. Based on this analysis, the thickness of the magnetic layer was selected to be 2 μm, which is less than the skin depth at 10MHz for

all the three materials. Decreasing the magnetic layer thickness increases the frequency stability of permeability in all the three cases.

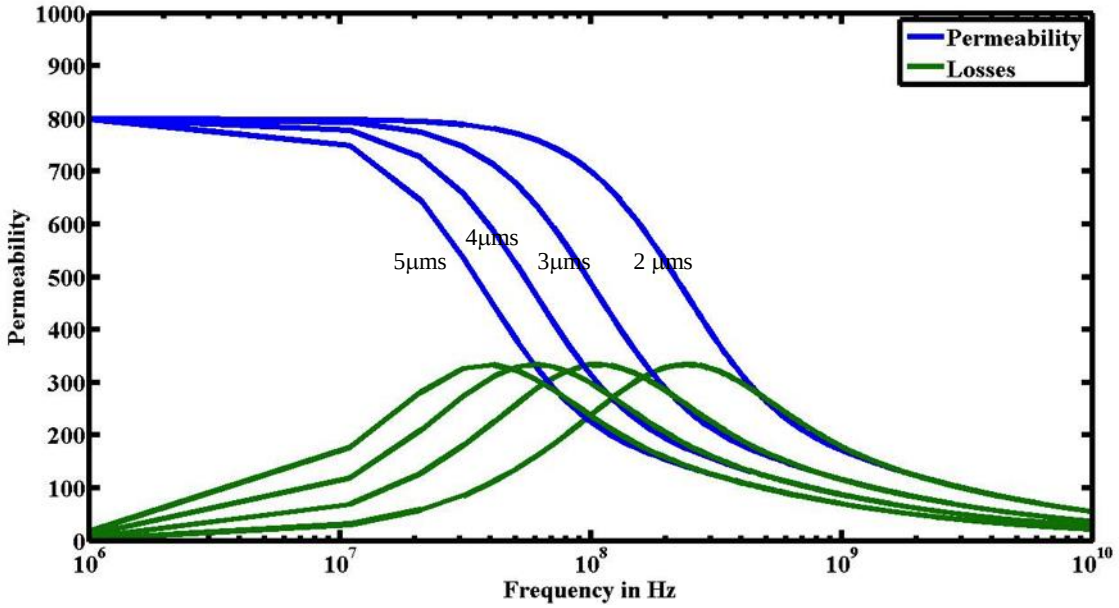


Figure 0.2 Variation of permeability and loss for different thicknesses of NiFeMo layers.

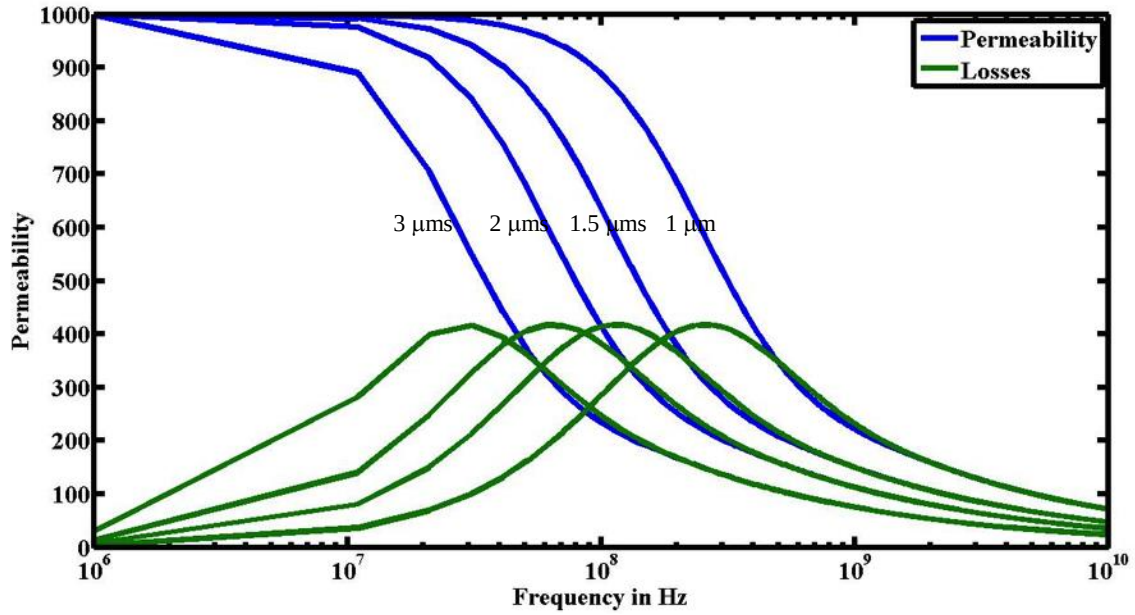


Figure 0.3 Variation of permeability and loss for different thicknesses of NiFe layers.

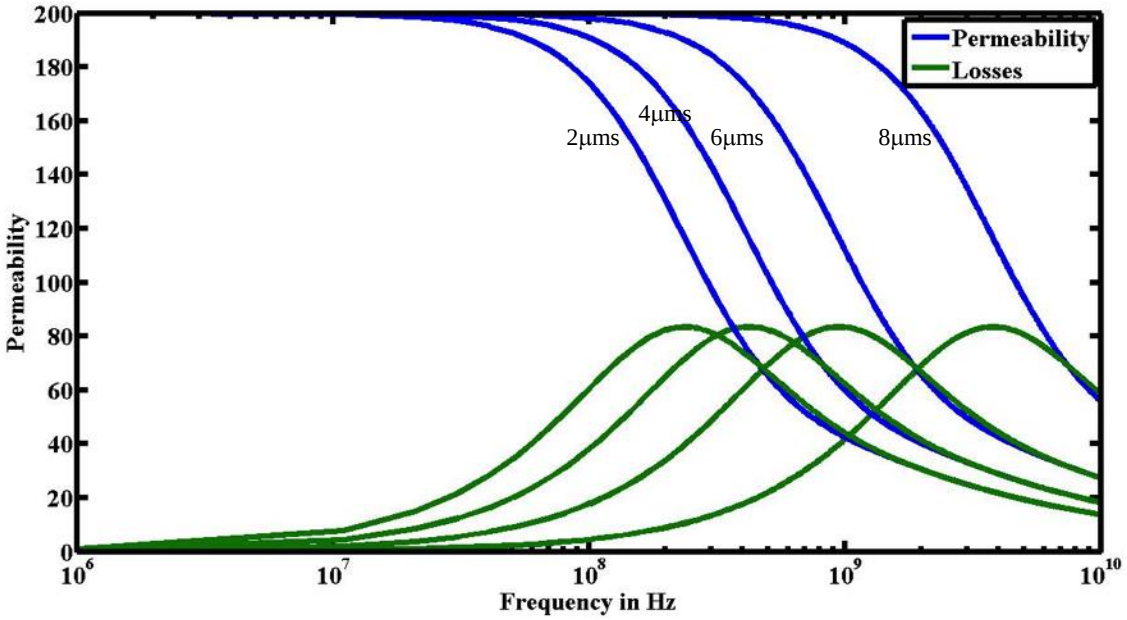


Figure 0.4 Variation of permeability and loss for different thicknesses of CoZrO layers.

### 3.1.2 Effect of polymer thickness

The thickness of the polymer layers affects the $M_s$ and permeability of the composite structures. The effective $M_s$ of the structure can be computed as[42]:

$$Ms_{eff} = q\, Ms_i \qquad (3.3)$$

where $Ms_{eff}$ is the effective saturation magnetization of the composite, q is the volume fraction of the ferromagnetic layers and $Ms_i$ is the saturation magnetization of the individual magnetic layers. Thus, it can be seen that higher effective composite $M_s$ can be achieved with lower polymer thickness.

## 3.2 3D Electromagnetic (EM) simulation based models

The frequency-dependent permeability of the multilayered composite structure is also estimated by extracting the reflection coefficients for a shorted- strip transmission line using full-wave electromagnetic (EM) simulations. The reflection coefficients are directly related to the effective permeability and loss of magnetic materials. The EM simulation

of the shorted strip-line is performed using SONNET EM solver software. Figure 3.5 shows a schematic design of the strip-line being modeled. As shown in the figure, the magnetic film, placed underneath the shorted strip-line, causes changes in the reflection loss coefficients.

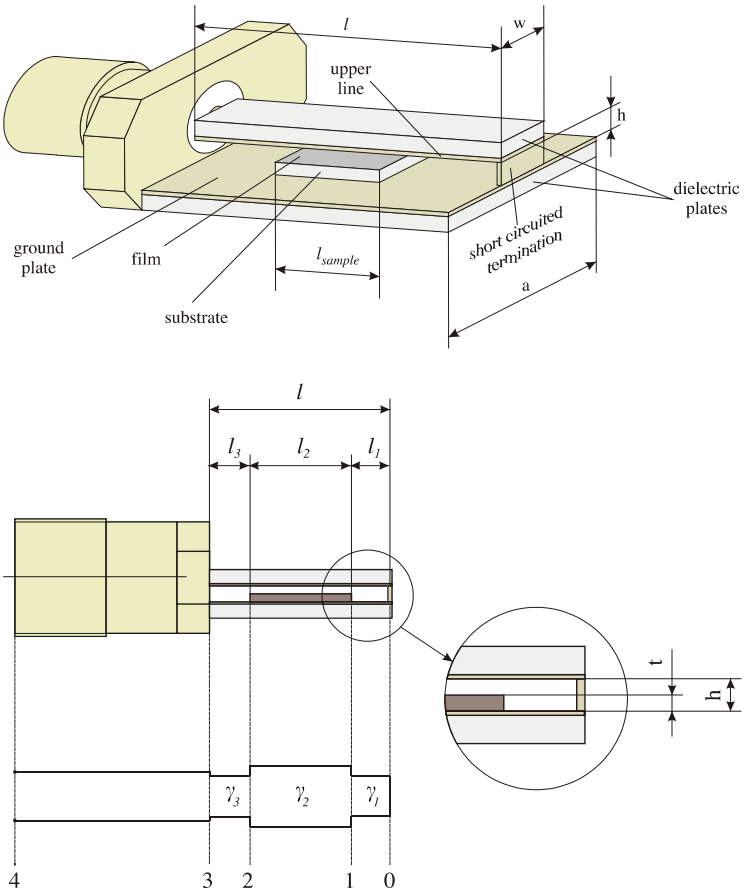


Figure 0.5 Schematic design of strip-line.

### 3.2.1 Theory

The expression for the reflection coefficient of a transmission line section is given by the basic equation[94]:

$$R = R_o e^{-2\gamma l} \qquad (3.4)$$

where γ is the propagation constant, $l$ is the length of a section and $R_o$ is the reflection coefficient of the strip line at the termination. The propagation constant is defined by the general solution of the Maxwell's equations [95] :

$$\gamma = \sqrt{-\omega^2(\varepsilon - \frac{i}{\rho\omega})} \qquad (3.5)$$

where ω=2πf is the angular frequency and ρ is the resistivity. μ, ε are the permeability and permittivity, respectively. According to a quasi-transverse electromagnetic wave approximation, the propagation constant of an inhomogeneous medium (air+substrate+material) can be represented by an effective homogenous expression:

$$\gamma = \frac{i\omega\sqrt{\varepsilon_{eff}\mu_{eff}}}{c_0} \qquad (3.6)$$

where $\varepsilon_{eff}$ is the effective permittivity, $\mu_{eff}$ is the effective permeability of the material and $c_0$ is the velocity of light in vacuum. Thus, it can be seen that that the effective permeability of a material directly influences the reflection coefficient of a shorted strip transmission line. For the strip-line shown in Figure 3.5, which exhibits two different sections i.e. air and sample, the common expression for the reflection coefficient is modified as follows[96]:

$$R = R_o e^{-2(\gamma_1 l_1 + \gamma_2 l_2)} \qquad (3.7)$$

where $\gamma_1$, $\gamma_2$ are the propagation constants of the sample and free-space regions respectively, $l_1$ is the sample length and $l_2$ is the common length of the empty strip line sections. Due to the shorted end of the strip line, $R_o$ is set to be –1.

### 3.2.2 Modeling methodology and extraction of frequency-dependent permeability

The SONNET EM simulation of the shorted strip-line outputs the scattering parameter S11 for different frequencies. The parameter S11 represents the reflection coefficient R of the strip line (R = ln (S11)). Using analytical equations[96], the frequency-dependent effective permeability of the composite structure can then be extracted from the simulated S11 plot. The analytical equations are solved using MATLAB. Figure 3.6 shows a schematic of the shorted strip line simulated using SONNET.

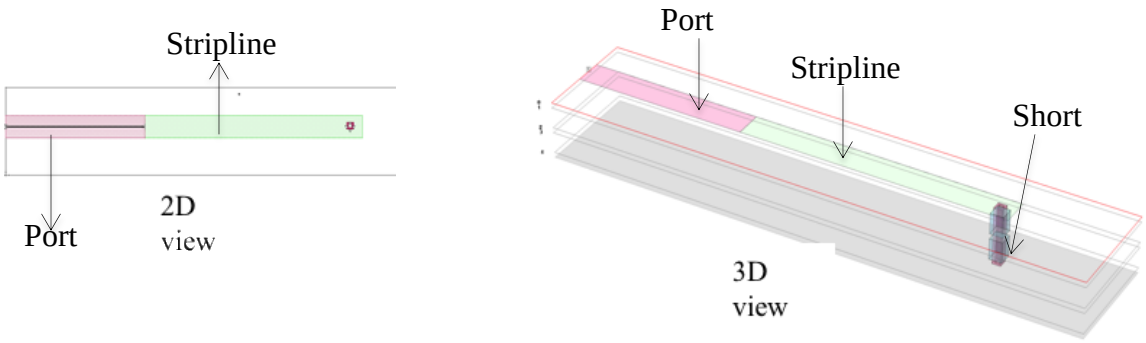


Figure 0.6 2D and 3D views of the simulated shorted strip transmission line structures.

The first step in the modeling procedure was to eliminate frequency-dependent errors associated with conducting losses and dielectric losses. This was attained by determining the effective permittivities of the empty strip line, $\varepsilon_{eff}^{empty}$, in the desired frequency range. $\varepsilon_{eff}^{empty}$ is extracted from the simulated reflection loss coefficients for an empty strip line, $S_{11}^{empty}$, by assuming $\mu_{eff}$=1.

$$\varepsilon_{eff}^{empty} = \left(\frac{ic_0 \ln(-S_{11}^{empty})}{2\omega(l_1+l_2)}\right)^2 \qquad (3.8)$$

The next step involves simulating a substrate (Si)-loaded strip-line without the magnetic

film. The effective permittivity of the substrate loaded strip-line region, $\varepsilon_{eff}^{sub}$, is obtained from the simulated reflection loss coefficients, $S_{11}^{sub}$, from:

$$\varepsilon_{eff}^{sub} = \left(\frac{ic_0 \ln(-S_{11}^{sub})}{2\omega l_2} - \frac{\sqrt{\varepsilon_{eff}^{empty}} l_1}{l_2}\right)^2 \qquad (3.9)$$

The effective permeability is 1 even for this calibration structure. The last step of the modeling procedure involves simulating a strip-line loaded with magnetic film and substrate. The magnetic film in this case is the multilayered composite structure consisting of 3 magnetic layers, shown in Figure 3.7.

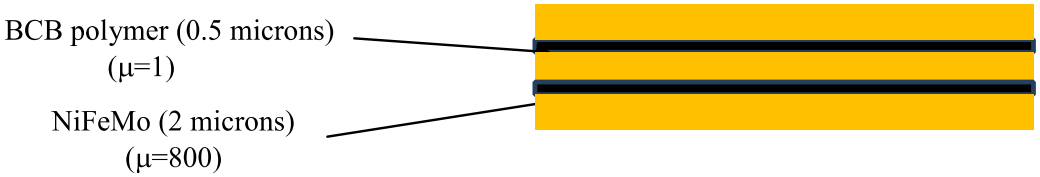


Figure 0.7 Simulated multilayered composite structure.

The effective complex permeability of the strip line is finally calculated from the simulated reflection coefficients of the strip-line loaded with both the magnetic film and substrate, $S_{11}^{f}$ , from:

$$\mu_{\text{eff}} = \left(\frac{ic_0 \ln\left(-S_{11}^{f}\right)}{2\omega l_2 \sqrt{\varepsilon_{eff}^{sub}}} - \frac{\sqrt{\varepsilon_{eff}^{empty}} l_1}{\sqrt{\varepsilon_{eff}^{sub}} l_2}\right)^2 \qquad (3.10)$$

The relative permeability, $\mu_r$ of the composite structure with thickness d was calculated from $\mu_{\text{eff}}$ by applying the relation:

$$\mu_r = \frac{\mu_{eff} - 1}{K_{(d/h)}} \qquad (3.11)$$

where h is the separation between the strip-line and the ground plane, and K is a proportionality factor determined by modeling the strip-line loaded with a sample of

known permeability (500).

## 3.3 EM modeling results

### 3.3.1 Effect of polymer thickness

The thickness of the magnetic layer was designed to be 2 μm based on analytical modeling shown previously. The EM modeling was performed to understand the effect of varying polymer layer thickness on the frequency-dependent permeability of the multilayered composite structures. Figure 3.8 shows the variation of permeability with frequency for different thicknesses of polymer layers. The magnetic layer is chosen to be NiFeMo for this simulation. The plot clearly shows that increasing the polymer thickness reduces the permeability of the NiFeMo multilayered composite films.

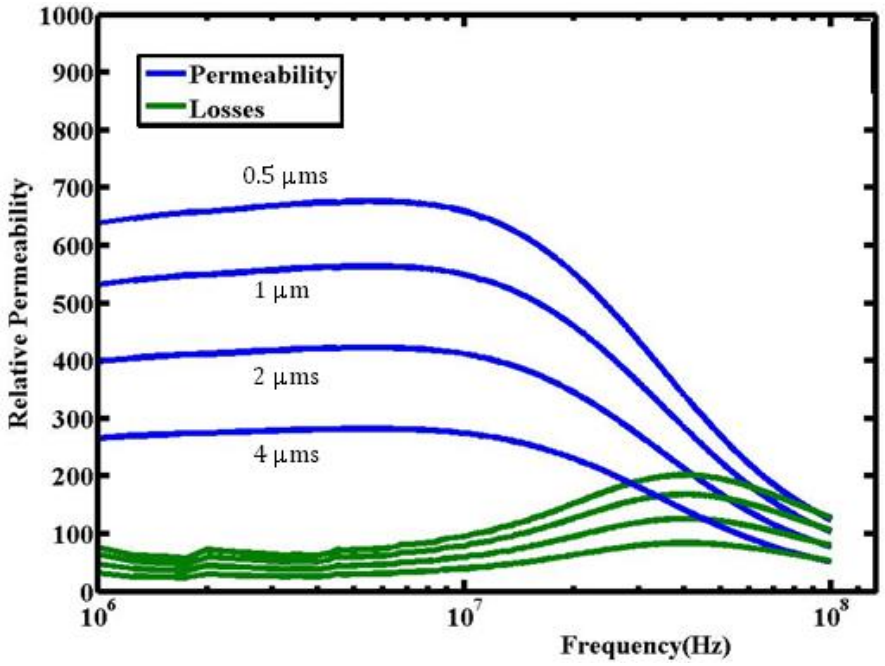


Figure 0.8 Variation of permeability for different thicknesses of polymer layers.

It can be seen from the plot that an ultra-thin polymer of thickness ~0.5 μm should be chosen to maintain a high permeability for the NiFeMo composite film.

### 3.3.2 Effect of magnetic layer resistivity

Figure 3.9 shows complex permeability spectra for different resistivities of the magnetic layers. This was performed by assigning the resistivities of NiFeMo (low resistivity=6e-5 ohm-cm) and CoZrO (high resistivity=30e-5 ohm-cm) for the individual magnetic layers in the SONNET simulation, although the permeability was kept constant. The magnetic layer thickness was chosen to be 2 microns and the polymer thickness was 0.5 microns. It can be clearly seen from the plot that increasing the magnetic layer resistivity by 5X increases the frequency stability of permeability also by ~4-5X.

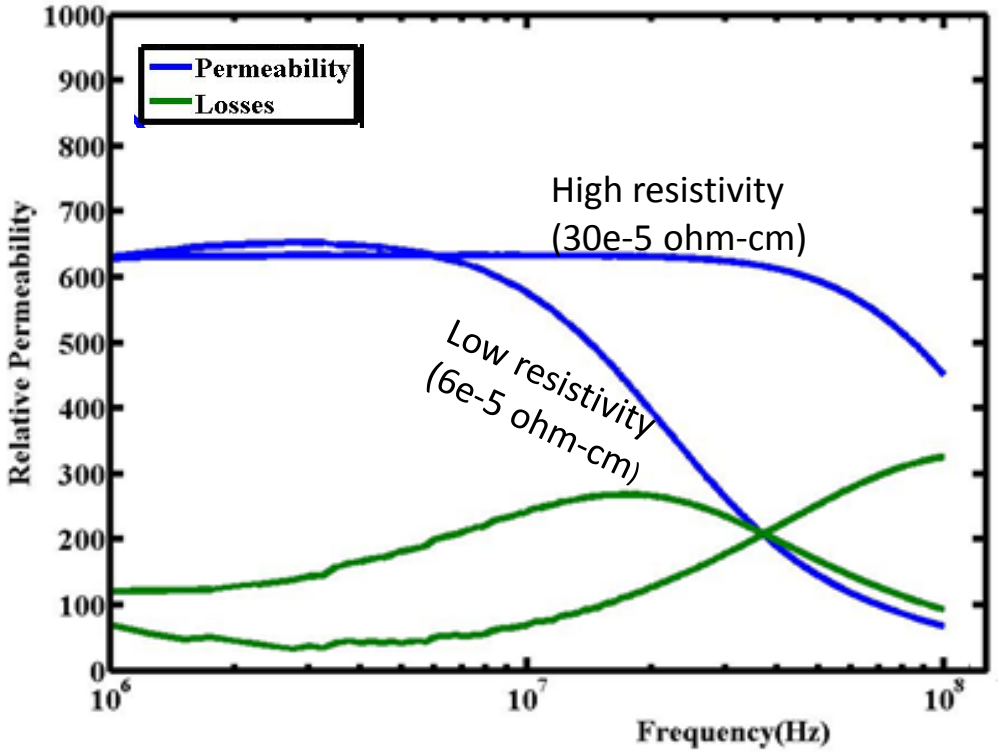


Figure 0.9 Variation of permeability for different resistivities of magnetic layers.

## 3.4 Summary

The guidelines for geometry and material parameters of the multilayered composite structures were determined based on the modeling results. The multilayered composite

structure is designed to consist of high μ magnetic layers (NiFe, NiFeMo, CoZrO) of thickness 2 microns and ultra-thin polymer layers of thickness 0.5 microns. The designed multilayered composite structures can achieve high μ (>500) and high $M_s$ (>0.5T) at desired frequencies of 1-10 MHz. Increasing the magnetic layer resistivity and decreasing its thickness will further enhance the frequency stability of permeability of the multilayered composite structure. Decreasing the thickness of the polymer layer will also enhance the permeability and $M_s$ of the multilayered composite structure. The fabrication and characterization of these composite structures will be described in Chapter 4, and their integration onto substrates as power inductors in Chapter 5.

# CHAPTER 4

# FABRICATION AND CHARACTERIZATION OF MULTILAYERED MAGNETIC COMPOSITE STRUCTURES

This chapter presents the fabrication and characterization of the multilayered composite structures that were modeled and designed in Chapter 3. The complete process details and structural characterization of the multilayered composite structures are described in the first part of the chapter. DC and high-frequency magnetic characterization of the composite structures are then described to validate the models developed in Chapter 3.

## 4.1 Material design

The multilayered composite structures are designed to achieve high μ (>500) and high $M_s$ (>0.5T) at desired frequencies of 1-10 MHz. The designs are based on the guidelines from modeling in Chapter 3, as shown in Figure 4.1. The multilayered composite structure design comprises of high μ metal layers (NiFe, NiFeMo, CoZrO) of thickness 2 microns and ultra-thin polymer layers of thickness 0.5 microns. The total target thickness of the multilayered composite structure is 50-100 microns.

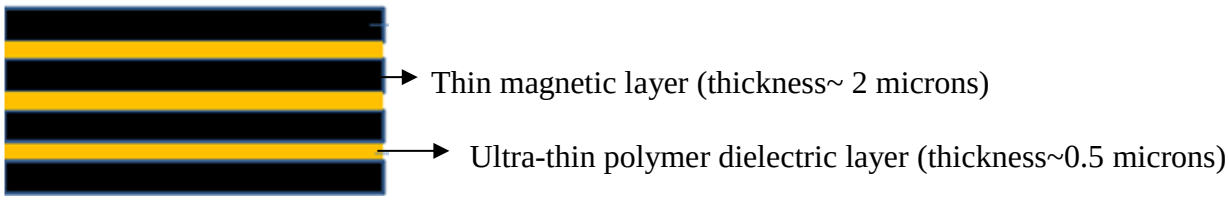


Figure 0.1 Design of multilayered composite structures.

Two approaches are pursued to fabricate the designed multilayered composite structures:

- Approach 1: Film transfer of sputtered magnetic films.
- Approach 2: Lamination of cold-rolled magnetic films.

## 4.2 Film-transfer of sputtered magnetic films

In the film-transfer process, magnetic thin films are deposited on temporary carriers. The carriers with the magnetic layers are then flipped and bonded to the device substrate using ultra-thin adhesive layers that also insulate the magnetic layers. The carrier is then released from the film. The magnetic film bonded well to the device substrate because of the high adhesion strength from the adhesive film. The film is thus transferred to the device substrate, and this process is repeated multiple times to form the multilayered composite structure. Figure 4.2 shows a schematic illustration of the process.

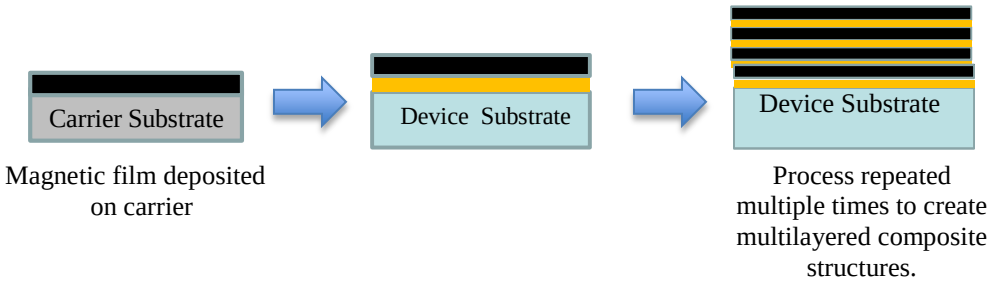


Figure 0.2 Schematic of film transfer process.

The first step in the film-transfer process is to develop magnetic thin film processes for high-permeability and high-$M_s$ magnetic films with low coercivity (<5Oe) and induced-anisotropy. This was achieved with two candidate materials: a)NiFe (b) CoZrO. Anisotropy is induced in the films using in-situ magnetic field during deposition, created by using a magnetic frame in the deposition chamber, as shown in Figure 4.3.

### 4.2.1 NiFe thin film process development

Permalloy ($Ni_{80}Fe_{20}$) is a widely explored high-permeability soft magnetic material used for various magnetic applications. Its behavior and properties are very well understood and hence it was chosen as a front-up magnetic

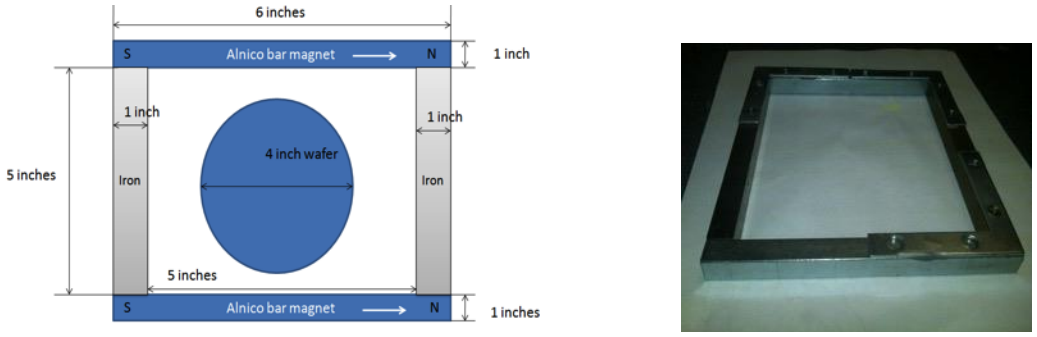


Figure 0.3 Magnetic frame used for creating in-situ magnetic field.

layer candidate for fabricating the multilayer core structures in power inductors. However, films with thicknesss above 200 nm show poor magnetic properties due to the stripe-domain effect. Hence, each layer of NiFe is further fabricated, as a multilayered stack, separated by $TiO_2$ interlayers (thickness~10 nm) to avoid this effect. Figure 4.4 shows the SEM image of such a multilayered stack. The thickness of the film is ~2 microns. The film-deposition was performed in DC sputterer (Denton Discovery) using a $Ni_{80}Fe_{20}$ alloy target in Ar atmosphere with a sputtering pressure of 6-7 mTorr and base pressure of 1E-7 torr. The deposited multilayered films have high permeability (~200), high saturation magnetization (~1T), low coercivity (~3Oe) and in-plane magnetic anisotropy, as shown by the B-H loop of Figure 4.5, measured using vibration sample magnetometry (VSM, Lakeshore 736 Model).

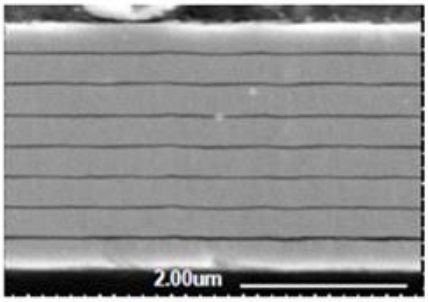


Figure 0.4 SEM image of the multilayered NiFe/$TiO_2$ stack.

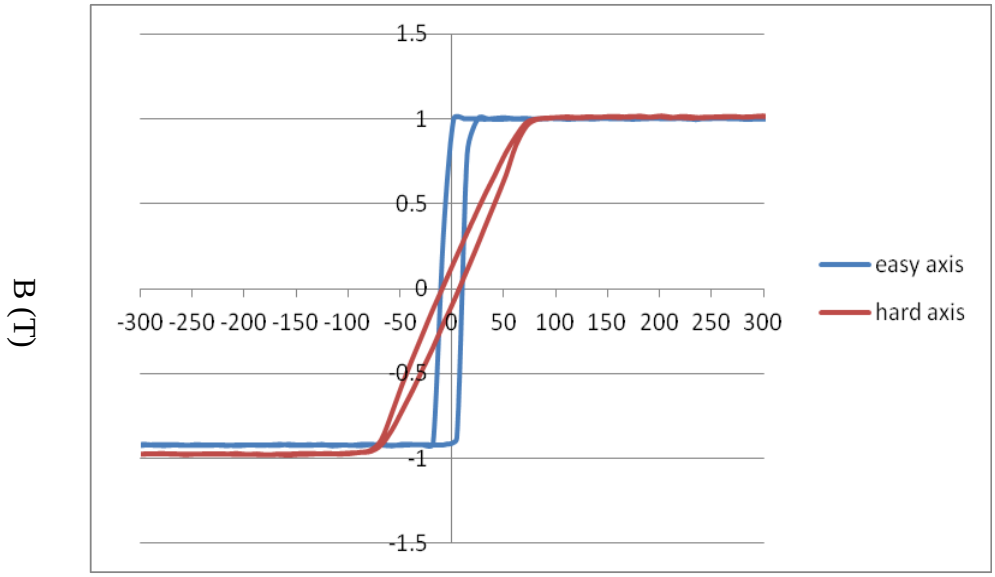


Figure 0.5 B-H loop of multilayered NiFe/$TiO_2$ stack showing good magnetic properties.

### 4.2.2 Nanostructured Co-Zr-O thin film development

Soft Co-based nanostructured films of the composition Co–M–O (*M*=nonmagnetic metal with high oxygen affinity) have high Ms, high μ and high electrical resistivity ρ, and are used as the second candidate. Co–M–O granular films are generally prepared using co-sputtering. Electrical resistivity and anisotropy field can be adjusted by controlling the ratio between cobalt and the nonmagnetic oxide. Decreasing the Co:oxide ratio usually increases the electrical resistivity. On the other hand, to keep high enough saturation magnetization *Ms*, a high fraction of cobalt is desired. It has also been reported that favorable soft magnetic properties can only be obtained in a limited composition range [ref]. Outside of this range, a strong perpendicular component of anisotropy often occurs, which can result in stripe domains, which increases coercivity and lowers the permeability.

The deposition of Co-Zr-O films is performed in a RF-DC sputterer by co-sputtering Co and Zr targets in an Ar+$O_2$ atmosphere on 4" Si wafers and glass substrates. The amount of oxygen in the sputtered films is precisely controlled by flowing oxygen from a premixed gas cylinder of Ar+5% $O_2$ and mixing it with pure Ar in a desired ratio during sputtering. Ar+5% $O_2$ and Ar are introduced simultaneously into the sputtering chamber using two different Mass Flow Controllers (MFCs) which help in controlling their ratios. Thus, by changing the ratio of power applied to Co and Zr targets, and Ar: Ar+5% $O_2$ gas-flow ratio, the composition of the film can be controlled during sputtering. The resistivities of the films are measured using a 4-point probe. The average resistivity of the sputtered films is about 3E-4 ohm-cm.

The composition of the films was measured using x-ray photoelectron spectroscopy (Thermo K-Alpha). The composition depth-profile was obtained by measuring the film composition at different depths, by sequentially sputter-etching the film. Figure 4.6 shows the composition profile of the sputtered films.

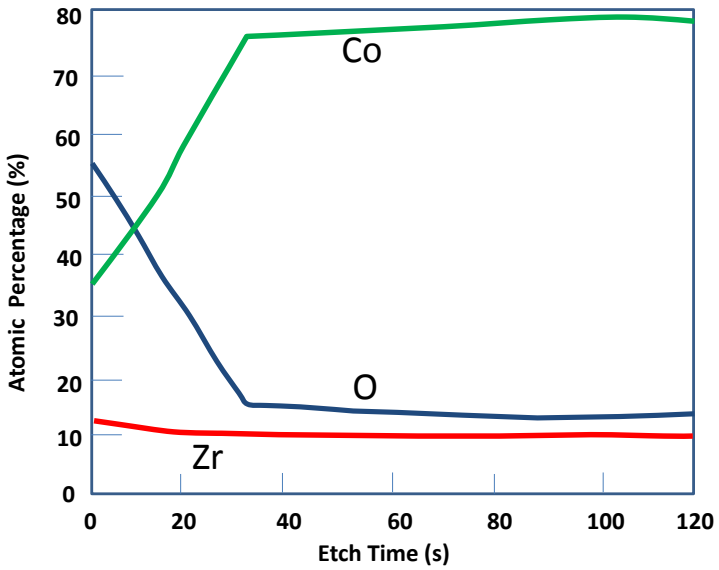


Figure 0.6 XPS composition profile of the sputtered films.

The XPS spectra confirmed that cobalt is predominantly in zero-valence state with minor oxide shoulders, while zirconium is in the oxidized state as shown in Figure 4.7. The SEM cross-section of the film is shown in Figure 4.8. TEM studies in the literature report that the cobalt forms a nanogranular structure of 1-2 nm interspersed with the oxide[97]. As described by the analysis of Herzer, the nanogranular domains interact through exchange coupling leading to enhanced permeability.

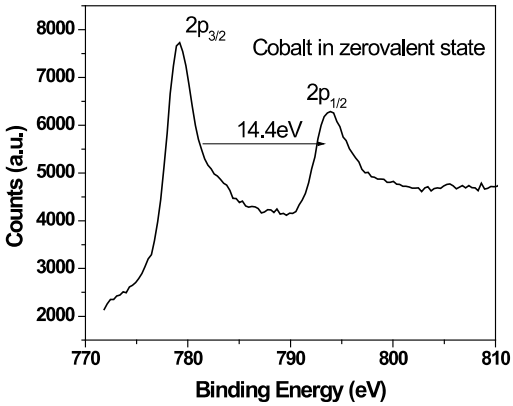


Figure 0.7 Cobalt 2p core level XPS spectrum.

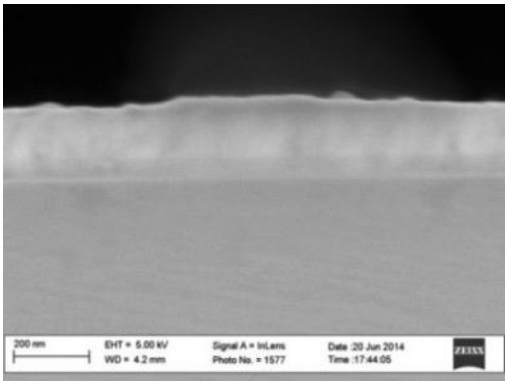

Figure 0.8 SEM cross-section of nanomagnetic Co-Zr-O films from co-sputtering.

Characterization: When a unidirectional magnetic field is applied during deposition, a corresponding magnetic anisotropy with low coercivity in the hard-axis direction is created in the films. To confirm this, the anisotropic magnetic properties of the films were measured using vibration sample magnetometry (Lakeshore 736 Model). The tool

identifies the easy and hard axis directions of the film and measures the properties along them. The deposited multilayered films have high permeability, high saturation magnetization, and in-plane magnetic anisotropy, as shown by the B-H loop in Figure 4.9. Good in-plane anisotropy with high field anisotropy of 50 Oe and low coercivity of 3.7 Oe were measured from the loop. The high resistivity and low coercivity are expected to result in low losses. The properties of the deposited films are compiled in Table 4.1.

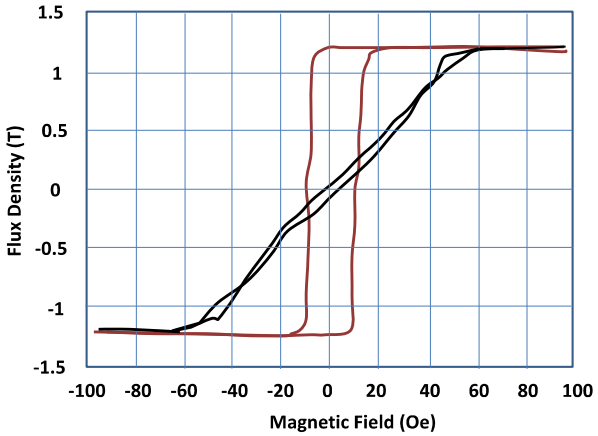


Figure 0.9 B-H loop of deposited Co-Zr-O films.

Table 0.1 Properties of Co-Zr-O films.

| | |
|---|---|
| Relative Permeability | 200 |
| Thickness | 150-200 nm |
| Coercivity | 3.7 Oe |
| Anisotropy field | 40-50 Oe |
| Saturation magnetization | 1.2 Tesla |
| Resistivity | 300 micro-ohm-cm |

### 4.2.3 Film-transfer process conditions and results

Choice of adhesive material**:** The polymer dielectric adhesive layer should be such that it can be very easily thinned down to required thickness (~0.5 microns). Yet, it should still have sufficient adhesion strength to be able to transfer the magnetic film from the carrier

wafer to the device wafer. For these purposes, spin-on BCB polymer (Cyclotene 3022-46) was chosen as the adhesive layer as it can be easily diluted to coat submicron level thicknesses, but still have enough adhesion strength to enable film-transfer. The adhesion strength was measured by bonding 25 micron Ni foils using 0.5 microns of spin-coated BCB and conducting a peel test on them. Figure 4.10 shows the adhesion strength of 0.5 microns BCB measured by peel-testing, which confirms its excellent bonding properties. The adhesion strength is approximately 150 gms/cm.

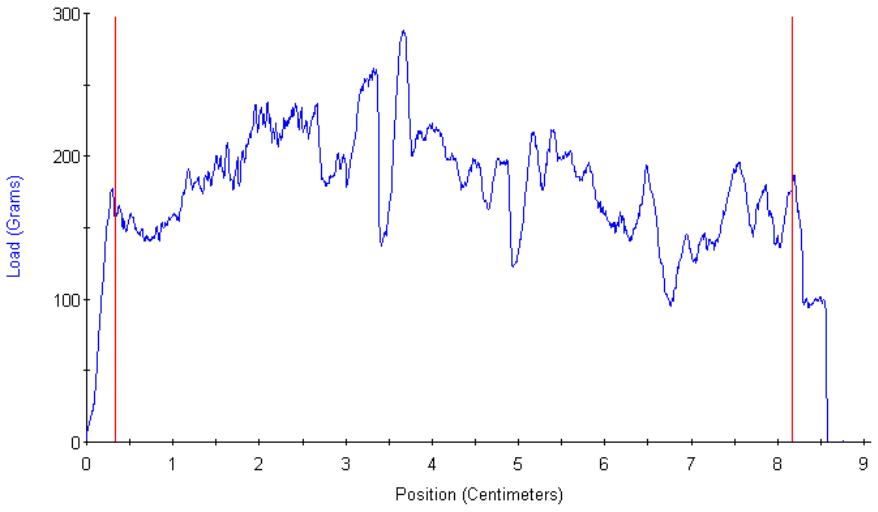


Figure 0.10 Peel test for BCB-coated Ni-foils

To transfer film , the carrier substrate (6-inch oxidized silicon wafer) is deposited with 1 micron thick layer of magnetic NiFe film (monolithic layer). It is then rinsed with DI water, and spin-coated with a coupling agent (AP3000) to promote adhesion. This completes the carrier wafer preparation. On a separate device wafer, the same coupling agent (AP-3000) was spin-coated onto the wafer to promote adhesion. Diluted BCB is spin-coated onto the device wafer. The dilution of the polymer and spin-coating speed are maintained such that the final thickness of BCB on the device wafer is 0.5 microns. This completes the device wafer preparation.

The carrier and device wafers are bonded in a hot press. The wafer pair is heated upto 300 C for 1 hour in the hot press using a small piston force of 1 kN. The wafer pair is allowed to cool down and the piston force is released. Thereafter, the bonded wafers are manually debonded by using a razor blade insertion and subsequent separation, thus transferring the film from carrier to the device wafer. Figure 4.11 shows the optical images of the carrier wafer (6-inch) and device wafer (6-inch) after the film-transfer process, using an ultrathin BCB layer of 0.5 microns. From the Figure, it can be seen that NiFe film is transferred completely from the carrier wafer to device wafer. Thus, the feasibility of the film transfer approach is proven over a large substrate area. This process is repeated multiple times to get a multilayered structure. Figure 4.12 shows a SEM cross-section of a 2-layer transferred NiFe/$TiO_2$ film. Figure 4.13 shows the DC magnetic properties of the multilayered NiFe/ $TiO_2$ film obtained after film-transfer, measured using VSM. The coercivity increased from 3 Oe to about 6-7 Oe after film-transfer, indicating some loss in magnetic anisotropy and hard-axis properties. Film-transfer involves heat-treatment at 250 C to cure the adhesive, which could degrade the magnetic anisotropy. Film-transfer also changes the stress-state in the film while releasing from the carrier and transferring to the substrate. All these phenomena have an impact on the coercivity. However, the multilayered composite structure still retains high Ms and high $\mu$.

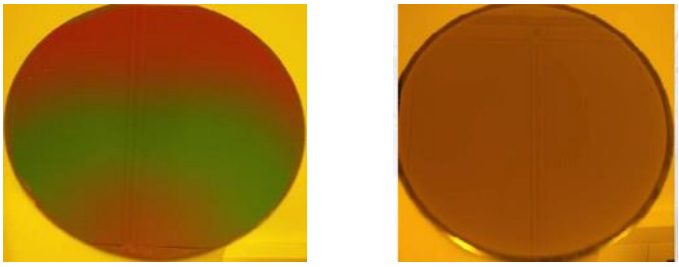

Carrier wafer after transfer  Device wafer after transfer

Figure 0.11 Optical images of carrier and device substrates after film-transfer.

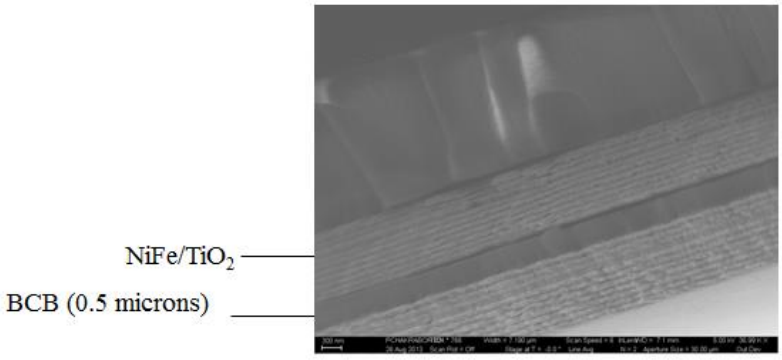


Figure 0.12 SEM cross-section of a transferred 2-layer NiFe/$TiO_2$ film.

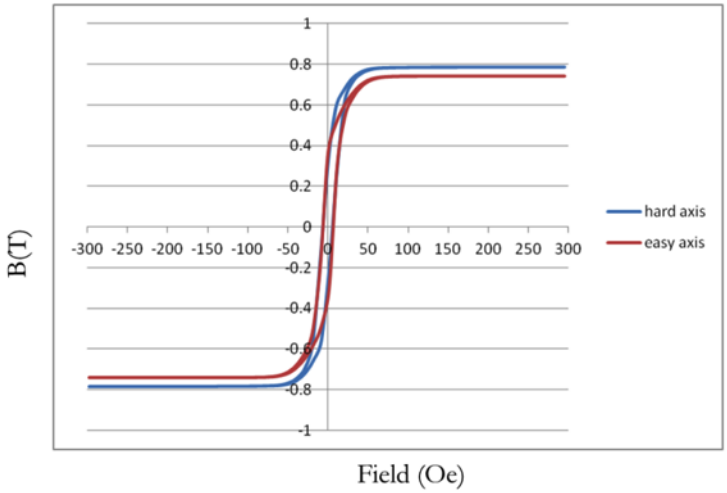


Figure 0.13 B-H loop of the multilayered NiFe/ $TiO_2$ after film-transfer.

### 4.3 Lamination of cold rolled magnetic foils

In this approach, cold-rolled magnetic foils of ~2 microns thickness are laminated using ultra-thin polymer adhesives of ~0.5 microns thickness to form the multilayered composite structures. Cold-rolled magnetic foils of molypermalloy (NiFeMo) that are two-microns thick, are commercially obtained for this purpose.

To form multilayer structures, spin-on BCB polymer (Cyclotene 3022-46) was again chosen as the ultra-thin polymer adhesive layer. The magnetic foils are temporarily laminated onto Si wafers to ensure ease of spin-coating. Multiple foils are individually spin-coated with a coupling agent AP3000 to promote adhesion. Diluted BCB is then individually spin-coated on these foils. The dilution of the polymer and spin-coating speed are designed such that the final thickness of BCB is 0.5 microns. The BCB-coated foils are then stacked together in a vacuum laminator and initial low-temperature bonding is performed at 100c for 60s to ensure wrinkle-free lamination. Finally, the multilayered foil stack is cured in a hot press at 300C for 1 hour. Figure 4.14 shows the image of a free-standing 16-layered foil of thickness ~50 microns. Figure 4.15 shows the SEM cross-section of a multilayered composite formed by foil-lamination, showing ultra-thin BCB layers.

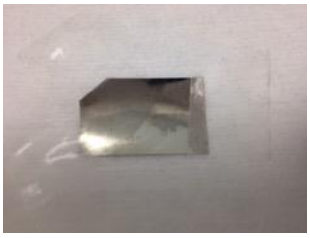

Figure 0.14 Free-standing multilayered laminates.

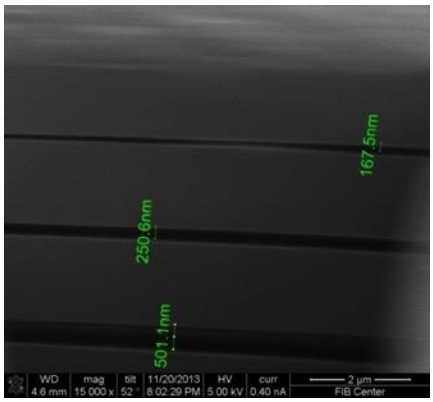


Figure 0.15 SEM cross-section of the multilayered composite structure.

Figure 4.16 shows the B-H loop of a 4-layered foil laminate of thickness ~10 microns, compared with a single layer of 2 microns. It should be noted that there is no hard and easy axis of magnetization as no magnetic field is applied during the fabrication of the structure to induce magnetic anisotropy. The multilayered composite structures formed by foil lamination have a high Ms, high μ and low coercivity (~4.4 Oe). The single foil layer sample has an Ms of 0.8T while the 4-layered foil laminate has an Ms of 0.6T. This is due to the dilution effect of the polymer layers, which is proportional to their volume fraction, as shown in Equation 3.2. The coercivities of both the samples are 4.4 Oe, which shows that the presence of intermediate polymer layers has an insignificant effect on the coercivity of the magnetic layers.

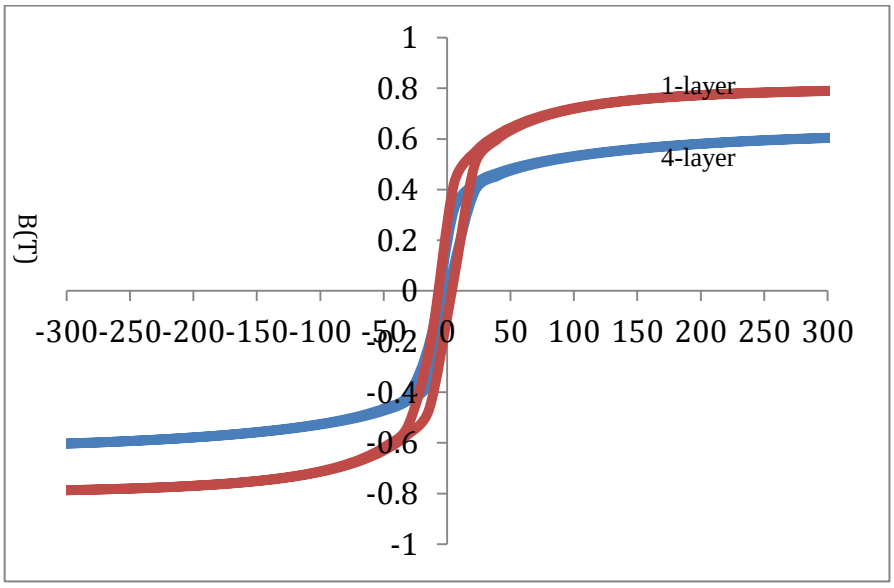


Figure 0.16 B-H loop of multilayered foil laminate

### 4.4 High-Frequency Magnetic Characterization

This section describes the high-frequency magnetic characterization technique to measure the frequency-dependent permeability of multilayered composite structures. An easy and

precise method for the measurement of the frequency-dependent complex permeability of magnetic materials, especially thin-films, is critical for the development of new magnetic materials. The measurement of frequency-dependent complex permeability can be performed using two types of methods: coil based techniques and transmission line methods. Coil techniques use an external electromagnetic field produced by means of a drive coil. The permeability is extracted from the impedance measurements of a pick-up coil with a sample under test [98]. The coil techniques provide reliable and accurate measurements in the MHz frequency range but their sensitivity decreases at GHz frequencies due to dimensional resonance and sensitivity effects. Transmission line techniques, on the other hand, use transmission and reflection (two-port measurement) or only reflection (one-port measurement) coefficients of a strip[99] or coaxial transmission line[100] loaded with a magnetic material. The one-port measurement technique has the simplest sample preparation and calibration procedure. It measures frequency-dependent permeability based on the modeling of network impedance of a strip-line, especially its reflection coefficients. The analytical models for extracting the frequency-dependent permeability from the reflection coefficients of a transmission line section in the one-port measurement technique have already been explained earlier in Chapter 3.

The frequency-dependent effective permeability of the composite structure is estimated from the measured S11 parameters over a frequency range for a shorted-strip transmission line, as described in Bekker et.al[96]. The measured S11 parameters represent the reflection coefficient of the strip line (R=ln(S11)). The permeability measurements were performed in three steps, the first one with an empty strip line, and the second one with the strip-line loaded with kapton tape as the substrate. The third measurement was made with the strip-line loaded with the multilayered composite film laminated onto the substrate kapton tape. This procedure eliminates frequency-dependent errors associated with conducting and dielectric losses, as well as strip-line fabrication

and connection mismatches. The effect of substrate and sample permittivity on reflection losses is also taken into account.

Figure 4.17 shows the shorted strip transmission line setup with the multilayered composite foil laminate. The shorted strip line is connected to a network analyzer to measure the S11 parameters. The shorted strip line structure with magnetic film underneath it is shown in Figure 4.18.

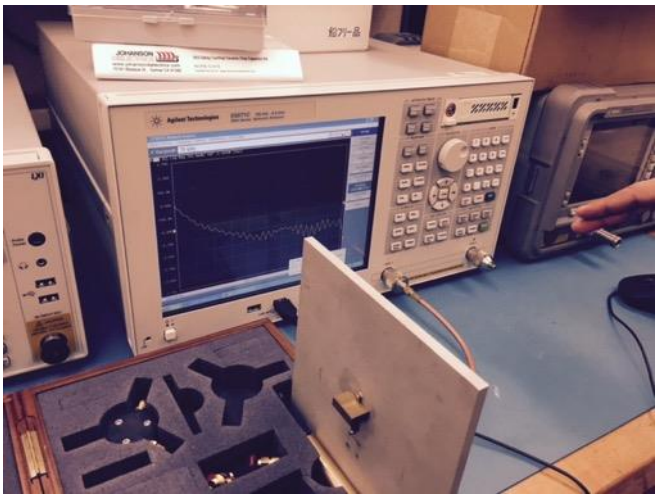

Figure 0.17 Setup for measuring high-frequency magnetic properties.

Figure 0.18 Shorted strip-line structure with magnetic film.

Measurement results and model validation: The complex permeability spectra of a 4-layered composite structure (thickness~10 microns) fabricated using foil lamination and measured using the shorted strip-line structure is shown in Figure xx. It can be seen that

the foil laminate has a stable high permeability (~500) till 10 MHz. Thus, they can be used as thick magnetic cores (50-100 microns) for power inductor applications in the frequency range of 1-10 MHz. Figure 4.19 shows the plot of effective permeability vs frequency of a 2-layered NiFe/$TiO_2$ stack fabricated using film-transfer. These films have stable high permeability (~900) at frequencies of above 100 MHz. Figure 4.20 shows that the measured real permeability of the foil laminates matches well with the results obtained using the EM modeling approach described in Chapter 3. However, the models and measurements for imaginary permeability need further refinement for accurate model-hardware correlations.

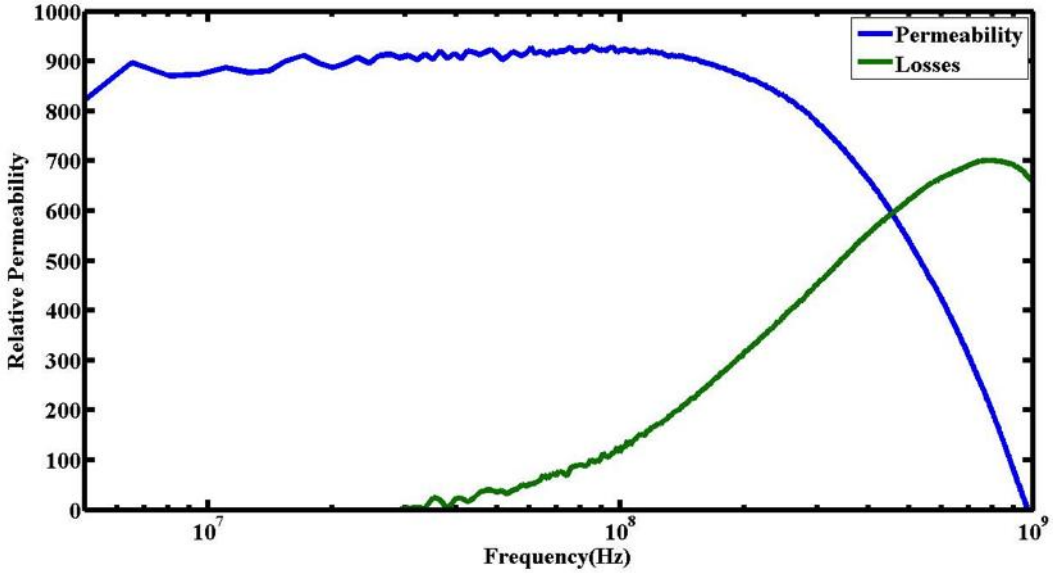


Figure 0.19 Variation of permeability with frequency for NiFe/$TiO_2$ stack.

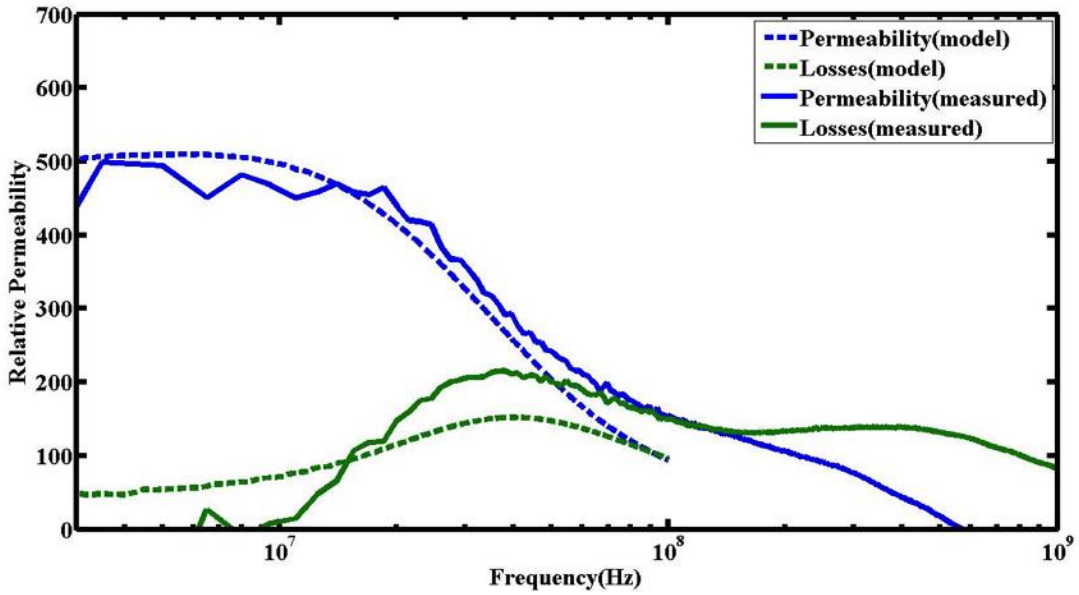


Figure 0.20 Measured and modeled permeability spectra for foil laminates.

Discussion: The frequency-dependence of permeability is governed by two major mechanisms: eddy current damping and Landau-Lifshitz-(L-L) phenomenological damping due to ferromagnetic resonance (FMR). In the multilayered composite structures, each magnetic layer can be considered as an independent magnetic thin-film which is not magneto-statically coupled to the adjacent magnetic layers because they are separated by an intermediate insulating polymer-dielectric. Thus, eddy current damping and FMR behavior of the individual layers also represent that of the composites.

L-L damping is determined by the intrinsic magnetic properties of the material. The precessional motion of magnetization can be described by the Landau-Lifshitz-Gilbert (LLG) phenomenological equation. The FMR frequency for a magnetic thin-film derived from the LLG equation can be written as[96]:

$$F_{fmr} = \frac{\gamma}{2\pi}\sqrt{(M_s + H_k)H_k} \qquad (4.1)$$

where $H_k$ is the anisotropy field, $M_s$ is the saturation magnetization and $\gamma$ is the gyromagnetic ratio.

In thicker films, eddy current effects dominate at frequencies lower than those at which L-L damping effects are observed. From Equation 3.1 and 3.2, it can be seen that the thickness and resistivity of magnetic thin-films are major factors in determining the frequency-dependent permeability, especially due to eddy current damping. Jayasekara et al. measured the permeability of NiFe single layer films of thicknesses ranging from 54 nm to 2.2 μm[93]. Thin NiFe samples (54nm-120nm) showed a behavior that could be fit with the L-L model. The permeability of thicker NiFe samples (2.2μm) was in agreement with the eddy current model. Similarly, for the multilayered composite structures consisting of NiFeMo films of 2 microns thickness, it can be shown that the permeability roll-off with frequency occurs due to eddy current damping as it occurs at much lower frequencies compared to the FMR frequency for NiFeMo. The FMR frequency for anisotropic NiFeMo thin-film is computed as 1.2GHz from Equation 6, while that of the isotropic film is ~30 MHz. The multilayered composite structure has a permeability roll-off with frequency at 10 MHz, indicating that the permeability relaxation is from eddy current damping and not FMR.

For the multilayered NiFe/$TiO_2$ stack fabricated by film transfer, eddy current losses are insignificant because the thickness of each individual NiFe film is only 200 nm. Hence, it has stable high permeability even beyond 100 MHz. Such films can be used for power inductors designed to work at 100 MHz.

## 4.5 Summary

Based on the design inputs from modeling in Chapter 3, multilayered composite

structures were fabricated using two approaches: film transfer and foil layering. The complete fabrication process details and the structural characterization of the multilayered composite structure are described. A novel technique for high-frequency magnetic characterization of the multilayered composite structures is also presented. The structures fabricated using foil lamination showed high $M_s$ (>0.5T) and high $\mu$ (~500) upto 10 MHz. The measured permeability of the multilayered composite structure matches well with the modeling results, thus validating the modeling approach. These results show that multilayered ferromagnetic-polymer composite structures can be used as thick magnetic cores (50-100 microns) for power inductor applications in the frequency range of 1-10 MHz. Chapter 5 focuses on integrating these materials onto substrates for thinfilm or planar power inductors.

# CHAPTER 5

# DESIGN, FABRICATION AND CHARACTERIZATION OF INTEGRATED INDUCTORS

This chapter describes inductor design, fabrication and characterization with the multilayered magnetic composite structures. . The first part of this chapter presents the design and fabrication of Si-integrated toroid inductors using the multilayered composite structures described in Chapter 2 and 3 as the inductor core. The process of micro-patterning the composite structure and forming 3D coils around them to demonstrate ultra-thin inductors is described in detail. The electrical characterization of the fabricated inductors is shown next to demonstrate the benefits of the novel magnetic structures for higher inductance densities.

## 5.1 Objectives

The specific objectives for this task are to show design and demonstrate integrated high-density inductors on silicon that can potentially achieve an inductance density of 2000 $nH/mm^2$, current-handling of 1 $A/mm^2$ for 100 micron component thickness. The specific objectives are also compiled in Table 5.1.

Table 0.1 Specific objectives of the proposed research

| **Parameter** | Objectives | Enabling technology |
|---|---|---|
| **Inductance density ($nH/mm^2$)** | 2000 | High-permeability and high-Ms magnetic composite films as magnetic cores; Integration with toroid designs; |
| **Power handling ($A/mm^2$) for 100** μm | 1 | |
| **Ultra-thin inductor** | 100 μms | |

## 5.2 Inductor Design

The primary objective of this research task is to design and demonstrate high-density inductors in silicon substrates with multilayered ferromagnetic-polymer composites. Toroid-based inductors designs are used because they enable highest power densities. The designs are shown in Figure 5.1. The inductor in this design consists of 16 turns of copper coil (red and green color), which surround the magnetic composite core (white color). The width of each turn of the coil is 50 μm. The gap between two consecutive turns is 100 μm. The length, width and thickness of the magnetic core (rectangular bar) are 7000 μm, 4000 μm and 1500μm, respectively. Each inductor structure has two pads for probing and measurement. The inductor layout on a 4-inch wafer is shown in Figure 5.3. Each wafer layout consists of 25 inductors.

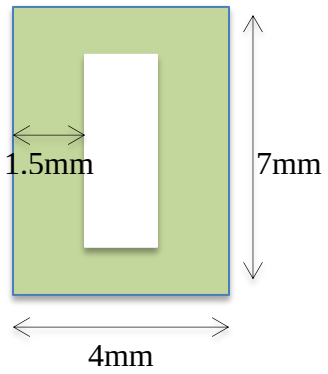


Figure 0.1 Schematic of toroid structure

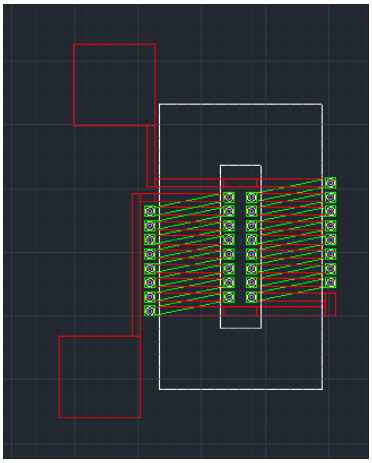

Figure 0.2 Design of single inductor coupon

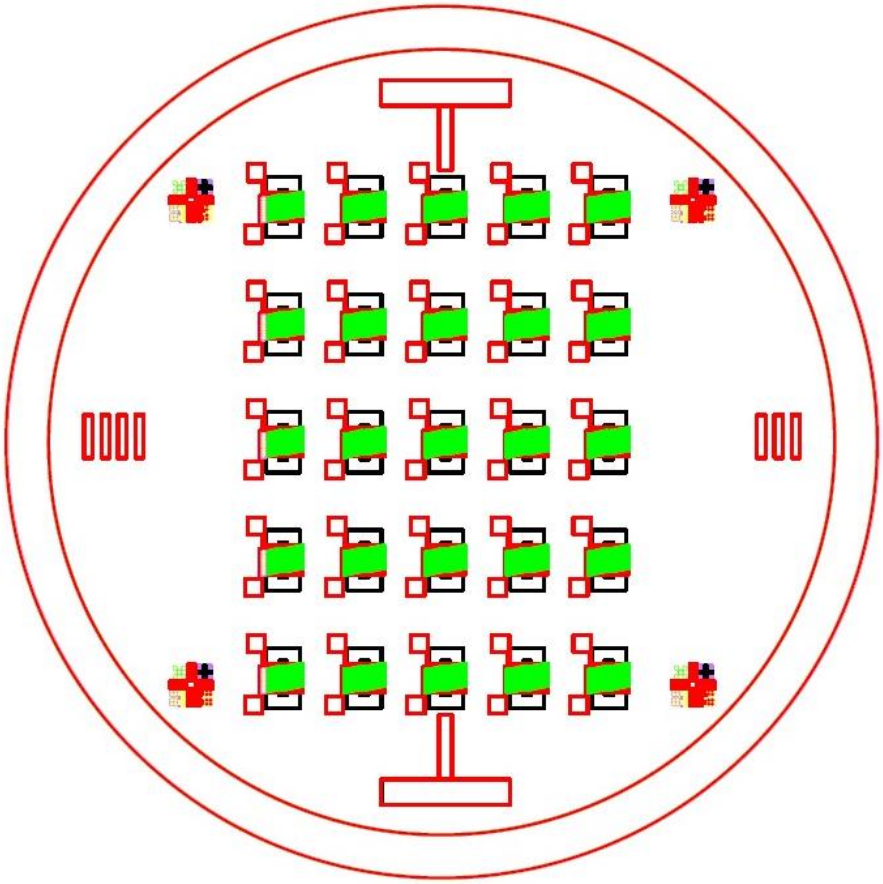

Figure 0.3 4-inch wafer inductor layout

## 5.3 Patterning of multilayered composite structures

Patterning the multilayered composites to form the toroid shape is the most critical step in forming the inductor devices. Various options have been explored to pattern the composite core, which are described in the following sections.

### 5.3.1 Micro-abrasive machining

In this process, the target material is eroded by use of fine abrasive particles blasted at a high velocity. This process allows for precise and accurate control of material removal rate. Non-machined areas are covered using a protective mask created by a photolithography step. The material removal mechanism is based on propagation and intersection of cracks generated by the impact of abrasive particles on the brittle materials**.** Figure 5.4 shows a schematic of the microabrasive machining process.

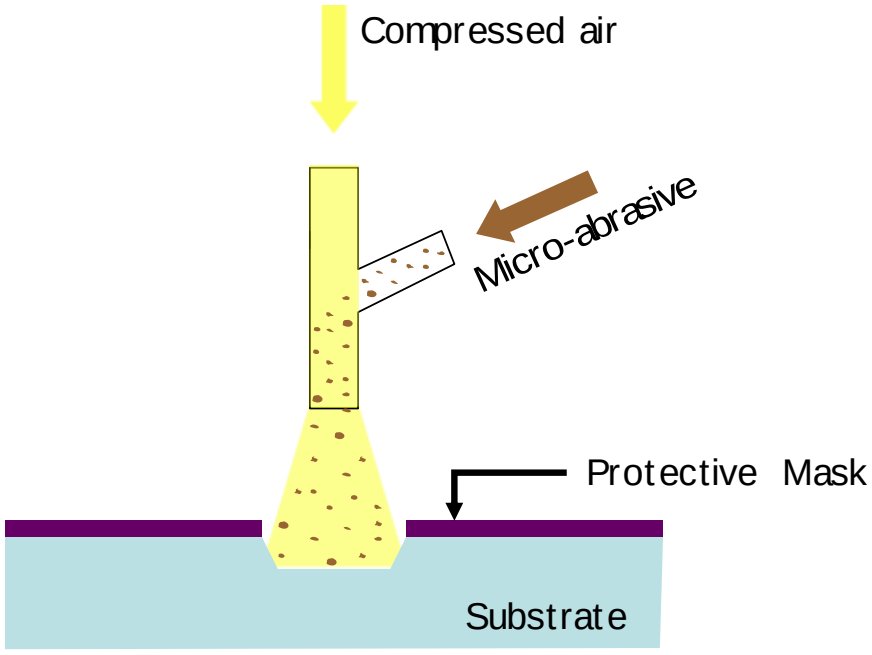


Figure 0.4 Schematic of abrasive machining process

Micro-abrasive machining trials were conducted using an in-house sandblasting tool as shown in Figure 5.5. Glass beads of size 45-90 microns were used as the abrasive media. Figure 5.6 shows a multilayered foil laminate covered with a patterned protective photomask (SR 3000). Figure xx shows a multilayered foil laminate bonded to a Si wafer, patterned with in-house micro-abrasive patterning.


Figure 0.5 In-house sandblasting tool

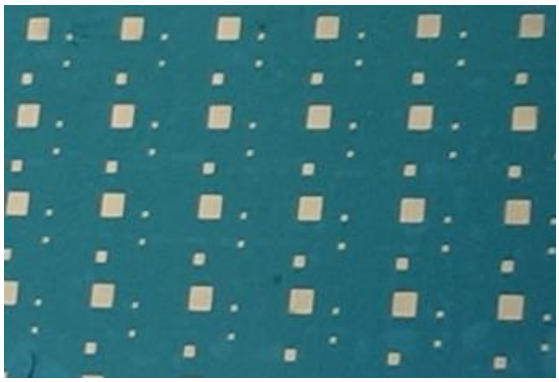

Figure 0.6 Patterned SR300 photoresist laminated on multilayered foils.

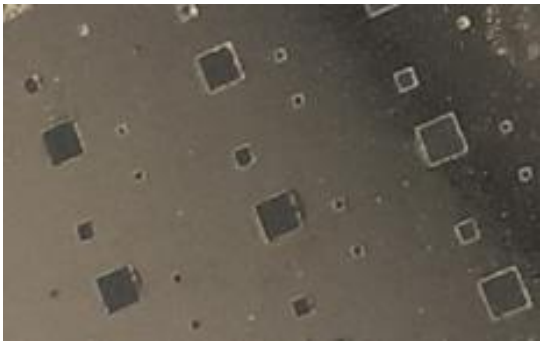

Figure 0.7 Pattern formed on foil laminate by in-house micro-abrasive machining

Figure 5.8 shows that the coarser features of the pattern (2mm x 2mm) have good edge resolution whereas the finer features (1mm x 1mm and 0.5mm x 0.5 mm) have conspicuous edge roughness and damage.

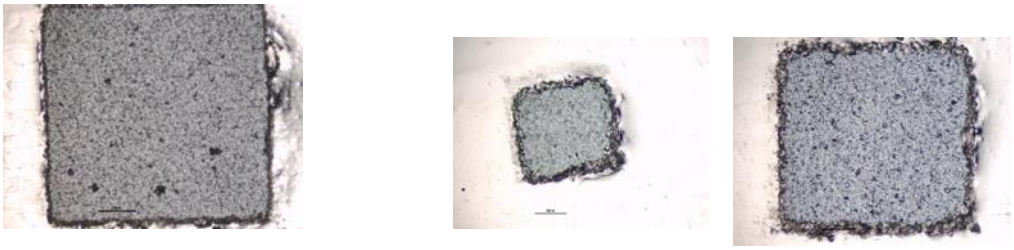

(a) 2mm X 2mm (b) 0.5mm X 0.5mm 1mm X 1mm

Figure 0.8 (a) Coarse features by in-house micro-abrasive patterning showing good edge resolution;(b)Fine features showing edge damage

Figure 5.9 shows SEM analysis of the edges of patterns formed by in-house micro-abrasive machining. The SEM images show significant roughness and smearing of edges.

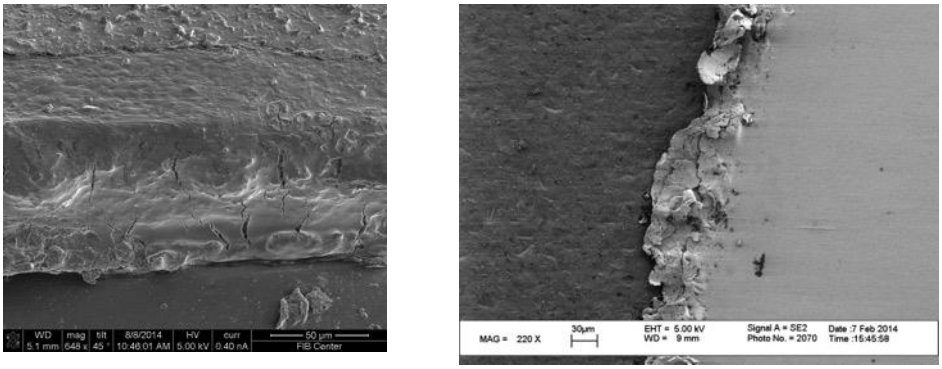

Figure 0.9 SEM images of pattern edges formed by in-house micro-abrasive machining

Finer features with good resolution are obtained by use of more precision-controlled equipment for micro-abrasive machining. This was performed with the help of an external vendor, Bullen Tech. Multilayered foils (~4 layers) of 10 micron thickness were bonded to Si wafers and sent to Bullen Tech for microabrasive patterning. Boron carbide particles of size 25-30 microns were used as the abrasive media for machining. Figure

5.10 shows the microscopic image of a 500 micron sized via feature formed by micro-abrasive machining at Bullen Tech., indicating improved edge resolution.

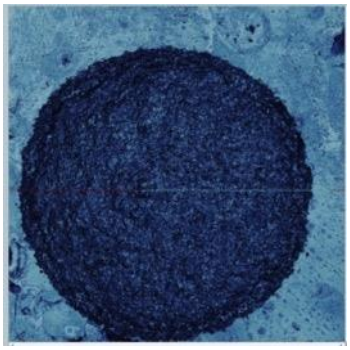

Figure 0.10 Microscopic image of 500 μm via feature formed by micro-abrasive machining

However, the SEM analysis of via edges revealed significant edge damage and smearing effects as shown in Figure xx. Thus further process optimization and post-pattern polishing or deburring operations are required to get minimal edge roughness and smearing.

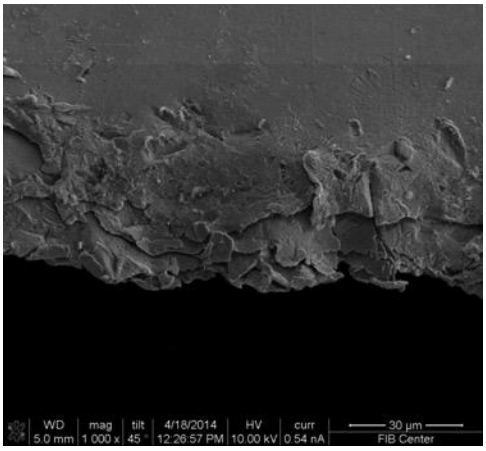


Figure 0.11 SEM images of via edges formed from micro-abrasive machining at Bullen Tech.

### 5.3.2 Ultrasonic machining

Ultrasonic machining is loose abrasive machining process in which the mirror image of a shaped tool can be created in materials. Material removal is achieved by the direct and indirect hammering of abrasive particles against a workpiece by means of an ultrasonically vibrating tool. It results in a low material removal rate compared to microabrasive machining. The process integrates well with semiconductor and MEMS processes. Machined features can be aligned to previously patterned, machined, or etched substrates.

Ultrasonic machining trials were conducted by sending samples to an external vendor, Bullen Tech. Multilayered foils (~4 layers) of 10 micron thickness were bonded to Si wafers and sent for processing. Boron carbide particles of size 25-30 microns were used as the abrasive media for machining. Figure 5.12 shows the microscopic image of a 500 micron sized via feature formed by micro-abrasive machining at Bullen Tech., showing good edge resolution.

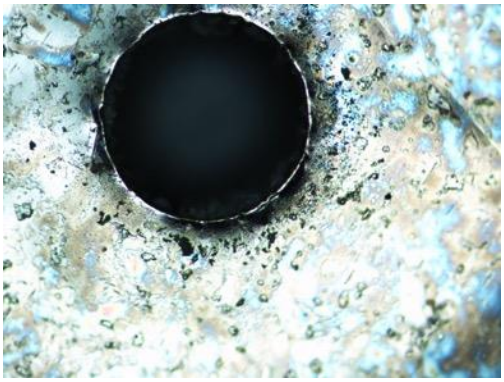

Figure 0.12 Microscopic image of 500 μm via feature formed by Ultrasonic machining

SEM analysis of via edges shown in Figure 5.13 demonstrates significantly lesser edge roughness and smearing compared to micro-abrasive machining. Some layer separation is also seen. However, some edge roughness still persists and many areas show no distinct

separation between layers. Thus further process optimization and post-pattern polishing or deburring operations are required to get minimal edge roughness and smearing.

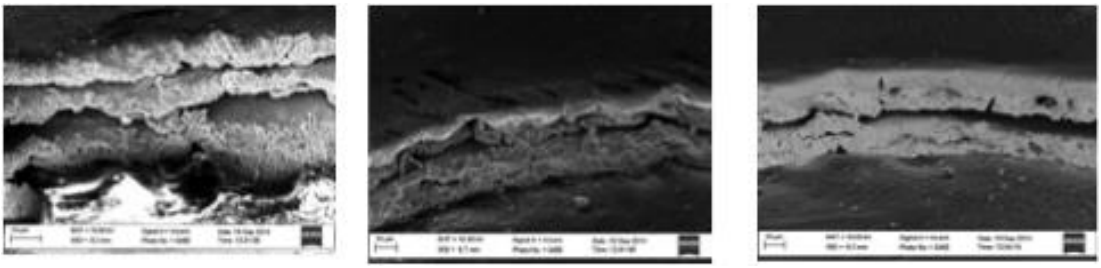

Figure 0.13 SEM images of via edges formed by Ultrasonic machining

### 5.3.3 Sequential etching

Toroid patterns can also be formed with the multilayered composite structures by masking it with a photoresist pattern created by a lithography step, and then sequentially etching the metal and polymer layers alternately. The photoresist is finally stripped off from the patterned structure. Nickel etchant Type-I obtained from Transene Chemicals is used to etch the NiFeMo metal layers. The ultra-thin BCB (0.5 microns thick) polymer dielectric layers are etched using a plasma based reactive ion etching (RIE) process in a Plasma-Therm RIE. Table 5.2 shows the plasma conditions for etching the BCB layers

Table 0.2 Plasma based RIE conditions for etching BCB layers

| | |
|---|---|
| **Power** | 300W |
| **Gas ratio** | $O_2$:$SF_6$=5:1 |
| **Gas Pressure** | 100 mTorr |
| **Time** | 10 minutes |

Figure 5.14 shows the image of a pattern formed by sequential etching on a 10 micron multilayered composite structure showing good edge resolution.

Figure 0.14 Pattern formed by sequential etching with multilayered composite structures.

Figure 5.15 shows SEM images of the patterned edges formed by sequential etching. The SEM images show complete separation of the metal layers and no edge smearing. Minimal edge roughness is seen due to metal undercut, which can be further reduced by using a dilute metal etchant. Thus, sequential etching method is adopted for patterning toroid features with the multilayered composite structures for the fabrication of integrated inductor test wafers.

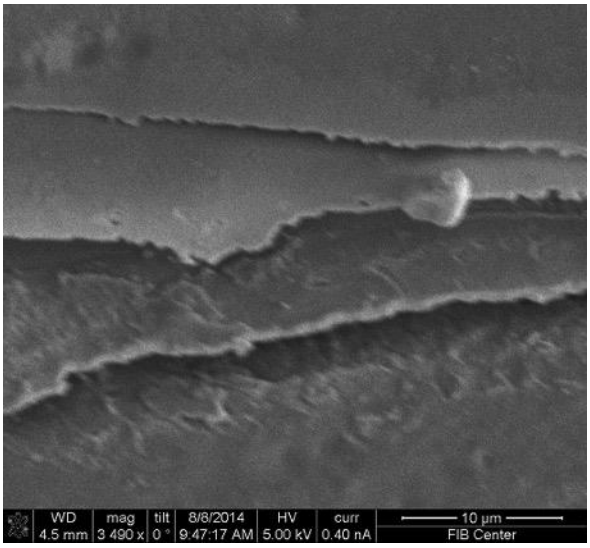


Figure 0.15 SEM images of pattern edges formed by sequential etching

## 5.4 Inductor test-vehicle fabrication

The fabrication of the designed integrated inductors with multilayered composite core requires formation of coils around a patterned toroid structure Figure 5.16 shows a schematic of the individual toroid inductor to be fabricated on Si wafer.

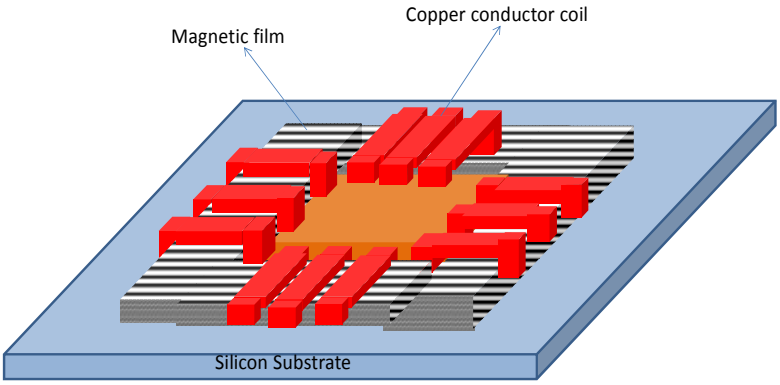


Figure 0.16 Schematic top-view of toroid inductor to be fabricated

The process-flow for the toroid inductor test wafer fabrication is shown in Figure 5.17. The multilayered composite structures are laminated onto silicon substrates with copper structures and patterned to form inductor structures. This involves the following steps:

1. Forming the bottom layer of the coil by copper plating
2. Polymer Dielectric layer for bottom isolation
3. Lamination and patterning of the multilayered composite core.
4. Via formation through dielectric in top and bottom isolation layers.
5. Via plating and forming top layer of the coil by copper plating.

The fabrication begins with an 4-inch Si wafer with Ti/Cu sputtered on it as seed layer for electroplating. Bottom coils were formed on it through a semi-additive process (SAP) by electroplating copper of thickness 20 microns. The plated wafer was laminatedwith an organic dielectric layer (ZIF) having a thickness of 22.5 μm, to form the isolation between the magnetic film and bottom winding.

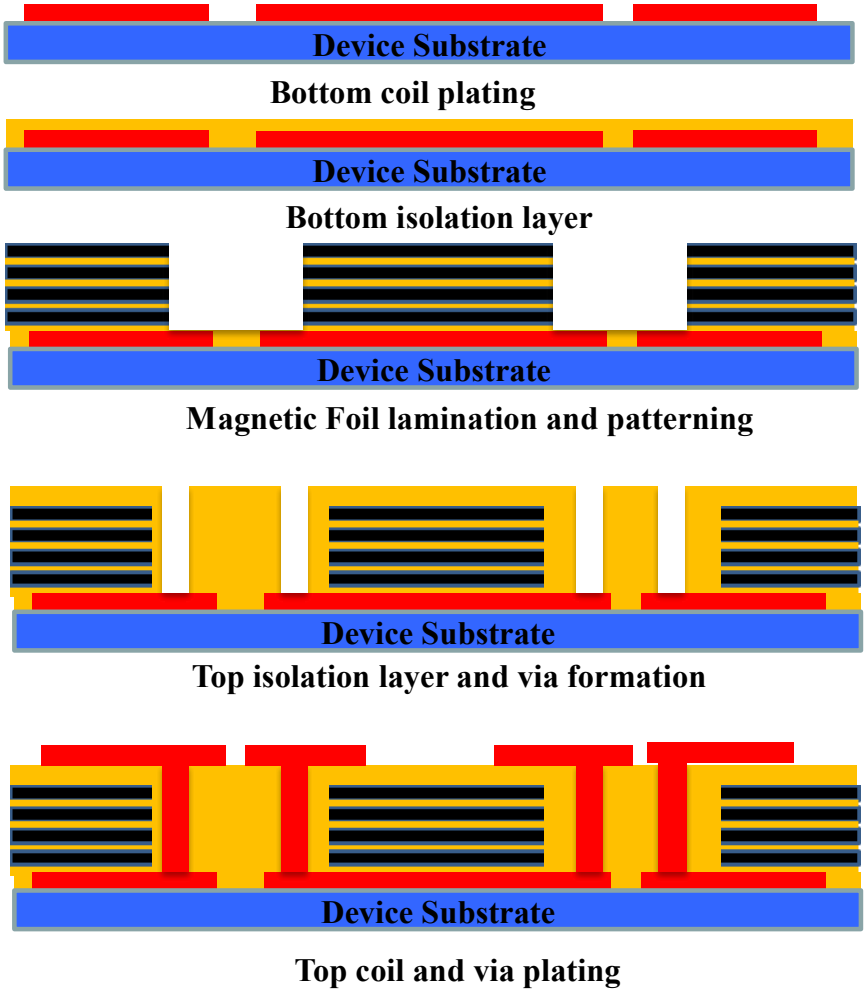


Figure 0.17 Process flow for fabricating toroid inductors

The dry-film ZIF dielectric was bonded onto the wafer by using a vacuum laminator at 95$^{o}$C for 120s. Next, a 10 μm thick multilayered (4-layers) NiFeMo foil laminate was bonded onto the dielectric by using a hot press at 250 C for 1 hour. The magnetic film was patterned into toroid structures using the sequential etching process explained earlier. After the patterning of the magnetic material, another ZIF layer (22.5 μm thick) was coated on these patterned magnetic bars. Then, $CO_2$ laser-drilling was used to open the holes through the dielectric layer for vias. The vias were desmeared using permanganate solution to clean any residue. After that, Cu was electroplated to fill the vias and grow the top copper layer (20 μm thick) to form a complete loop of the copper coil and complete

the test wafer. Figure 5.18 shows different steps of the process to fabricate an inductor test wafer. Figure 5.19 shows a completely fabricated inductor test wafer. Figure 5.20 shows the image of an individual inductor test coupon with test pads after fabrication.

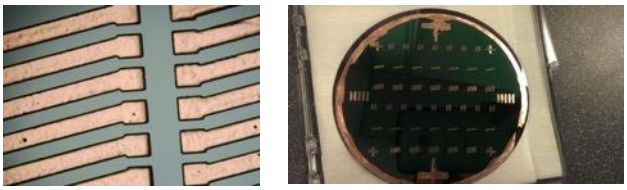

Bottom coil plated

Magnetic layer laminated and patterned

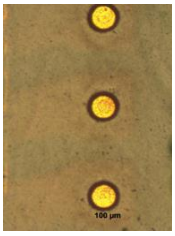

Via drilled through ZIF dielectric by $CO_2$ laser

Top coil and via plated

Figure 0.18 Inductor test wafer fabrication steps

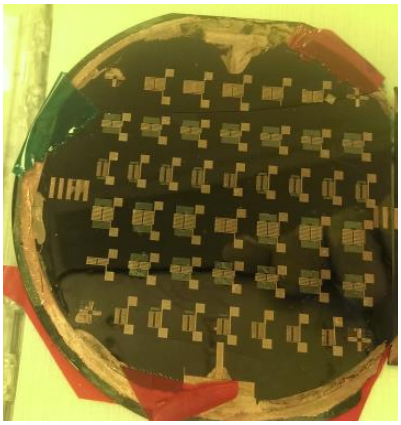

Figure 0.19 Complete inductor test wafer after fabrication

Figure 0.20 Single inductor test coupon

## 5.5 Electrical characterization of fabricated inductors

The inductor test wafers show good devices yield of ~50%. The DC resistance of the devices was measured using a multimeter and showed low values of 0.4-0.5 ohms, indicating good connectivity through the vias. The calculated DC resistance of each inductor based on its geometry is 0.408 ohms, considering the thickness of plated Cu to be 20 μms and its resistivity, $\rho=2x10^{-8}$ ohm-m. Although, it was difficult to measure the individual via contact resistances, the comparison between the measured and the estimated values suggest that the resistance of a metal via contact had almost negligible values. Thus, the electroplating coils have stable via connections with good metal contacts.

The inductance of the fabricated devices from 0.5-5 MHz was measured with a Precision LCR meter having the measurement capability over a frequency range of 75KHz - 30MHz. Figure 5.21 shows an image of the LCR meter used for inductance measurements. The LCR meter was setup with a probe station and calibrated using standard SMD inductors over a range of 5nH-5μH.

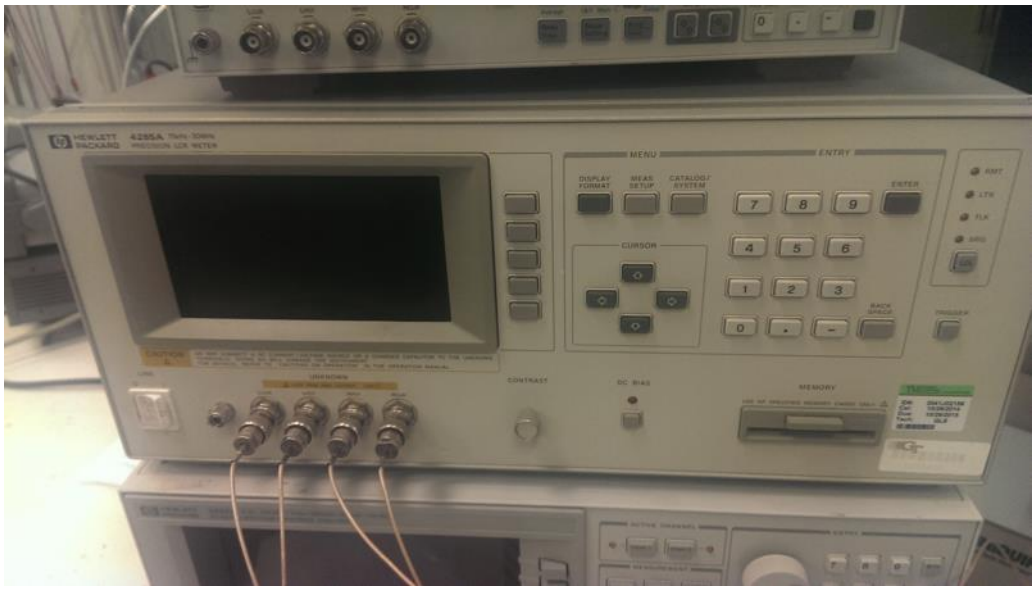


Figure 0.21 Precision LCR meter

For accurate benchmarking of the magnetic core inductors, air core inductors of the same toroid design were fabricated and measured. The parasitics of the cables and testing pads are removed by careful calibration of the tool through an OPEN-SHORT correction method. Figure 5.22 shows the plot of inductance vs frequency for air core and magnetic inductors measured over a frequency range of 1-30 MHz.

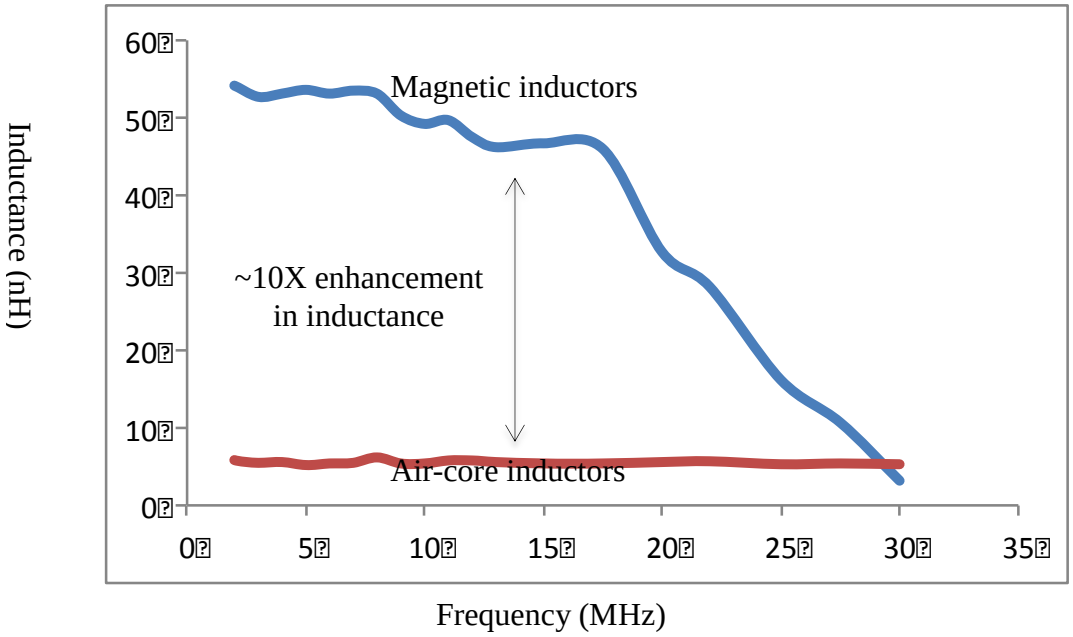


Figure 0.22 Variation of inductance with frequency for air air-core and magnetic inductors

From the plot, ~10X enhancement of inductance is seen with magnetic laminate (~thickness-10 μms) inductors over air core inductors. Further enhancement of inductance density is possible with better inductor design and scaling magnetic film thickness. The frequency roll-off of inductance for the magnetic laminate inductors is shown to be beyond 10MHz. This is almost entirely due to the dependence of the permeability of the multilayered composite core on frequency.

## 5.6 Analysis and Discussion

The classical expression given by Soohoo (Equation 1.3) has been widely used to estimate the inductance of magnetic inductors. However, this expression is known to significantly overestimate the actual inductance. One of the reasons for the discrepancy is the demagnetization effect in patterned magnetic cores[101]. The formation of the demagnetization field inside the finite-sized magnetic core effectively reduces the relative permeability $\mu_r$ of the magnetic cores. In addition, the inductance contribution from winding can be comparable to that from the magnetic cores, and hence the winding and magnetic contributions should be carefully separated. Taking these into account, the inductance of the integrated toroid inductor with magnetic core can be described by the following expression [102]:

$$L_{MC} = L_{AC} + \Delta L \qquad (5.1)$$

$$\text{where } \Delta L = \frac{t_m w_m N^2 \mu_r \mu_0}{l_m(1+N_d(\mu_r-1))} = \frac{t_m w_m N^2 \mu_{eff} \mu_0}{l_m} \qquad (5.2)$$

$$\mu_{eff} = \frac{\mu_r}{1+N_d(\mu_r-1)} \qquad (5.3)$$

where $\Delta L$ is the net increase in the inductance due to the magnetic contribution, $L_{AC}$ is the inductance of an air core inductor of same design and $N_d$ is the demagnetization factor. N is the number of coil turns, and $w_m$, $t_m$ and $l_m$ are the width, thickness, and the length of the magnetic core, respectively. The demagnetization field is not uniform inside the magnetic core and it is not trivial to analytically estimate it [103]. However, numerical solutions available in the literature show that the the demagnetization effect is more severe with higher permeability[103]. The inductance enhancement due to the magnetic contribution is expressed as [79]:

$$\frac{L_{MC}-L_{AC}}{L_{AC}} = \frac{\Delta L}{L_{AC}} \approx \mu_{eff} \frac{A_{MC}}{A_{AC}} \qquad (5.4)$$

where $A_{MC}$ is the cross-section area of the magnetic core and $A_{AC}$ is the cross-section area of the air core. The above expression shows that the actual inductance gain is greatly reduced from $\mu_r$, since $\mu_{eff} < \mu_r$ and $A_{MC} < A_{AC}$.

Performance benefits of multilayered composite inductors: Despite the demagnetization effects, the inductance gain from magnetic cores can, however, still be significant. In this study, the inductance was enhanced by a factor of 10 even with thinner magnetic composite films (~10 μms). With thicker magnetic films (50-100 μms), the enhancement can be even more significant.

Air-core inductors with reasonable quality factors can be designed to have inductance densities of upto 200 nH/mm$^2$ [15]. Such inductor designs have high copper winding density. Integration of the multilayered composite magnetic core with such air-core inductor structures can achieve inductance densities beyond 2000 nH/mm$^2$. This is due to the 10X inductance enhancement shown in this study by multilayered composite inductors over air-core inductors.

Along with the inductance enhancement, the power handling capability is also dramatically enhanced because of the high Ms achieved from the magnetic films. Discrete inductors used in power modules today are made of ferrite cores which have a $M_s$ of ~0.3T. The multilayered composite structures showed an $M_s$ of 0.62T . Thus, using Equation 1.4, it can be shown that the power handling is enhanced by 4X due to the increase in $M_s$.

Significant reduction in inductor thickness is also seen due to silicon integration with ultra-thin, high permeability (~500) multilayered composite cores. Discrete power inductors have thicknesses greater than 500 μms whereas the Si-integrated inductors

demonstrated in this research are less than 100 μm thickness. Thus, a 5X reduction in thickness is seen.

## 5.7 Summary

Si-integrated inductors were successfully demonstrated with multilayered composite structures as magnetic cores. Various processes for micro-patterning the composite structure were explored. Sequential etching was selected as the front-up process for patterning toroid structures. The fabrication process for integrated inductors, consisting of forming coils around toroid-patterned multilayered composite structures is described in detail. The fabricated test wafers show good yield of devices with low DC resistance. The high-frequency inductance of the fabricated magnetic inductors is measured using a Precision LCR meter and is compared against air-core inductors having the same toroid design. The frequency roll-off of inductance for the multilayered composite inductors is shown to occur beyond 10MHz. Approximately 10X enhancement of inductance over air core inductors is shown with magnetic laminate (~thickness-10 μms) inductors. The discrepancy between designed and measured inductance is explained through the reduction in the effective permeability from demagnetization fields.

The performance benefits of the multilayered composite inductors are demonstrated and compared to prior art. The capability of achieving significant enhancement in inductance density(~2X) and power handling capability (~4X) as well as drastic reduction in inductor thickness (5X) over prior art is demonstrated.

# CHAPTER 6

# SUMMARY AND OUTLOOK

## 6.1 Research Summary

Emerging multifunctional smart and wearable electronic systems utilize increasing number of power modules to convert the battery voltage to the device voltage and current requirements. These power modules occupy a major fraction of system volume. Magnetic components such as inductors are the largest components in these power modules, creating a major bottleneck for system miniaturization. The critical parameters governing the size and performance of power inductors are its inductance density and power handling capability. These parameters are determined by the permeability (μ) and saturation magnetization (Ms) of the inductor core materials. Traditional magnetic material approaches do not achieve high Ms and μ at the desired frequency of operation (1-10 MHz). Fabrication of ultra-miniaturized and ultra-thin inductors with advanced high-performance magnetic materials, on the other hand, is also limited by the geometry and processing requirements.

This study investigates an innovative approach to address the above challenges using multilayered ferromagnetic-polymer dielectric composite structures. The composite structure aims at achieving high μ, high Ms, and low loss—all three simultaneously at high frequencies (1-10 MHz) in ultra-thin form factor (50-100 microns). Ultra-thin Si substrate-integrated inductors that can potentially achieve higher inductance densities and power-handling than state-of-the-art technologies are also demonstrated with these multilayered composite structures.

The study starts with the modeling and design of the multilayered composite structures. Electromagnetic (EM) based modeling techniques are used to extract the effective frequency-dependent permeability of the composite structures. The design rules for geometry and material parameters of the multilayered composite structures were optimized based on the modeling results. The multilayered composite structure is designed to consist of high $\mu$ magnetic layers (NiFe, NiFeMo, CoZrO) of thickness 2 microns and ultra-thin polymer layers of thickness 0.5 microns.

The next part of the study involves fabricating and characterizing the multilayered composite structures. Based on the design inputs from modeling, multilayered composite structures were fabricated using two approaches: film transfer and foil layering. The structures fabricated using foil lamination showed high $M_s$ (>0.5T) and high $\mu$ (~500) upto 10 MHz. The measured permeability of the multilayered composite structures matches well with the modeling results, thus validating the modeling approach.The composite structures fabricated with film transfer had even higher $\mu$ (~1000) stable beyond 100 MHz.

The final part of the study demonstrates design, fabrication and characterization of ultra-thin inductors with the multilayered magnetic composite cores, integrated onto silicon substrates. The process of micro-patterning the composite structures and forming 3D coils around them to demonstrate ultra-thin inductors, is described in detail. The electrical characterization of the fabricated inductors with multilayered composite structure showed low DC resistance (0.3-0.5 ohms) and 10X inductance enhancement over air-core inductors of the same design. Further enhancement of inductance density requires implementing finer lithography for patterning and copper plating with fine line structures for extra winding density. With implementation of better inductor designs, these ultra-thin inductors (thickness < 100 microns) are shown to be capable of achieving high

inductance densities upto 2000 nH/mm$^2$ and power handling of 1A/mm$^2$ for 100 μm core component thickness

## 6.2 Future Work

The following directions are suggested for future research in this area:

**Fabrication of multilayered composite structures**:

- Explore options for laminating ultra-thin dry-film polymer dielectrics as the adhesive layer instead of spin-coating BCB solutions: The fabrication of thicker multilayered composite structures with foil-layering can be made more compatible with large-scale roll-to-roll manufacturing by using dry-film dielectrics as the polymer adhesive layers.
- Enhance the frequency-stability of permeability for the multilayered composite structures beyond 10 MHz : Decreasing the thickness of each magnetic layer or increasing its resistivity, can enhance the frequency-stability of permeability as dictated by the eddy current models. The thickness of the magnetic layers can be decreased by controlled wet-etching of NiFeMo foils before lamination. Doping the NiFeMo alloys with Si before casting and cold rolling can increase the resisitivity of the foils and thus enhance the frequency stability of permeability.
- Enhance the current-carrying capability of multilayered composite structures by magnetic annealing: Magnetic annealing of the composite structures post fabrication will increase the DC field at which the inductor core saturates at higher current levels. This enhances their power-handling ability.

**Design and fabrication of ultra-thin multilayered composite inductors:**

- Explore various inductor designs with increased winding densities: Inductor designs consisting of more copper windings around the multilayered composite

structure can help in enhancing the inductance density. Before the fabrication, device simulation with various design parameters needs to be carried out to predict and optimize the inductor performance. This can be performed using commercial or customized simulation software packages. The permeability of the composite structures and the demagnetization effects of patterning them should be taken into account in the simulations.

- Explore various options for large-scale patterning of thicker multilayered composite structures: Large scale patterning of thicker composite structures can enable fabrication of inductors with enhanced inductance density and power handling. The method of sequential etching used in this study for micro-patterning of composite structures during fabrication of inductors is only viable for thinner composite structures. Various options for micro-patterning these structures such as blade cutting, dicing, micro-machining etc., and their feasibility for large scale manufacturing need to be further studied.

# REFERENCES


[1] R. R. Tummala, "SOP: what is it and why? A new microsystem-integration technology paradigm-Moore's law for system integration of miniaturized convergent systems of the next decade," *Advanced Packaging, IEEE Transactions on,* vol. 27, pp. 241-249, 2004.

[2] R. R. Tummala, "Moore's law meets its match (system-on-package)," *Spectrum, IEEE,* vol. 43, pp. 44-49, 2006.

[3] M. Swaminathan, J. Kim, I. Novak, and J. P. Libous, "Power distribution networks for system-on-package: Status and challenges," *Advanced Packaging, IEEE Transactions on,* vol. 27, pp. 286-300, 2004.

[4] L. D. Smith, R. E. Anderson, D. W. Forehand, T. J. Pelc, and T. Roy, "Power distribution system design methodology and capacitor selection for modern CMOS technology," *Advanced Packaging, IEEE Transactions on,* vol. 22, pp. 284-291, 1999.

[5] W. J. Lambert, M. J. Hill, K. Radhakrishnan, L. Wojewoda, and A. E. Augustine, "Package embedded inductors for integrated voltage regulators," in *Electronic Components and Technology Conference (ECTC), 2014 IEEE 64th*, 2014, pp. 528-534.

[6] W.Kim
Available:http://www.eecs.harvard.edu/~wonyoung/IVR_intro_Jun2012.pdf.

[7] C. Ó. Mathúna, N. Wang, S. Kulkarni, and S. Roy, "Review of integrated magnetics for power supply on chip (PwrSoC)," *Power Electronics, IEEE Transactions on,* vol. 27, pp. 4799-4816, 2012.

[8] . *T. Instruments. (2014, November 10). MicroSiPTM Power Modules*. Available: http://www.ti.com/ww/en/analog/power_management/microsip/index.html?DCMP=fullyc&HQS=tlead-power-dcdc-pwr-alps-lpdc-fullyc-20140926-lp3-en

[9] J. Park and M. Allen, "Development of magnetic materials and processing techniques applicable to integrated micromagnetic devices," *Journal of Micromechanics and Microengineering,* vol. 8, p. 307, 1998.

[10] I. Kowase, T. Sato, K. Yamasawa, and Y. Miura, "A planar inductor using Mn-Zn ferrite/polyimide composite thick film for low-Voltage and large-current DC-DC converter," *Magnetics, IEEE Transactions on,* vol. 41, pp. 3991-3993, 2005.

[11] Y. Fukuda, T. Inoue, T. Mizoguchi, S. Yatabe, and Y. Tachi, "Planar inductor with ferrite layers for DC-DC converter," *Magnetics, IEEE Transactions on*, vol. 39, pp. 2057-2061, 2003.

[12] T. Sato, H. Tomita, A. Sawabe, T. Inoue, T. Mizoguchi, and M. Sahashi, "A magnetic thin film inductor and its application to a MHz switching dc-dc converter," *Magnetics, IEEE Transactions on*, vol. 30, pp. 217-223, 1994.

[13] T. Inoue, K. Nishijima, S. Yatabe, T. Mizoguchi, and T. Sato, "The effect of magnetic film structure on the inductance of a planar inductor," *Magnetics, IEEE Transactions on*, vol. 34, pp. 1372-1374, 1998.

[14] T. Sato, E. Komai, K. Yamasawa, T. Hatanai, and A. Makino, "Application of nanocrystalline Fe (or Co-Fe)-Hf-O magnetic films with high electrical resistivity to micro DC-DC converters," *Magnetics, IEEE Transactions on*, vol. 33, pp. 3310-3312, 1997.

[15] Y. Sasaki, S. Morita, T. Hatanai, A. Makino, T. Sato, and K. Yamasawa, "High frequency soft magnetic properties of nanocrystalline Fe-(Co)-Hf-O films with high electrical resistivity and their application to micro DC-DC converter," *NanoStructured Materials*, vol. 8, pp. 1025-1032, 1997.

[16] T. Sato, K. Yamasawa, H. Tomita, T. Inoue, and T. Mizoguchi, "Planar power inductor using FeCoBN magnetic film with high saturation magnetization and high electrical resistivity," in *Proc. IPEC*, 2000, pp. 303-308.

[17] K. H. Kim, J. Kim, H. J. Kim, S. H. Han, and H. J. Kim, "A megahertz switching DC/DC converter using FeBN thin film inductor," *Magnetics, IEEE Transactions on*, vol. 38, pp. 3162-3164, 2002.

[18] H. Nakazawa, M. Edo, Y. Katayama, M. Gekinozu, S. Sugahara, Z. Hayashi, *et al.*, "Micro-DC/DC converter that integrates planar inductor on power IC," *IEEE transactions on magnetics*, vol. 36, pp. 3518-3520, 2000.

[19] Y. Katayama, S. Sugahara, H. Nakazawa, and M. Edo, "High-power-density MHz-switching monolithic DC-DC converter with thin-film inductor," in *Power Electronics Specialists Conference, 2000. PESC 00. 2000 IEEE 31st Annual*, 2000, pp. 1485-1490.

[20] J. Y. Park, S. H. Han, and M. G. Allen, "Batch-fabricated microinductors with electroplated magnetically anisotropic and laminated alloy cores," *Magnetics, IEEE Transactions on*, vol. 35, pp. 4291-4300, 1999.

[21] M. Brunet, T. O. Donnell, L. Baud, N. Wang, J. O. Brien, P. McCloskey, *et al.*, "Electrical performance of microtransformers for DC-DC converter applications," *Magnetics, IEEE Transactions on*, vol. 38, pp. 3174-3176, 2002.

[22] J. Y. Park and M. G. Allen, "Integrated electroplated micromachined magnetic devices using low temperature fabrication processes," *Electronics Packaging Manufacturing, IEEE Transactions on,* vol. 23, pp. 48-55, 2000.

[23] J.-W. Park and M. G. Allen, "Ultralow-profile micromachined power inductors with highly laminated Ni/Fe cores: application to low-megahertz DC-DC converters," *Magnetics, IEEE Transactions on,* vol. 39, pp. 3184-3186, 2003.

[24] T. Osaka, "Electrodeposition of highly functional thin films for magnetic recording devices of the next century," *Electrochimica Acta,* vol. 45, pp. 3311-3321, 2000.

[25] R. W. Filas, T. M. Liakopoulos, and A. Lotfi, "Micromagnetic device having alloy of cobalt, phosphorus and iron," ed: Google Patents, 2003.

[26] C.J.Kaiser, *The Inductor Handbook*: CJ Publisher, April 1996.

[27] . *A critical comparison of ferrites and other magnetic materials*. Available: http://www.mag-inc.com

[28] R. Ramprasad, P. Zurcher, M. Petras, M. Miller, and P. Renaud, "Magnetic properties of metallic ferromagnetic nanoparticle composites," *Journal of applied physics,* vol. 96, pp. 519-529, 2004.

[29] R. G. Arnaudov and R. B. Borisov, "Simple extraction of effective dielectric permittivity and magnetic permeability in IC transmission lines on multilayer substrates," in *Telecommunications Forum (TELFOR), 2012 20th*, 2012, pp. 947-950.

[30] E. P. Valstyn and H. B. Huang, "An extended, dynamictransmission-line'model for thin-film heads," *Magnetics, IEEE Transactions on,* vol. 29, pp. 3870-3872, 1993.

[31] Y. Li and G. Li, "Physics of ferrites," *Science, Beijing*, p. 335, 1978.

[32] S. Liao, "Ferromagnetic Physics," *Science, Beijing*, pp. 17-81, 1992.

[33] B. Lu, X. Dong, H. Huang, X. Zhang, X. Zhu, J. Lei, *et al.*, "Microwave absorption properties of the core/shell-type iron and nickel nanoparticles," *Journal of magnetism and magnetic materials,* vol. 320, pp. 1106-1111, 2008.

[34] F. Mazaleyrat and L. Varga, "Ferromagnetic nanocomposites," *Journal of magnetism and magnetic materials,* vol. 215, pp. 253-259, 2000.

[35] M. Wu, Y. Zhang, S. Hui, T. Xiao, S. Ge, W. Hines, *et al.*, "Microwave magnetic properties of Co50/(SiO2) 50 nanoparticles," *Applied Physics Letters*, vol. 80, pp. 4404-4406, 2002.

[36] M. A. Abshinova, A. V. Lopatin, N. E. Kazantseva, J. Vilčáková, and P. Sáha, "Correlation between the microstructure and the electromagnetic properties of carbonyl iron filled polymer composites," *Composites part A: Applied science and manufacturing*, vol. 38, pp. 2471-2485, 2007.

[37] M. Obol and C. Vittoria, "Microwave permeability of Y-type hexaferrites in zero field," *Journal of applied physics*, vol. 94, pp. 4013-4017, 2003.

[38] C. Kittel and P. McEuen, *Introduction to solid state physics* vol. 7: Wiley New York, 1996.

[39] J. Snoek, "Dispersion and absorption in magnetic ferrites at frequencies above one Mc/s," *Physica*, vol. 14, pp. 207-217, 1948.

[40] C.W.Chen, *Magnetism and Metallurgy of Soft Magnetic Materials* vol. XV. New York: North Holland Publishing Company, 1977.

[41] J. S. a. H. P. J. Wijn, *Ferrites*. Holland: Philips, 1959.

[42] D. Jiles, *Introduction to magnetism and magnetic materials*. London: Chapman and Hall, 1998.

[43] B.D.Cullity, *Introduction To Magnetic Materials*. Massachussets: Addison-Wesley Publishing Company, 1972.

[44] H. Shokrollahi and K. Janghorban, "Influence of additives on the magnetic properties, microstructure and densification of Mn–Zn soft ferrites," *Materials Science and Engineering: B*, vol. 141, pp. 91-107, 2007.

[45] D. Vladikova, L. Ilkov, and S. Karbanov, "Influence of the microstructure on some microwave properties of substituted nickel ferrites," *physica status solidi (a)*, vol. 111, pp. 145-154, 1989.

[46] C. Guillaud, "The properties of manganese-zinc ferrites and the physical processes governing them," *Proceedings of the IEE-Part B: Radio and Electronic Engineering*, vol. 104, pp. 165-173, 1957.

[47] A. H. Qureshi, "The influence of hafnia and impurities (CaO/SiO 2) on the microstructure and magnetic properties of Mn–Zn ferrites," *Journal of crystal growth*, vol. 286, pp. 365-370, 2006.

[48] S.-F. Wang, Y.-J. Chiang, Y.-F. Hsu, and C.-H. Chen, "Effects of additives on the loss characteristics of Mn–Zn ferrite," *Journal of Magnetism and Magnetic Materials,* vol. 365, pp. 119-125, 2014.

[49] Y. Yoshizawa, S. Oguma, and K. Yamauchi, "New Fe-based soft magnetic alloys composed of ultrafine grain structure," *Journal of applied physics,* vol. 64, pp. 6044-6046, 1988.

[50] G. Herzer, "Grain size dependence of coercivity and permeability in nanocrystalline ferromagnets," *Magnetics, IEEE Transactions on,* vol. 26, pp. 1397-1402, 1990.

[51] R. Alben, J. Becker, and M. Chi, "Random anisotropy in amorphous ferromagnets," *Journal of applied physics,* vol. 49, pp. 1653-1658, 1978.

[52] G. Herzer, "Soft magnetic nanocrystalline materials," *Scripta Metallurgica et Materialia,* vol. 33, pp. 1741-1756, 1995.

[53] Y. Zhao, C. Ni, D. Kruczynski, X. Zhang, and J. Q. Xiao, "Exchange-coupled soft magnetic FeNi-SiO2 nanocomposite," *The Journal of Physical Chemistry B,* vol. 108, pp. 3691-3693, 2004.

[54] V. Leger, C. Ramiarinjaona, R. Barrue, and R. Lebourgeois, "Composite magnetic materials based on nanocrystalline powders for middle-and high-frequency applications up to 1MHz," *Journal of magnetism and magnetic materials,* vol. 191, pp. 169-173, 1999.

[55] M. Müller, A. Novy, M. Brunner, and R. Hilzinger, "Powder composite cores of nanocrystalline soft magnetic FeSiB-CuNb alloys," *Journal of magnetism and magnetic materials,* vol. 196, pp. 357-358, 1999.

[56] D. Nuetzel, G. Rieger, J. Wecker, J. Petzold, and M. Mueller, "Nanocrystalline soft magnetic composite-cores with ideal orientation of the powder-flakes," *Journal of magnetism and magnetic materials,* vol. 196, pp. 327-329, 1999.

[57] D. S. Gardner, G. Schrom, F. Paillet, B. Jamieson, T. Karnik, and S. Borkar, "Review of on-chip inductor structures with magnetic films," *Magnetics, IEEE Transactions on,* vol. 45, pp. 4760-4766, 2009.

[58] Y. Xiaolin and R. Chengli, "High frequency properties of Ni< sub> 75</sub> Fe< sub> 25</sub>–SiO< sub> 2</sub> granular thin films with very high resistivity," *Materials Letters,* vol. 61, pp. 908-911, 2007.

[59] Y. Hayakawa, A. Makino, H. Fujimori, and A. Inoue, "High resistive nanocrystalline Fe-MO (M= Hf, Zr, rare-earth metals) soft magnetic films for high-frequency applications," *Journal of applied physics,* vol. 81, p. 3747, 1997.

[60] S. Ohnuma, H. Fujimori, T. Masumoto, X. Xiong, D. Ping, and K. Hono, "FeCo–Zr–O nanogranular soft-magnetic thin films with a high magnetic flux density," *Applied physics letters,* vol. 82, pp. 946-948, 2003.

[61] L. Liangliang, A. M. Crawford, S. X. Wang, A. F. Marshall, M. Ming, T. Schneider, *et al.*, "Soft magnetic granular material Co-Fe-Hf-O for micromagnetic device applications," *Journal of applied physics,* vol. 97, 2005.

[62] N. Tang, W. Zhong, X. Wu, H. Jiang, W. Liu, and Y. Du, "Synthesis and complex permeability of Co/SiO< sub> 2</sub> nanocomposites," *Materials Letters,* vol. 59, pp. 1723-1726, 2005.

[63] L. J. Martin, S. Ooi, D. Staiculescu, M. D. Hill, C. Wong, and M. M. Tentzeris, "Effect of Permittivity and Permeability of a Flexible Magnetic Composite Material on the Performance and Miniaturization Capability of Planar Antennas for RFID and Wearable Wireless Applications," *Components and Packaging Technologies, IEEE Transactions on,* vol. 32, pp. 849-858, 2009.

[64] K. Peng, L. Zhou, A. Hu, Y. Tang, and D. Li, "Synthesis and magnetic properties of Ni–SiO< sub> 2</sub> nanocomposites," *Materials Chemistry and Physics,* vol. 111, pp. 34-37, 2008.

[65] W. Liu, W. Zhong, H. Jiang, N. Tang, X. Wu, and Y. Du, "Highly stable alumina-coated iron nanocomposites synthesized by wet chemistry method," *Surface and Coatings Technology,* vol. 200, pp. 5170-5174, 2006.

[66] Y. Zhan, S. Wang, D. Xiao, J. Budnick, and W. Hines, "Nanocomposite Co/SiO< sub> 2</sub> soft magnetic materials," *Magnetics, IEEE Transactions on,* vol. 37, pp. 2275-2277, 2001.

[67] D. Guo, Z. Zhang, M. Lin, X. Fan, G. Chai, Y. Xu, *et al.*, "Ni–Zn ferrite films with high resonance frequency in the gigahertz range deposited by magnetron sputtering at room temperature," *Journal of Physics D: Applied Physics,* vol. 42, p. 125006, 2009.

[68] G. Xiao and C. Chien, "Temperature dependence of spontaneous magnetization of ultrafine Fe particles in Fe-SiO2 granular solids," *Journal of applied physics,* vol. 61, pp. 3308-3310, 1987.

[69] R. Takahashi, S. Sato, T. Sodesawa, M. Suzuki, and N. Ichikuni, "Ni/SiO2 prepared by sol-gel process using citric acid," *Microporous and mesoporous materials,* vol. 66, pp. 197-208, 2003.

[70] A. Santos, J. Ardisson, A. Viegas, J. Schmidt, A. Persiano, and W. Macedo, "Structure and magnetism of granular Fe–Al< sub> 2</sub> O< sub> 3</sub>," *Journal of magnetism and magnetic materials,* vol. 226, pp. 1861-1863, 2001.

[71] G. Ennas, G. Marongiu, S. Marras, and G. Piccaluga, "Mechanochemical route for the synthesis of cobalt ferrite–silica and iron–cobalt alloy–silica nanocomposites," *Journal of Nanoparticle Research,* vol. 6, pp. 99-105, 2004.

[72] A. K. Giri, C. De Julian, and J. Gonzalez, "Coercivity of Fe-SiO2 nanocomposite materials prepared by ball milling," *Journal of applied physics,* vol. 76, pp. 6573-6575, 1994.

[73] D. Kim, M. Ohnishi, N. Matsushita, and M. Abe, "Magnetic cores usable in gigahertz range: permalloy/Ni-Zn ferrite microcomposite made by low-temperature wet process," *Magnetics, IEEE Transactions on,* vol. 39, pp. 3181-3183, 2003.

[74] M. Saidani and M. A. Gijs, "Cubic millimeter power inductor fabricated in batch-type wafer technology," *Microelectromechanical Systems, Journal of,* vol. 12, pp. 172-178, 2003.

[75] E. Waffenschmidt, B. Ackermann, and J. A. Ferreira, "Design method and material technologies for passives in printed circuit board embedded circuits," *Power Electronics, IEEE Transactions on,* vol. 20, pp. 576-584, 2005.

[76] T. Fujiwara, "Planar integrated magnetic component with transformer and inductor using multilayer printed wiring board," *Magnetics, IEEE Transactions on,* vol. 34, pp. 2051-2053, 1998.

[77] S. Kelly, C. Collins, M. Duffy, F. M. Rhen, and S. Roy, "Core materials for high frequency VRM inductors," in *Power Electronics Specialists Conference, 2007. PESC 2007. IEEE*, 2007, pp. 1767-1772.

[78] M. Ludwig, M. Duffy, T. O'Donnell, P. McCloskey, and S. C. Ó. Mathùna, "PCB integrated inductors for low power DC/DC converter," *Power Electronics, IEEE Transactions on,* vol. 18, pp. 937-945, 2003.

[79] E. Waffenschmidt, "Performance limits of ultra-thin printed circuit board inductors," in *Power Electronics Specialists Conference, 2006. PESC'06. 37th IEEE,* 2006, pp. 1-7.

[80] T. Mikura, K. Nakahara, K. Ikeda, K. Furukuwa, and K. Onitsuka, "New substrate for micro DC-DC converter," in *Electronic Components and Technology Conference, 2006. Proceedings. 56th,* 2006, p. 5 pp.

[81] K. Moon, S. Hong, H. Kim, and J. Kim, "A fabrication of DC-DC converter using LTCC NiZnCu ferrite thick films," in *Magnetics Conference, 2005. INTERMAG Asia 2005. Digests of the IEEE International*, 2005, pp. 1109-1110.

[82] M. H. Lim, J. D. Van Wyk, F. C. Lee, and K. D. Ngo, "A class of ceramic-based chip inductors for hybrid integration in power supplies," *Power Electronics, IEEE Transactions on,* vol. 23, pp. 1556-1564, 2008.

[83] J. Y. Park, L. K. Lagorce, and M. G. Allen, "Ferrite-based integrated planar inductors and transformers fabricated at low temperature," *IEEE Transactions on Magnetics,* vol. 33, pp. 3322-3324, 1997.

[84] J. Y. Park and M. G. Allen, "Low temperature fabrication and characterization of integrated packaging-compatible, ferrite-core magnetic devices," in *Applied Power Electronics Conference and Exposition, 1997. APEC'97 Conference Proceedings 1997., Twelfth Annual*, 1997, pp. 361-367.

[85] Z. Hayashi, Y. Katayama, M. Edo, and H. Nishio, "High-efficiency DC-DC converter chip size module with integrated soft ferrite," *Magnetics, IEEE Transactions on,* vol. 39, pp. 3068-3072, 2003.

[86] D. S. Gardner, G. Schrom, P. Hazucha, F. Paillet, T. Karnik, S. Borkar, *et al.*, "Integrated on-chip inductors using magnetic material (invited)," *Journal of applied physics,* vol. 103, p. 07E927, 2008.

[87] S. Prabhakaran, Y. Sun, P. Dhagat, W.-d. Li, and C. R. Sullivan, "Microfabricated V-groove power inductors for high-current low-voltage fast-transient dc-dc converters," in *Power Electronics Specialists Conference, 2005. PESC'05. IEEE 36th*, 2005, pp. 1513-1519.

[88] P. Hazucha, G. Schrom, J. Hahn, B. Bloechel, P. Hack, G. E. Dermer, *et al.*, "A 233-MHz 80%-87% efficient four-phase DC-DC converter utilizing air-core inductors on package," *Solid-State Circuits, IEEE Journal of,* vol. 40, pp. 838-845, 2005.

[89] T. Osaka, M. Takai, K. Hayashi, K. Ohashi, M. Saito, and K. Yamada, "A soft magnetic CoNiFe film with high saturation magnetic flux density and low coercivity," *Nature,* vol. 392, pp. 796-798, 1998.

[90] J.-W. Park, J. Y. Park, Y.-H. Joung, and M. G. Allen, "Fabrication of high current and low profile micromachined inductor with laminated Ni/Fe core," *Components and Packaging Technologies, IEEE Transactions on,* vol. 25, pp. 106-111, 2002.

[91] S. D. Leith and D. T. Schwartz, "In-situ fabrication of sacrificial layers in electrodeposited NiFe microstructures," *Journal of Micromechanics and Microengineering,* vol. 9, p. 97, 1999.

[92] D. P. Arnold, I. Zana, and M. G. Allen, "Analysis and optimization of vertically oriented, through-wafer, laminated magnetic cores in silicon," *Journal of Micromechanics and Microengineering,* vol. 15, p. 971, 2005.

[93] W. Jayasekara, J. Bain, and M. Kryder, "High frequency initial permeability of NiFe and FeAlN," *Magnetics, IEEE Transactions on*, vol. 34, pp. 1438-1440, 1998.

[94] C. Nelson, *High-frequency and microwave circuit design*: CRC Press, 2007.

[95] R. F. Soohoo, "Microwave magnetics," *New York, Harper and Row Publishers, 1985, 270 p.*, vol. 1, 1985.

[96] V. Bekker, K. Seemann, and H. Leiste, "A new strip line broad-band measurement evaluation for determining the complex permeability of thin ferromagnetic films," *Journal of Magnetism and Magnetic Materials*, vol. 270, pp. 327-332, 2004.

[97] Y. Zhan, S. Wang, D. Xiao, J. Budnick, and W. Hines, "Nanocomposite Co/SiO2 soft magnetic materials," *Magnetics, IEEE Transactions on*, vol. 37, pp. 2275-2277, 2001.

[98] C. A. Grimes and J. V. Prodan, "Swept frequency permeameters for measuring the complex, off-diagonal permeability tensor components of anisotropic, thin magnetic films," *Journal of applied physics*, vol. 73, pp. 6989-6991, 1993.

[99] W. B. Weir, "Automatic measurement of complex dielectric constant and permeability at microwave frequencies," *Proceedings of the IEEE*, vol. 62, pp. 33-36, 1974.

[100] A.-L. Adenot, O. Acher, D. Pain, F. Duverger, M.-J. Malliavin, D. Damiani, *et al.*, "Broadband permeability measurement of ferromagnetic thin films or microwires by a coaxial line perturbation method," *Journal of Applied Physics*, vol. 87, pp. 5965-5967, 2000.

[101] D. Won Lee, K.-P. Hwang, and S. X. Wang, "Design and fabrication of integrated solenoid inductors with magnetic cores," in *Electronic Components and Technology Conference, 2008. ECTC 2008. 58th*, 2008, pp. 701-705.

[102] D. W. Lee, K.-P. Hwang, and S. X. Wang, "Fabrication and analysis of high-performance integrated solenoid inductor with magnetic core," *Magnetics, IEEE Transactions on*, vol. 44, pp. 4089-4095, 2008.

[103] D.-X. Chen, E. Pardo, and A. Sanchez, "Demagnetizing factors for rectangular prisms," *Magnetics, IEEE Transactions on*, vol. 41, pp. 2077-2088, 2005.